

UNIVERSITY OF SÃO PAULO
SÃO CARLOS SCHOOL OF ENGINEERING

ÍTALO LEITE DE CAMARGO

ADDITIVE MANUFACTURING OF ADVANCED CERAMICS BY
DIGITAL LIGHT PROCESSING: EQUIPMENT, SLURRY,
AND 3D PRINTING

São Carlos

2022

ÍTALO LEITE DE CAMARGO

Additive manufacturing of advanced ceramics by digital light processing:
equipment, slurry, and 3D printing

Thesis presented to the São Carlos School of Engineering of the University of São Paulo, as a requirement to obtain the Doctorate degree in Mechanical Engineering (Concentration Area: Mechanical Design, Materials and Manufacturing).

Advisor: Prof. Dr. Carlos Alberto Fortulan

CORRECTED VERSION

São Carlos
2022

I AUTHORIZE THE TOTAL OR PARTIAL REPRODUCTION OF THIS WORK,
THROUGH ANY CONVENTIONAL OR ELECTRONIC MEANS, FOR STUDY AND
RESEARCH PURPOSES, SINCE THE SOURCE IS CITED.

Catalog card prepared by Patron Service at "Prof. Dr. Sergio
Rodrigues Fontes" Library at EESC/USP

C172a Camargo, Italo Leite de
Additive manufacturing of advanced ceramics by digital
light processing : equipment, slurry, and 3D printing /
Italo Leite de Camargo; Thesis directed by Carlos Alberto
Fortulan. -- São Carlos, 2022.

Doctoral (Thesis) - Graduate Program in Mechanical
Engineering and Research Area in Mechanical Design,
Materials and Manufacturing -- São Carlos School of
Engineering of the University of São Paulo, 2022.

1. 3D printing. 2. Additive manufacturing.
3. Ceramics. 4. Digital light processing.
5. Vat photopolymerization. I. Title.

EVALUATION SHEET

Candidate: Engineer **ÍTALO LEITE DE CAMARGO**.

Thesis Title: "Additive manufacturing of advanced ceramics by digital light processing: equipment, slurry, and 3D printing".

Defense Date: November 25, 2022.

Thesis Examination Committee	Judgement
-------------------------------------	------------------

Associate Prof. Carlos Alberto Fortulan (Advisor) (São Carlos School of Engineering – EESC/USP)	Approved
---	-----------------

Full Professor Jonas de Carvalho (São Carlos School of Engineering – EESC/USP)	Approved
--	-----------------

Associate Prof. Cesar Renato Foschini (São Paulo State University – UNESP-Bauru)	Approved
--	-----------------

Prof. Dr. Eduardo Guy Perpétuo Bock (Federal Institute of Education, Science and Technology of São Paulo – IFSP)	Approved
--	-----------------

Full Prof. Cecília Amélia de Carvalho Zavaglia (State University of Campinas – UNICAMP)	Approved
---	-----------------

Coordinator of the Graduate Program in Mechanical Engineering:

Associate Prof. **Adriano Almeida Gonçalves Siqueira**

President of the Graduate Commission:

Full Professor **Murilo Araujo Romero**

ACKNOWLEDGMENTS

To my parents (Fátima and Ivo) and my sister (Gabriela), for their love and encouragement throughout my life. My achievements would not be possible without them.

To Thalita, for the love and support. Also, for her patience during all the working weekends and for the countless times she listened to my presentations.

To my advisor Carlos Alberto Fortulan, for the trust placed and the autonomy he gave me during the years of research.

To Rogério Erbereli, João Fiore Parreira Lovo, Jorge Luís Faneco Paschoa, Mateus Mota Morais, and Ana Caroline Batista Pires, for working directly with me in this research.

To Professor Hayden Taylor and his team at the University of California – Berkeley, for having me and for their cooperation ever since.

To Professors Eduardo Bellini Ferreira, Eder Cavalheiro, and Carla Cristina Schmitt Cavalheiro, for the exchange of ideas and for having made available the infrastructure of their laboratories.

To Professors Cesar Renato Foschini and Jonas de Carvalho, for their valuable comments during the qualifying exam, which helped make this work happen.

To Professors Marcia Cristina Branciforti, Rafael Salomão, Vera Lúcia Arantes, and Zilda de Castro Silveira, for having me as a listener in their classes. Much of the knowledge obtained was applied directly to this work.

To Professor Eduardo Bock, for proposing a noble application for the technique.

To Ana Paula Garcia Ferreira (IQSQ - USP), Diego Luiz Tita (LMA- IQ - UNESP), Heitor Jose Reali Junior (CHR Cerâmica Técnica LTDA), Johan Sebastián Díaz Tovar (IFSC - USP), José Carlos Risardi (EESC-USP), Manoel Ricardo Roncon (IFSC - USP), Luiz Alberto Penazzi (EESC - USP), Naira Canevarolo Pesquero (IQ - UNESP), Raphael Fortulan (Sheffield Hallam University), and Walter Aparecido Mariano (DEMa - UFSCar), for the support with tests.

To Daniel Aparecido Souza, Katiany Thays Lopes Zangrando, and Marcelo Del Guerra, for the help with the first application tests of my research on commercial equipment.

To Paula Aline Prearo Jelaš, for proofreading this thesis.

To BYK and Folpal Química Ltda, for providing samples of dispersants.

To the Federal Institute of Education, Science and Technology of São Paulo (IFSP) and especially to the Itaquaquecetuba campus, for encouraging research and qualification of its employees.

To EESC-USP, for hosting me for more than 10 years.

To the CAASO Athletics Team and running friends, for the hard training that made my days lighter and kept my physical and mental health.

To all my friends and people who somehow contributed to this work.

This study was financed in part by the Coordenação de Aperfeiçoamento de Pessoal de Nível Superior – Brasil (CAPES) – Grant Finance Code 001.

“If you really want to do something, you'll find a way. If you don't, you'll find an excuse.”

Jim Rohn

ABSTRACT

CAMARGO, I.L. **Additive manufacturing of advanced ceramics by digital light processing: equipment, slurry, and 3D printing.** 2022. Thesis (Doctoral) – São Carlos School of Engineering, University of São Paulo, São Carlos, 2022.

Additive manufacturing (AM) or 3D printing is a set of technologies that fabricate parts by successively adding layers. This technique is already applied in all classes of materials. In ceramic manufacturing, AM allows the fabrication of small series components with greater geometric freedom, lower cost, and reduced delivery time. Among the AM technologies, vat photopolymerization (VP) stands out for its ability to produce ceramic pieces with excellent dimensional accuracy and surface finish. However, there is a shortage of VP commercial equipment dedicated to producing ceramics at an affordable price, given the challenges of dealing with raw material with high particle loading. In this work, which approaches the fabrication of advanced ceramics by digital light processing VP, the feasibility of using a top-down 3D printer prototype and an ordinary commercial bottom-up printer (usually applied in polymer 3D printing) in the processing of ceramic materials was tested. For this, a 3D printer prototype was designed and built, creating an innovative recoating system (patent pending), composed of two blades with distinct and sequential functions. This system aims to overcome the challenge of creating layers for ceramic suspensions, which usually have high viscosity. In addition, photosensitive suspensions were developed seeking to meet process requirements related to high ceramic loading, rheological behavior, photosensitive parameters, and stability. The ceramic powders were selected to evaluate the process using distinct groups of advanced ceramics: nanometric powders (3Y-TZP) and submicrometric powders (electrofused mullite). Furthermore, a combination of natural raw material (zircon) with alumina was used to investigate the in-situ formation of mullite-zirconia composites in 3D printed parts. Thus, photosensitive ceramic suspensions based on a nanometric zirconia powder (3Y-TZP) were developed and characterized, selecting the appropriate components (monomer, photoinitiator, and dispersant). In this way, a ceramic slurry was obtained capable of validating the developed prototype and manufacturing green ceramic bodies. Nonetheless, the same formulation was not suitable for the commercial 3D printer, due to its rheological behavior not being compatible with the equipment. On the other hand, the submicrometric mullite powder allowed the preparation of formulations with high solid loading (up to 50 vol%). These new formulations were successfully used in both pieces of equipment tested. Furthermore, the formulation based

on the mixture of ceramic powders (zircon and alumina) showed that the technique can be combined with reactive sintering to create in-situ mullite and zirconia composites. After analysis of the thermal decomposition, a protocol for the thermal treatment was created and the printed bodies were submitted to burning of the organic components and sintering. Both 3D printers tested proved capable of creating dense ceramic pieces (>95%) and with geometries that would be unfeasible or even impossible by other manufacturing methods. The various characterizations of the sintered bodies (mechanical strength, microstructure, etc.) indicate that there are still limitations when the present route is compared with conventional manufacturing processes. Finally, it is believed that the present study contributes to the knowledge related to the additive manufacturing of ceramics and stands out for presenting an approach accessible to laboratories and small manufacturers of ceramic products.

Keywords: 3D printing; Additive manufacturing; Ceramics; Digital light processing; Vat photopolymerization.

RESUMO

CAMARGO, I.L. **Manufatura aditiva de cerâmicas avançadas por fotopolimerização por projeção: equipamento, barbotina e impressão 3D**. 2022. Tese (Doutorado) – Escola de Engenharia de São Carlos, Universidade de São Paulo, São Carlos, 2022.

A manufatura aditiva (MA) ou impressão 3D é um conjunto de tecnologias que fabrica corpos pela adição sucessiva de camadas. Tal técnica já é aplicada em todas as classes de materiais. Na fabricação cerâmica, a MA permite a produção de corpos em pequena escala, com maior liberdade de forma, menor custo e prazo de entrega reduzido. Dentre as tecnologias de MA, a fotopolimerização em cuba se destaca pela capacidade de produzir peças cerâmicas com excelente precisão dimensional e acabamento superficial. Contudo, existe uma escassez de equipamentos comerciais destinados a produzir cerâmica, baseados nessa tecnologia e com preço acessível, visto os desafios de lidar com a matéria-prima com alto carregamento de partículas. Neste trabalho, que aborda a fabricação de cerâmica avançada por fotopolimerização por projeção, foi testada a viabilidade do uso de um protótipo de impressora 3D *top-down* e de uma impressora comercial *bottom-up* comum (usualmente empregada na impressão 3D de polímeros) no processamento de materiais cerâmicos. Para isso, um protótipo de impressora 3D foi projetado e construído, criando-se um sistema de recobrimento inovador (patente depositada), composto por duas lâminas com funções distintas e sequenciais. Esse sistema visa superar o desafio de criação de camadas para as suspensões cerâmicas, que usualmente apresentam alta viscosidade. Além disso, suspensões fotopolimerizáveis foram desenvolvidas buscando atender os requisitos do processo relacionados ao alto carregamento cerâmico, comportamento reológico, parâmetros fotossensíveis e estabilidade. Os pós cerâmicos foram selecionados para avaliar o processo usando grupos distintos de cerâmica avançada: pó nanométrico (3Y-TZP) e pó submicrométrico (mulita eletrofundida). Além disso, a combinação de matéria-prima natural (zirconita) com alumina foi usada para investigar a formação *in-situ* de compósitos mulita-zircônia em peças impressas. Assim, suspensões fotopolimerizáveis cerâmicas baseadas em um pó nanométrico de zircônia (3Y-TZP) foram desenvolvidas e caracterizadas, selecionando-se os componentes (monômero, fotoiniciador e dispersante) apropriados. Desta forma, obteve-se uma barbotina cerâmica capaz de validar o protótipo desenvolvido e fabricar corpos cerâmicos verdes. Contudo, a mesma formulação não foi adequada na impressora 3D comercial, devido ao seu comportamento reológico não ser compatível com o equipamento. Por sua vez, o pó submicrométrico de mulita permitiu o preparo

de formulações com alto carregamento sólido (até 50 %v/v). Essas novas formulações foram usadas com sucesso nos dois equipamentos testados. Ainda, a formulação baseada na mistura de pós cerâmicos (zirconita e alumina) mostrou que a técnica pode ser combinada com sinterização reativa para criar compósitos *in-situ* de mulita e zircônia. Após análise da decomposição térmica, um protocolo para o tratamento térmico foi criado e os corpos impressos foram submetidos à queima dos componentes orgânicos e sinterização. Ambos os equipamentos testados se mostraram capazes de criar peças cerâmicas densas (>95%) e com geometrias que seriam inviáveis ou até mesmo impossíveis por outros métodos de fabricação. As diversas caracterizações dos corpos sinterizados (resistência mecânica, microestrutura, etc.) indicam que ainda existem limitações quando a presente rota é comparada com os processos convencionais de fabricação. Por fim, acredita-se que o presente estudo contribui para o conhecimento relacionado à manufatura aditiva de cerâmicas e destaca-se por apresentar uma abordagem acessível aos laboratórios e pequenos fabricantes de produtos cerâmicos.

Palavras-chave: Impressão 3D; Manufatura aditiva; Cerâmica; Fotopolimerização por projeção; Fotopolimerização em cuba.

LIST OF FIGURES

Figure 1 – Vat photopolymerization classification according to the light pattern formation. a) Stereolithography (SLA). b) Digital light processing (DLP).	35
Figure 2 – Top-down vat photopolymerization.	35
Figure 3 – Schematic of a not constant layer formed in the top-down approach.	36
Figure 4 – Bottom-up vat photopolymerization.	36
Figure 5 – Potential applications for ceramic vat photopolymerization. a) Tissue engineering, represented by a trabecular bone replica made of tricalcium phosphate [84]. b) Heat exchanger, represented by a pipe with a complex structure made of alumina [75]. c) Catalytic applications, represented by a honeycomb and twisted honeycomb components made of alumina [88]. d) Dental restorations, represented by crowns made of alumina (left) and zirconia (right) [99].	37
Figure 6 – Recoating system used for years in SLA-250 (3D Systems). A blade moves horizontally above the vat, spreading the photopolymerizable material	39
Figure 7 – Recoating system composed of brush elements spaced at regular intervals.	39
Figure 8 – Recoating system with pumping. The raw material is pumped and then deposited and pumped by an elongated nozzle member.	40
Figure 9 – Recoating system in which a thin film covers a movable rigid plate, spreading and forming new layers.	40
Figure 10 – Meniscus formation generated in simple blade recoating.	41
Figure 11 – Recoating system with transition zones. Parts are 3D printed just in the central zone and the transition zones are used so that the scraper reaches the central zone with adequate speed.	41
Figure 12 – Recoating system with “active recoater blade”. A roller translates across the working surface and rotates counter to the direction of translation, and associated with a dam, creates a layer of photopolymerizable material.	42
Figure 13 – Recoating system with “liquid curtain”. A distribution chamber is moved horizontally back and forth by a piston, while the photopolymerizable material is pumped into the distribution chamber, creating a liquid curtain.	43
Figure 14 – Zephyr® recoating system. The photopolymerizable material is maintained by a vacuum pump and deposited by an applicator.	43
Figure 15 – Recoating system based on rollers with an additional degree of freedom provided by a pivot hinge.	44
Figure 16 – Recoating system based on a tape casting configuration.	45
Figure 17 – Organization of particles according to the flow in a highly loaded suspension. a) Particles at rest; b) the ordering of particles in layers promotes shear-thinning; c) destruction of the layered organization of the particles and subsequent jamming promote shear-thickening.	47
Figure 18 – Suspension viscosity curves for different solid loadings.	48

Figure 19 – Representation of the rheological behavior of suspensions that show a transition from shear-thinning to shear-thickening behavior. The critical shear rate $\dot{\gamma}_{cr}$ decreases with increasing solid loading.	49
Figure 20 – Representation of the rheological behavior of a suspension with yield stress according to Herschel-Bulkley’s model.	50
Figure 21 – Krieger-Dougherty’s model with $B = 2.5$ and $\phi_m = 63.7\%$	53
Figure 22 – Effect of the fraction of large particles on the viscosity of a bimodal suspension, for different levels of solid loading (10 to 75 vol%). The particle size ratio is 5:1.	54
Figure 23 – Schematic representation of smaller particles free to flow in the interstices of large particles. Particle size ratio: 40:1.	54
Figure 24 – Comparison of mono and multifunctional monomers: a) monofunctional monomers; b) linear polymerization of monofunctional monomers; c) entanglement of linear polymeric chains; d) bifunctional monomers; e) network polymerization of bifunctional monomers; f) polymeric network with cross-linking (in red).	57
Figure 25 – Schematic illustration of steric stabilization. Dispersant molecules have polar anchor groups adsorbed in the ceramic surfaces and hydrophobic chains soluble in the medium, creating a protective layer against agglomeration.	62
Figure 26 – Viscosity curve as a function of dispersant concentration.	64
Figure 27 – Schematic of the materials and methods used in this thesis.	73
Figure 28 – Schematic diagram of a top-down DLP test bench.	75
Figure 29 – SEM images of the 3Y-TZP powder (TZ-3Y-E). a) Granules. b) Magnified granule. c) Granule surface composed of particles. d) Particles.	77
Figure 30 – Schematic diagram of the sedimentation test	80
Figure 31 – Manual spread of layers performed by previous works of our research group. ...	83
Figure 32 – Schematic diagram of the recoating system concept. a) Spreading with the first blade active. b) Active blade change. c) Leveling and thickness calibration with the second blade active.	85
Figure 33 – Sketch of the designed recoating system.	85
Figure 34 – Built recoating system	86
Figure 35 – 3D printer prototype built.	86
Figure 36 – Ceramic suspension based on preliminary studies of our research group, after 4 hours of preparation, presenting sedimentation and liquid phase separation (yellowish coloring) at the top.	88
Figure 37 – Emission spectrum of the used mercury-vapor lamp and absorbance of the photoinitiator selected (BAPO).	89
Figure 38 – Rheological behavior of 3Y-TZP ceramic slurries with 15 vol% solid loadings (a) with different dispersants with varying concentrations at a shear rate of 30 s^{-1} . (b) Viscosity curve with different dispersants in the concentration which provided the lowest viscosity. (c) Shear stress vs shear rate with different dispersants fitted by the Herschel-Bulkley model. ..	90
Figure 39 – Sedimentation test of 3Y-TZP ceramic slurries with 15 vol% solid loading with different dispersants. (a) Suspensions with different dispersants after 30 days of settling. (b) Retained volume fraction as a function of the time.	91

Figure 40 – Rheological behavior of 3Y-TZP ceramic slurries with 30 vol% solid loading (a) viscosity curve with different monomers (b) Shear stress vs shear rate with different monomers fitted by the Herschel-Bulkley model.....	93
Figure 41 – Influence of solid loading in 3Y-TZP ceramic slurries with 2wt% of Disperbyk-111 at a shear rate of 30 s ⁻¹	94
Figure 42 – Rheological behavior of 40 vol% solid loading 3Y-TZP ceramic slurries with different dispersant concentrations. (a) Viscosity curve; (b) Shear stress vs shear rate fitted by the Herschel-Bulkley model.	95
Figure 43 – Cure depth vs exposure energy of the 3Y-TZP photosensitive ceramic suspension.	96
Figure 44 – Thermogravimetric analysis of the 3Y-TZP green printed parts. b) Post-processing protocol.....	97
Figure 45 – 3Y-TZP green parts manufactured in the built prototype.	98
Figure 46 – 3Y-TZP printed adaptation of Christ the Redeemer Statue (Rio de Janeiro – Brazil). (a) Green part. (b) Sintered part.	98
Figure 47 – Top view of the vat after removal of the 3Y-TZP suspension, indicating a “sticking” printing failure: the first layer does not adhere to the building platform and sticks to the transparent bottom of the vat.	99
Figure 48 – Characterization of 3Y-TZP printed parts sintered at different temperatures. a) Relative density. b) Linear Shrinkage.	100
Figure 49 – SEM images of 3Y-TZP printed part sintered at 1600 °C.	101
Figure 50 – a) Flexural strength of the 3Y-TZP printed parts sintered at different temperatures. b) Specimens that failed at the layers interface in the flexural test.	102
Figure 51 – X-ray diffraction patterns for the 3Y-TZP raw material and parts sintered at different temperatures.....	103
Figure 52 – Mullite mean particle size as a function of the grinding time.....	104
Figure 53 – SEM image of the ground mullite powder.....	105
Figure 54 – X-ray diffraction pattern for the ground mullite powder.	106
Figure 55 – Rheological behavior of mullite slurries with 40 vol% solid loading (a) varying dispersant concentrations at a shear rate of 30 s ⁻¹ . (b) Viscosity curve with 3 wt% of dispersant (concentration which provided the lowest viscosity).	107
Figure 56 – Influence of solid loading in mullite slurries at a shear rate of 30 s ⁻¹	108
Figure 57 – Cure depth vs exposure energy of the mullite photosensitive suspensions with different solid loading.....	108
Figure 58 – Thermogravimetric analysis of a green mullite printed part.....	109
Figure 59 – Mullite green parts manufactured in the DLP 3D printer prototype.....	109
Figure 60 – Mullite sintered 3D printed parts. a) Miscellaneous components. b) Torch. c) Pyramid. d) Scaffold with a complex internal structure.	110
Figure 61 – Green mullite parts manufactured in the commercial 3D printer.	111
Figure 62 – 3D printing fail of a mullite green part: partial detachment from the build platform.	112

Figure 63 – Successful 3D printing of mullite part with inclined orientation. a) 3D printed part with the support. b) 3D printed part after support removal. c) 3D printed part and support.	112
Figure 64 – Mullite sintered part from 3D printing with inclined configuration.....	113
Figure 65 – Mullite 3D printed part with tiny structures. a) Green part (Eiffel Tower). b) Base of the tower after breaking during post-processing. c) Piece of the tower after breaking during post-processing.....	114
Figure 66 – SEM images of sintered mullite 3D printed parts showing the interface between the layers.	115
Figure 67 – Influence of sintering temperature and solid loading on linear shrinkage of mullite 3D printed parts. a) Linear shrinkage in the building direction. b) Linear shrinkage in the XY plane.	116
Figure 68 – SEM images of mullite parts sintered at 1600 °C from suspensions with different solid loading. a) 45 vol%. b) 50 vol%.....	117
Figure 69 – Influence of sintering temperature and solid loading on properties of mullite 3D printed parts. a) Relative density. b) Flexural strength.	118
Figure 70 – SEM images of mullite parts sintered from 50 vol% suspensions at different temperatures. a) 1500 °C. b) 1550 °C. c) 1600 °C. d) 1650 °C.	119
Figure 71 – X-ray diffraction patterns for the mullite raw material and parts sintered at different temperatures.	120
Figure 72 – SEM images of the ceramic powders used in the preparation of the photosensitive suspensions. a) Calcined Alumina. b) Ground Zircon.	121
Figure 73 – Viscosity curves of the prepared ceramic suspensions made of alumina, zircon, and the stoichiometric mixture.....	122
Figure 74 – 3D printed parts made of a stoichiometric mixture of zircon and alumina with tiny structures. a) Green. b) Sintered at 1600 °C.	122
Figure 75 – X-ray diffraction patterns for the alumina and zircon raw materials and parts sintered at different temperatures made of a stoichiometric mixture of zircon and alumina. Peaks of zircon are marked with ♦, alumina with ■, monoclinic Zirconia with ●, and mullite with ★.	123
Figure 76 – Influence of sintering temperature on true density and bulk density of 3D printed parts made of a stoichiometric mixture of zircon and alumina.	124
Figure 77 – SEM-EDS elemental mapping of a sample made of a stoichiometric mixture of zircon and alumina sintered at 1400 °C. a) Scanning Electron Microscopy. b) Element mapping of Zr. c) Element mapping of Al. d) Element mapping of Si.	126
Figure 78 – SEM-EDS elemental mapping of a sample made of a stoichiometric mixture of zircon and alumina sintered at 1500 °C. a) Scanning Electron Microscopy (SEM). b) Magnified view of the SEM image with an indication of an impurity-rich region. c) Element mapping of Zr. d) Element mapping of Al. e) Element mapping of Si.	127
Figure 79 – SEM-EDS elemental mapping of a sample made of a stoichiometric mixture of zircon and alumina sintered at 1600 °C. a) Scanning Electron Microscopy. b) Element mapping of Zr. c) Element mapping of Al. d) Element mapping of Si.	128
Figure 80 – SEM-BSD image of a sample made of a stoichiometric mixture of zircon and alumina sintered at 1600 °C.	129

Figure 81 – 3D caricature of the author of this thesis made of mullite (3D model created by the artist Raul Tabajara, manufactured from the 40 vol% mullite suspension in the selected commercial 3D printer and sintered at 1600 °C)..... 130

LIST OF TABLES

Table 1 – Patented recoating systems	45
Table 2 – Properties of monomers used in ceramic vat photopolymerization.....	56
Table 3 – Properties of diluents used in ceramic vat photopolymerization.....	57
Table 4 – Refractive index for some printable ceramic materials.	59
Table 5 – Some combinations of monomers and diluents for ceramic VP.....	60
Table 6 – Dispersants used in formulations of ceramic slurries vat photopolymerization.	65
Table 7 – Dispersants used in formulations of ceramic slurries for vat photopolymerization. Studies from the same research group are displayed in sequence.	67
Table 8 – Photoinitiator used in ceramic VP	69
Table 9 – Monomers used in this thesis.....	79
Table 10 – Application of TRIZ on requirements contradictions.....	84
Table 11 – Post-processing protocol used in this work.	97
Table 12 – Influence of sintering temperature on open and closed porosity of samples made of stoichiometric mixture of zircon and alumina.	124
Table 13 – Summary of the best results obtained with the photosensitive ceramic suspensions developed in this work.	131

LIST OF ABBREVIATIONS

2HEA	2-Hydroxyethyl acrylate
3Y-TZP	3 mol% yttria stabilized tetragonal zirconia polycrystal
4HBA	4-Hydroxybutyl acrylate
ABCM	Brazilian Society of Mechanical Sciences and Engineering
ACMO	4-Acryloylmorpholine
AM	Additive manufacturing
APTMS	3-(Trimethoxysilyl)propylacrylate
ASTM	American Society for Testing and Materials
BAPO	Phenylbis(2,4,6-trimethyl benzoyl)phosphine oxide
BDDA	1,4-Butanediol diacrylate
BEA	Butoxyethyl acetate
BIOENG	Laboratory of Bioengineering and Biomaterials
BP	Benzophenone (diphenylmethanone)
BPAE2DMA	Bisphenol A bis(2-hydroxyethyl ether) dimethacrylate
COBEF	Brazilian Congress on Manufacturing Engineering
CQ	Camphorquinone
DEGDA	Di(ethylene glycol) diacrylate
Di-TMPTA	Di(trimethylolpropane) tetraacrylate
DLP	Digital light processing
DMPA	2,2-dimethoxy-2-phenylacetophenone
DPHA	Dipentaerythritol penta-/hexa-acrylate
EESC	São Carlos School of Engineering
EPTTA	Ethoxylated pentaerythritol tetraacrylate
HCPK	1-Hydroxycyclohexyl phenyl ketone
HDDA	1,6-Hexanediol diacrylate
HDEODA	1,6-Hexanediol ethoxylate diacrylate
HEMA	2-Hydroxyethyl methacrylate
HMPP	2-hydroxy-2-methyl-1-phenyl-propan-1-one
IBOA	Isobornyl acrylate
IDA	Isodecyl acrylate
IFSP	Federal Institute of Education, Science and Technology of São Paulo

IPA	Isopropyl alcohol
KH-570	3-(Trimethoxysilyl)propyl methacrylate
LTC	Laboratory of Tribology and Composites
MBAM	N-N'-Methylenebisacrylamide
NMP	1-Methyl-2-pyrrolidone
NPGPO2DA	Neopentyl glycol (PO) ₂ diacrylate
PAA-NH ₄	Ammonium polyacrylate
PEG	Polyethylene glycol
PEGDA	Poly(ethylene glycol) diacrylate
PhD	Doctor of Philosophy
PHEA	2-Phenoxyethyl acrylate
POE	Phenoxyethanol
PPG	Polypropylene glycol
PPGDMA	Poly(propylene glycol) dimethacrylate
PVP	Polyvinylpyrrolidone
SEM	Scanning electron microscope
SLA	Stereolithography
TEGMA	Tri(ethylene glycol) dimethacrylate
TGA	Thermogravimetric analysis
TMPETA	Trimethylolpropane ethoxylate triacrylate
TMPTA	Trimethylolpropane triacrylate
TPGDA	Tri(propylene glycol) diacrylate
TPO	Diphenyl(2,4,6-trimethylbenzoyl) phosphine oxide
TPO-L	Ethyl(2,4,6-trimethylbenzoyl) phenylphosphinate
TRIZ	Theory of inventive problem solving
TTEGDA	Tetra(ethylene glycol) diacrylate
UDMA	Diurethane dimethacrylate
USP	University of São Paulo
UV-Vis	Ultraviolet-visible
VP	Vat photopolymerization
XRD	X-ray diffraction

LIST OF SIMBOLS

$\dot{\gamma}$	Shear rate
v	Recoating blade speed
e	Layer of thickness
$\dot{\gamma}_{cr}$	Critical shear rate
τ_y	Yield stress
K	Flow consistency index
n	Flow behavior index
ϕ	Solid fraction
d	Particle size
$V_{settling}$	Settling velocity
ρ_{solid}	Solid density
ρ_{fluid}	Fluid density
η_{fluid}	Fluid viscosity
η_r	Relative viscosity
η_s	Suspension viscosity
η_0	Medium viscosity
ϕ	Volumetric solid loading
ϕ_m	Maximum volumetric solid loading
B	Einstein's coefficient
$n_{ceramic}$	Ceramic refractive index
n_{medium}	Medium refractive index
C_d	Cure depth
S_d	Sensitivity of the suspension
E	Incident light energy density
E_c	Critical energy
D_{50}	Average particle size
\emptyset	Diameter
h	Height
T_{etch}	Etching temperature
T_{sint}	Sintering temperature
R^2	Coefficient of determination

SUMMARY

1. INTRODUCTION	29
1.1 Objectives	31
1.2 Thesis Relevance	31
1.3 Thesis Structure	32
2 LITERATURE REVIEW	33
2.1 Additive Manufacturing	33
2.2 Ceramics by additive manufacturing	33
2.3 Vat Photopolymerization	34
2.3.1 Stereolithography vs Digital Light Processing	34
2.3.2 Top-Down vs bottom-up	35
2.4 Ceramics by vat photopolymerization	36
2.5 3D Printers	38
2.5.1 Recoating Systems	38
2.6 Photosensitive Ceramic Suspensions	46
2.6.1 Rheological Behavior	47
2.6.1.1 Non-Newtonian behavior	47
2.6.1.2 Yield stress	49
2.6.1.3 Stability	50
2.6.2 Influence of formulation on the rheological behavior	52
2.6.2.1 Volumetric solid fraction	52
2.6.2.2 Particle size and shape	53
2.6.2.3 Monomers and diluents	55
2.6.2.4 Dispersants	60
2.6.2.4.1 Dispersion and adsorption mechanisms	61
2.6.2.4.2 Optimum amount of dispersant	63
2.6.2.4.3 Types of dispersants used in photosensitive ceramic suspensions	64
2.6.2.5 Best reported formulations concerning rheological behavior	66
2.6.3 Curing Behavior and photosensitive parameters	68
2.6.3.1 Photoinitiators	69
2.7 Post-Processing	70
3 MATERIALS AND METHODS	73
3.1 DLP 3D Printer prototype	74
3.2 Light source irradiance	75
3.3 Ceramic Powders	75
3.3.1 Ceramic Powders preparation	77

3.4	Slurry development	78
3.5	Rheological Behavior.....	79
3.6	Stability	79
3.7	Curing and photosensitive parameters	80
3.8	Thermal analysis	80
3.9	Additive manufacturing and post-processing	81
3.10	Sintered parts characterization	81
4	RESULTS AND DISCUSSIONS.....	83
4.1	DLP 3D Printer Prototype for ceramic materials: design development.....	83
4.2	Additive Manufacturing of 3Y-TZP: slurry development and 3D printer prototype validation.....	87
4.2.1	Choosing the photoinitiator and light source irradiance characterization.....	88
4.2.2	Choosing the dispersant.....	89
4.2.3	Choosing the resin	92
4.2.4	Influence of solid loading on the viscosity.....	93
4.2.5	Choosing the dispersant concentration.....	94
4.2.6	Photosensitive parameters	95
4.2.7	Thermal analysis.....	96
4.2.8	3D printing	97
4.2.9	Sintered parts characterization	99
4.3	Additive Manufacturing of mullite: from coarse electrofused powder to ceramic parts using the built prototype and a low-cost commercial 3D printer.....	103
4.3.1	Ground powder characterization	104
4.3.2	Choosing the dispersant concentration.....	106
4.3.3	Influence of solid loading on the viscosity.....	107
4.3.4	Photosensitive parameters	108
4.3.5	Thermal analysis.....	109
4.3.6	3D printing	109
4.3.7	Comparison between built prototype and commercial 3D printer	110
4.3.8	Post-processing challenge	114
4.3.9	Influence of solid loading and sintering temperature on final parts.....	115
4.4	Additive manufacturing of in situ mullite-zirconia composites.....	120
4.4.1	Powder characterization	120
4.4.2	Slurry rheological Behavior and Stability	121
4.4.3	3D printing	122
4.4.4	Reaction Sintering	123
4.5	Final considerations	129
4.5.1	Summary of the best results obtained in this work	130

4.5.2	General guideline for future developments in ceramic vat photopolymerization....	131
5	CONCLUSIONS	133
5.1	Suggestions for future works	134
6	SCIENTIFIC PRODUCTION	137
6.1	Articles published in Journals.....	137
6.2	Filed patent	138
6.3	Article published as book chapter	138
6.4	Conferences and fairs with presentation of work or lecture	138
6.5	Articles published in magazines	138
	REFERENCES	139

1. INTRODUCTION

Ceramic materials are known for their remarkable properties such as high-temperature resistance, hardness, and chemical inertia [1]. Advanced ceramics are special ceramics that exhibit superior properties and are often produced in small quantities at higher prices [2], having applications in several areas such as solid-oxide fuel cells [3,4], automotive sensors [2], prostheses [5], dental applications [6,7], etc. There is a growing demand for customized (or small series) ceramic parts with complex geometries. In this context, additive manufacturing (AM) stands out for being able to produce these parts without the high costs of molds [8–10], reducing costs and lead times [11].

Additive manufacturing or 3D printing is a set of processes that fabricate parts by adding materials layer by layer. After the great development of additive manufacturing of polymers and metals, developments of this technique applied to ceramic materials have gained prominence in recent years [12,13].

Although several AM processes can manufacture ceramic parts [10], the vat photopolymerization process (VP) stands out for its ability to produce tiny structures with excellent dimensional precision and good surface quality [14,15]. In this type of AM, a photosensitive liquid in a vat is selectively cured by light-activated polymerization [16]. Besides, Digital Light Processing (DLP) is a type of VP in which an entire layer is formed at once by projecting the section, being faster than processes based on scanning the region to be polymerized [14,17,18]. It is a multi-step [16] (or indirect [19]) process, in which additives and binders are used to create a green body that is subsequently debound (to eliminate the organics) and sintered (to increase density) [10,20,21].

The widespread of ceramic AM depends on technological availability [22]. Thus, equipment [22] and proper feedstock [21] availability have been an issue. For example, there is a shortage of VP commercial equipment dedicated to producing ceramics at an affordable price, given the challenges of dealing with raw material with high particle loading. Most commercial VP devices were not designed to handle high viscosity materials, and so to manufacture ceramic components. The few exceptions are costly industrial equipment [23].

Moreover, most manufacturers of ceramic suspensions suitable for vat photopolymerization are also machine manufacturers and, in general, do not supply the feedstock separately. A photosensitive suspension for the VP must fulfill several process requirements [24,25]. For example, a slurry must have solid loading of not less than 40 vol% to avoid cracks and delamination during the post-processing [24,26,27]; proper rheological

behavior and stability to allow uniform and homogeneous micrometric layers to be formed [15,28–30] and adequate photosensitive parameters to ensure geometrical accuracy [3,24,25]. Thus, specifications of the ceramic particles, monomers, and dispersants should be considered [24]. Also, a suitable photoinitiator, compatible with the chosen monomers and light source must be selected [31,32].

Another important step in the manufacture of ceramic parts by DLP is the post-processing of the green printed parts. For example, the debinding must have adequate heating rates to avoid cracks [25,33], being a very challenging process since, in general, the slurries have at least 50 vol% of organic material. Moreover, sintering temperature has a strong influence on the properties of the final parts [4,34–37].

This work has been developed at the Laboratory of Tribology and Composites (LTC), in the Department of Mechanical Engineering of the São Carlos School of Engineering (EESC-USP). This research group has experience with ceramic additive manufacturing, having recently started the studies in ceramic vat photopolymerization. Preliminary studies to the present work had already been conducted in our lab and were able to produce a few ceramic pieces [38,39], however, they had significant limitations. First, the photosensitive ceramic slurries prepared had limited ceramic loading, high viscosity, poor stability, and short shelf life. In addition, the manufacturing was based on the manual spreading of the layers, implying high dependence on the operator and low repeatability.

Despite the strong worldwide development of ceramic VP, the use of this AM technology is still dependent on high investments. On the other hand, this study aims to overcome this restriction, being an important step toward the use of the technique in labs and small companies. Thereunto, multidisciplinary research was carried out, dealing with a variety of research areas such as machine design, ceramic processing, development and characterization of suspensions, etc.

Thus, this work has the hypothesis that it is possible to produce advanced ceramic parts by DLP additive manufacturing using low-cost bottom-up and top-down equipment as long as photosensitive ceramic suspensions with proper rheological behavior, stability, and photosensitive parameters are developed, 3D printed using compatible parameters (e.g. light exposure energy), debound and sintered at an adequate heating protocol.

1.1 Objectives

The main objective of this work is to investigate the additive manufacturing of advanced ceramics by DLP using a top-down 3D printer prototype and an ordinary bottom-up commercial 3D printer (not specialized in ceramic materials). Therefore, the following specific objectives were established:

- ✓ To design and manufacture a top-down DLP 3D Printer with a suitable recoating system;
- ✓ To develop and characterize photosensitive ceramic suspensions;
- ✓ To 3D print green ceramic parts using the built prototype and a low-cost commercial machine;
- ✓ To obtain ceramic parts by debinding and sintering the 3D printed green bodies;
- ✓ To characterize the manufactured ceramic parts.

1.2 Thesis Relevance

The main relevance of this work is related to the comprehension of all stages of ceramic additive manufacturing by DLP, which made it possible to manufacture complex ceramic parts from a variety of ceramic powders, without using the costly 3D printers specialized in ceramic materials. The mastery of the process as a whole also allowed the 3D printing of important types of ceramic (mullite-zirconia composites) for the first time and the use of a raw material (electrofused mullite) which was still little explored by vat photopolymerization.

Thus, this work placed our research group as a reference on the topic in South America. In addition, some achievements should be highlighted:

First, this work is based on a strong literature review, which resulted in an article that was among the top downloaded articles for months in *Ceramics International Journal* and has already received over 30 citations on Scopus.

Second, it created a low-cost and innovative recoating system capable of handling high viscosity materials, such as the high solid loading photosensitive ceramic suspensions. Such an invention has already had its patent application filed.

Next, this thesis led to several publications in international journals and presentations at conferences. One related conference manuscript received the “Best Article Award” at the 11th Brazilian Congress on Manufacturing Engineering (COBEF 2021), the largest national event in the area of Manufacturing Engineering, promoted by the Brazilian Society of Mechanical Sciences and Engineering (ABCM). Also, it was awarded as one of the best 3 works at the 65th

Brazilian Ceramic Conference (CBC 2022), the most important and traditional national event in the sector, organized by the Brazilian Ceramic Society (ABCERAM).

In addition, this work can be useful for several research groups and companies and is already motivating new developments. For example, studies have already begun on the use of the technique to manufacture ceramic centrifugal blood pumps in partnership with Prof. Eduardo Bock (BIOENG-IFSP). Also, glass photosensitive suspension has been developed by a partner research group led by Prof Eduardo Bellini Ferreira (Department of Materials Engineering, EESC-USP), and bone-mimetic structures made of hydroxyapatite were produced by Rogério Erbereli (PhD candidate of LTC research group) in the 3D printer prototype developed in this work. Moreover, some national industries, both in the ceramic and 3D printing sectors, have already made contact, and conversations about partnerships have started.

Lastly, it promoted communication for society, having disseminated the research to non-academic audiences in local newspapers (written and on TV) and magazines.

1.3 Thesis Structure

The thesis is organized according to the following chapters:

Chapter 2 presents a literature review covering important aspects of ceramic vat photopolymerization related to the 3D printers, photosensitive suspensions development and characterization, post-processing, etc.

In Chapter 3, the materials and methods used in this work are introduced, concerning the design of the 3D printer prototype, the development and characterization of the photosensitive ceramic suspensions, 3D printing on the built prototype and in an ordinary commercial 3D printer (not specialized in ceramic materials), post-processing and sintered parts characterization.

Chapter 4 presents and discusses the results on four main topics. The first is related to the design development and building of the DLP 3D Printer Prototype for ceramic materials. The other topics are associated with the development and characterization of photosensitive ceramic suspensions and their use to produce ceramic parts by photopolymerization of three different groups of ceramic materials: nanometric powder (3Y-TZP), submicrometric powder (electrofused mullite), and a combination of natural raw material (zircon) with alumina to investigate reaction sintering and manufacturing of in situ mullite zirconia composites parts.

Finally, Chapter 5 presents the conclusions and suggestions for future works and Chapter 6 shows the scientific production resulting from this work.

2 LITERATURE REVIEW

This chapter addresses the literature review about additive manufacturing, especially topics related to ceramics and vat photopolymerization (3D printers, feedstock development and characterization, post-processing, etc.). This thesis has already led to the publication of articles, and in this way, part of the literature review has been published in articles resulting from this thesis [24,40–47].

2.1 Additive Manufacturing

Additive manufacturing (AM) or 3D printing is a set of technologies that fabricate parts by adding materials, usually layer by layer, from 3D model data [16,17]. AM is well known for its ability to produce parts with complex geometries (freedom of design) and to significantly shorten product development times and costs [17,48]. On the other hand, AM still presents significant challenges concerning the low availability of material suitable for diverse applications, inferior mechanical properties, and anisotropic behavior [21,22,48].

2.2 Ceramics by additive manufacturing

After the extensive development of additive manufacturing of polymers and metals, the application of this technique to ceramic materials has gained prominence in recent years [12,13], aiming at the fabrication of ceramic parts with complex shapes that would be very challenging or even unfeasible by conventional manufacturing methods [12]. Ceramic AM enables the manufacturing of customized ceramic parts without molds [8–10], reducing costs and lead times [11]. However, there are still several challenges to the ceramic AM such as the improvement of surface quality [49], dimensional accuracy, and mechanical properties [10].

Ceramic parts can be produced by a variety of AM technologies [10] such as binder jetting, direct ink writing, fused deposition, material jetting, vat photopolymerization, etc. [45]. Choosing a technology will depend on the application requirements and the technologies characteristics.

Although research into ceramic 3D printing by all technologies started back in the 90s [50–55], its application is still quite restricted when compared to polymers and metals [11,21,56]. The widespread of ceramic AM depends on technological availability [22]. Thus,

proper feedstock [21] and equipment [22] availability have been an issue. Moreover, many technologies present high-priced raw materials, and their supply is linked to the equipment manufacturer [45].

Additive manufacturing can be classified into two categories [16]. In the single-step (or direct [19]) processes, the parts achieve the final shape and properties in a single operation. On the other hand, in the multi-step (or indirect [19]) processes, two or more operations are needed to reach the final part. Multi-step processes are the most common for ceramic AM. Additives and binders are used to create a green body that is subsequently debound (to eliminate the organics) and sintered (to increase density) [10,20,21]. The debinding is a critical step to successfully obtaining the ceramic parts and the heating rates must be suitable to avoid cracks and/or delamination [10,25,33]. Also, debinding becomes more difficult with increasing wall thickness [10], and some AM technologies that use a high amount of organic material, such as vat photopolymerization and fused deposition, have the maximum wall thickness limited [11].

2.3 Vat Photopolymerization

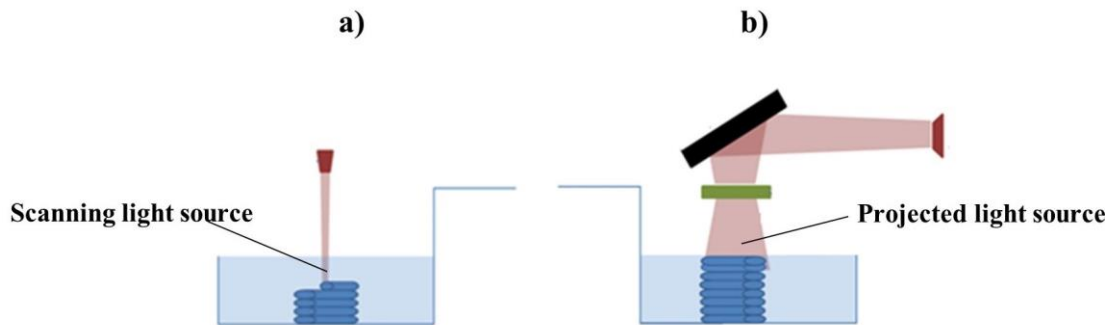
Vat photopolymerization (VP) is an additive manufacturing process in which a liquid photopolymerizable material contained in a vat is selectively cured by light-activated polymerization [16]. It was the first technology of additive manufacturing developed and commercialized [57–60], and it is still widely used by the industry today [61]. It was created in the 80's but only in the late 90's it started to have its application for the manufacture of ceramic components studied [26,55,62,63].

Recent works already point to the manufacture by VP of defect-free ceramic components with high relative density [64–66]. Furthermore, VP stands out among other ceramic AM processes due to its dimensional precision, surface quality, and ability to print tiny structures [14,15,24]

2.3.1 Stereolithography vs Digital Light Processing

The VP process can be divided according to how the light pattern is formed to selectively cure each layer. In the stereolithography (SLA) or vector scan, the pattern is formed by scanning a polymerization point (Figure 1a). On the other hand, in digital light processing (DLP), the entire layer is formed at once, by projecting the entire pattern (Figure 1b), being faster than SLA [14,17].

Figure 1 – Vat photopolymerization classification according to the light pattern formation. a) Stereolithography (SLA). b) Digital light processing (DLP).

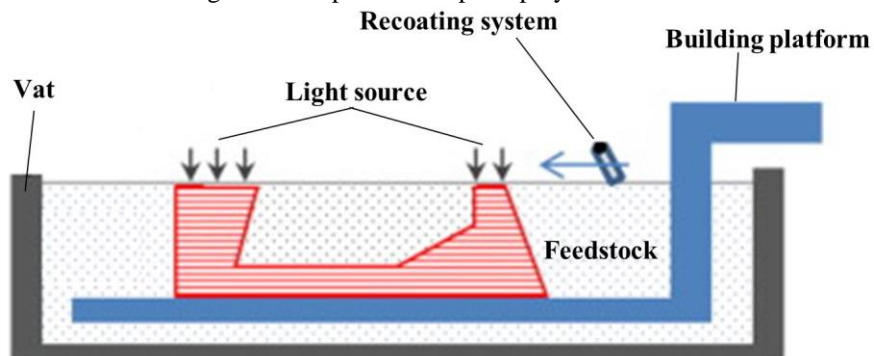


Source: Adapted from [67].

2.3.2 Top-Down vs bottom-up

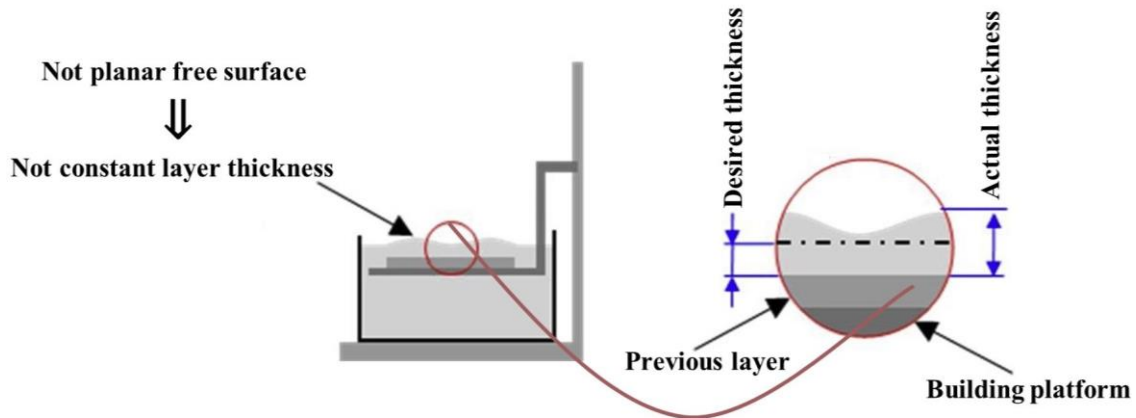
VP processes can also be divided according to the building direction. In the top-down category, the light source is above the vat, and the platform moves downwards, progressively forming new layers (illustrated in Figure 2). In this approach, the main challenge is the recoating, which is the process of depositing a new layer of uncured material between the previously cured layer and the light source. A successful recoating process establishes a fresh layer of thickness exactly equal to the desired one within a short time. The effects related to the viscosity and surface tension properties of the raw material are obstacles to this process. Incorrect or not constant layer thickness (Figure 3) will impair the accuracy of the printed parts [15,18,68]. Therefore, a dedicated recoating system is usually required in a top-down 3D printer [15,18].

Figure 2 – Top-down vat photopolymerization.



Source: Adapted from [69].

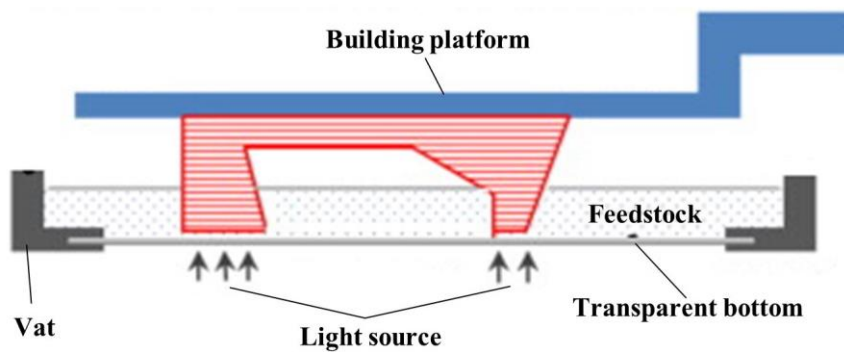
Figure 3 – Schematic of a not constant layer formed in the top-down approach.



Source: Adapted from [15].

On the other hand, in the bottom-up category (Figure 4), the light falls from below through a transparent bottom, and the platform moves upwards after such new layers have been formed [15,70]. In this approach, there is no need for a recoating system [15,18], since the rising movement of the platform will already cause the resin to spontaneously fill the space [40]. However, this process has a major disadvantage. There is a periodic detachment between the last printed layer and the bottom [15,18], which introduces stresses in the part being printed, a problem that is aggravated in high viscosity processes, as in ceramic VP, which uses slurries with high solid concentration [15,71].

Figure 4 – Bottom-up vat photopolymerization.



Source: Adapted from [69].

2.4 Ceramics by vat photopolymerization

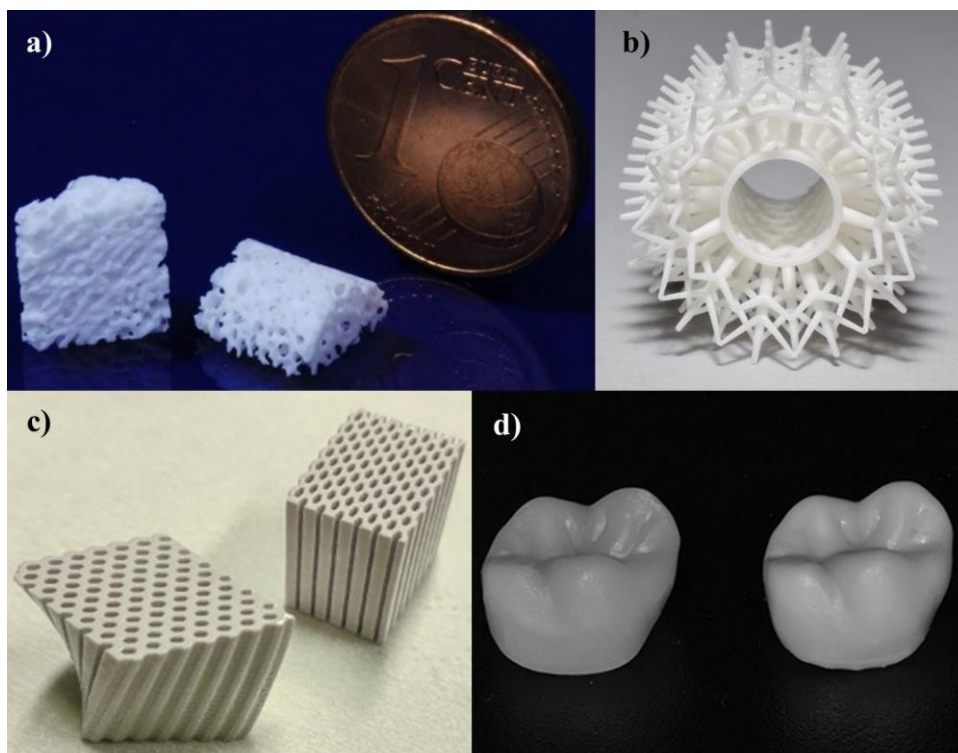
VP stands out among other ceramic AM processes due to its ability to print tiny structures [14,15], in addition to its excellent resolution ($\sim 40 \mu\text{m}$ [72–75]), and surface quality (surface roughness, R_a , below $0.5 \mu\text{m}$ have been reported [9,76–78]). This technology is best

suiting for small ceramic components for high-precision applications [11]. It is not recommended for large dense parts due to the high amount of organic material associated with the process and that would lead to cracks in the debinding of thick sections [11,79], as discussed in detail in section 2.7.

Ceramic Vat Photopolymerization is the most mature additive manufacturing technology [11] and some ready-to-use industrial systems are commercially available as discussed in section 2.5. These systems can produce dense parts (>99%) [9,64–66] and properties comparable to those produced by conventional methods. For example, zirconia produced by vat photopolymerization and with flexural strength greater than 700 MPa has been reported [66,76,78].

Recent research related to ceramic vat photopolymerization indicated potential application in different areas such as ceramic membranes [80–83], tissue engineering [84–87], catalytic applications [88–92], ceramic core for investment casting [93–97], dental restoration [6,7,98,99], solid oxide fuel [3,4,100,101], heat exchanger [75,102–104], among others. Figure 5 illustrates some of these potential applications published in related articles.

Figure 5 – Potential applications for ceramic vat photopolymerization. a) Tissue engineering, represented by a trabecular bone replica made of tricalcium phosphate [84]. b) Heat exchanger, represented by a pipe with a complex structure made of alumina [75]. c) Catalytic applications, represented by a honeycomb and twisted honeycomb components made of alumina [88]. d) Dental restorations, represented by crowns made of alumina (left) and zirconia (right) [99].



Source: Adapted from [75,84,88,99].

There are several key factors for successful ceramic manufacturing by vat photopolymerization concerning 3D printers, photosensitive ceramic suspension, and post-processing. These topics will be covered in the next sections.

2.5 3D Printers

There are dozens of vat photopolymerization machines, popularly known as resin 3D printers, commercially available. However, most of these printers were not designed to handle viscous materials that make it difficult to form constant and homogeneous layers, as is the case with ceramic suspensions with a high content of solid load. Thus, the few capable of producing technological ceramics with good mechanical properties are costly or time-consuming [23].

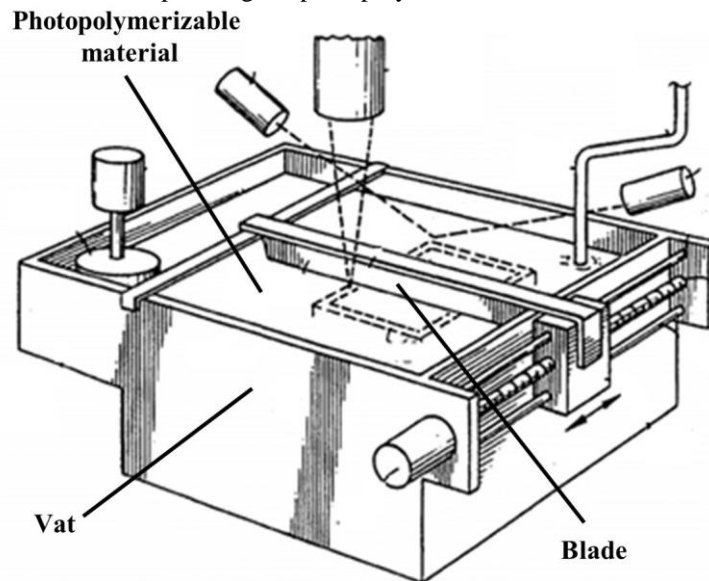
On the other hand, some 3D printer suppliers for ceramic vat photopolymerization such as Fortify and Photocentric emerged in the last 5 years. Moreover, there are well-established companies with years in the market as Admatec, 3DCeram, Lithoz, and Prodways with a variety of related 3D printing systems and feedstock commercially available. These leading suppliers offer industrial ready-to-use solutions [105] and have the ability to process high viscosity materials, which may exceed 15 Pa.s [64,65,106,107] due to their dedicated recoating system. However, these machines are costly, with the sale value usually exceeding US\$100.000,00.

2.5.1 Recoating Systems

As discussed in subsection 2.3.2, top-down VP 3D printers require a recoating system to create uniform layers with constant thickness. Such a system can present a variety of solutions that may include blades, brush elements, drain pumps, pneumatic dispensers, etc. [108]. In this way, in this subsection, a variety of recoating systems will be presented, covering patents related to this topic and solutions adopted by VP 3D printers.

The patent EP0361847B1 [109], filled in 1989, presents the “dip and scrape” recoating system, used for several years in SLA-250 (3D Systems) [110]. This method includes a “deep dip”, in which the part is dipped into the resin vat and then raised until it is a layer thickness from the top of the tank [111]. Then, a simple blade moves from one side to another, removing excess, spreading the photopolymerizable material, and creating a new layer [109–111], as shown in Figure 6. However, the formed layers affect the liquid movement and may lead to recoating faults and parts defects [112], mainly above large solidified layers.

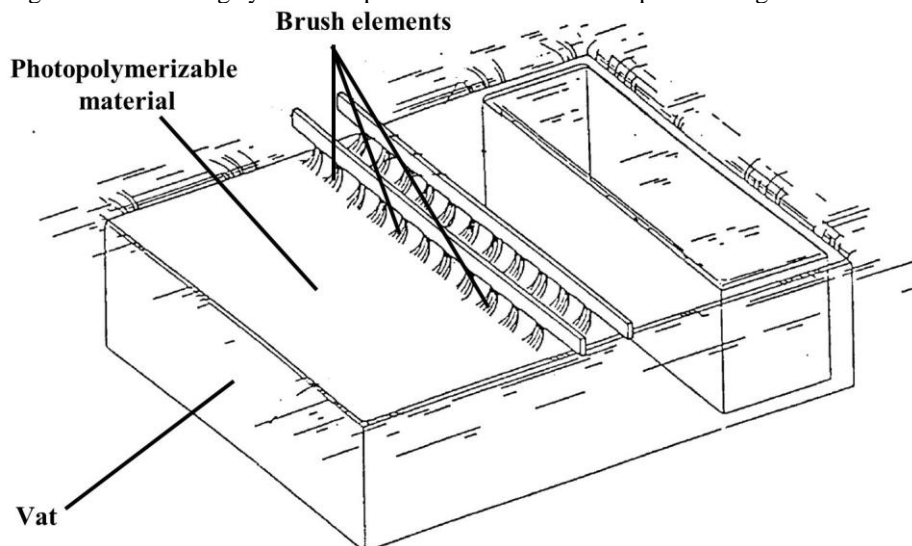
Figure 6 – Recoating system used for years in SLA-250 (3D Systems). A blade moves horizontally above the vat, spreading the photopolymerizable material



Source: Adapted from Patent EP0361847B1 [109].

The patent EP0484182A1 [113], filled in 1991, presents a recoating system composed of brush elements spaced at regular intervals that would provide uniform layers with constant thickness even over a large, solidified area (Figure 7).

Figure 7 – Recoating system composed of brush elements spaced at regular intervals.

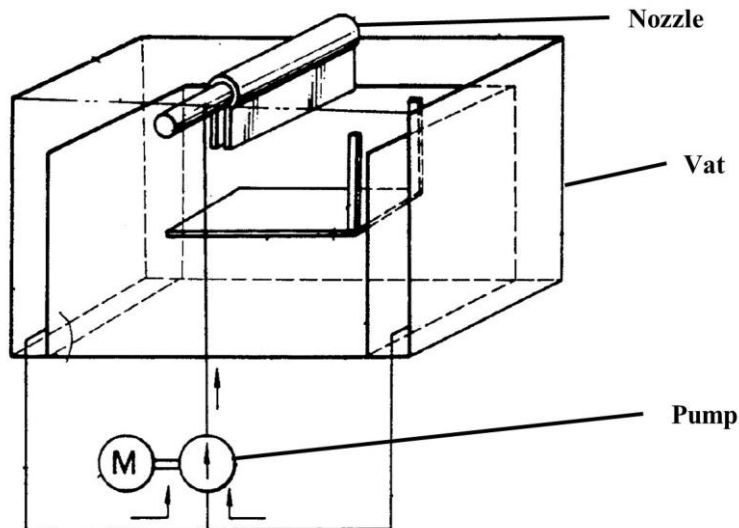


Source: Adapted from Patent EP0484182A1 [113].

The patent US5238497A [114], also filled in 1991, presents a recoating system in which the photopolymerizable material is pumped and then spread. For that, an elongated nozzle is horizontally moved along the working surface while supplying the photosensitive raw material.

Excess resin is directed to a resin storage tank and then again directed to the spreader component, as shown in Figure 8.

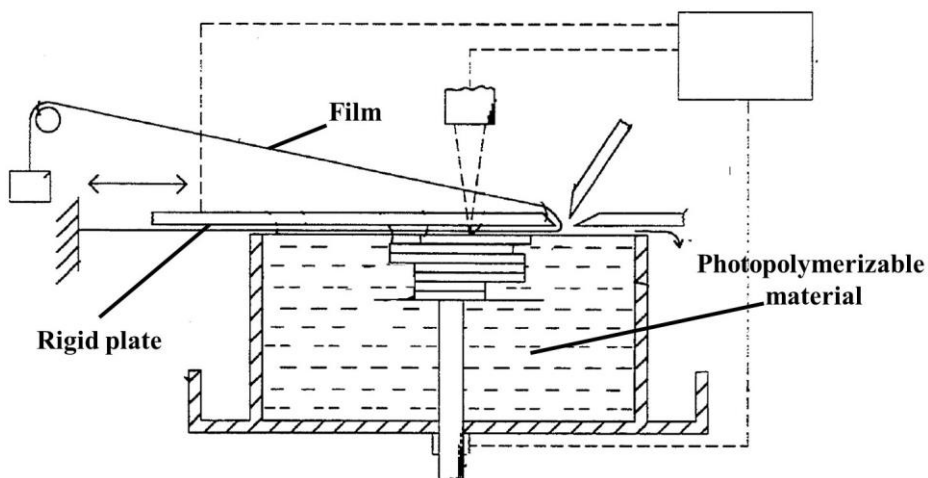
Figure 8 – Recoating system with pumping. The raw material is pumped and then deposited and pumped by an elongated nozzle member.



Source: Adapted from Patent US5238497A [114].

The patent US5447822A [115], filled in 1994, presents a recoating system in which a thin film covers a rigid plate. The film is placed in contact with the photopolymerizable material. The plate with the film moves horizontally across the resin surface, spreading and creating new layers, as shown in Figure 9.

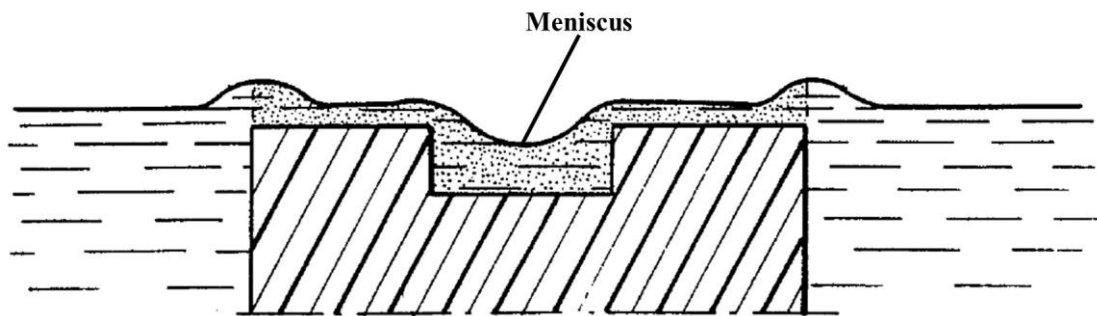
Figure 9 – Recoating system in which a thin film covers a movable rigid plate, spreading and forming new layers.



US5238497A Source: Adapted from Patent US5447822A [115].

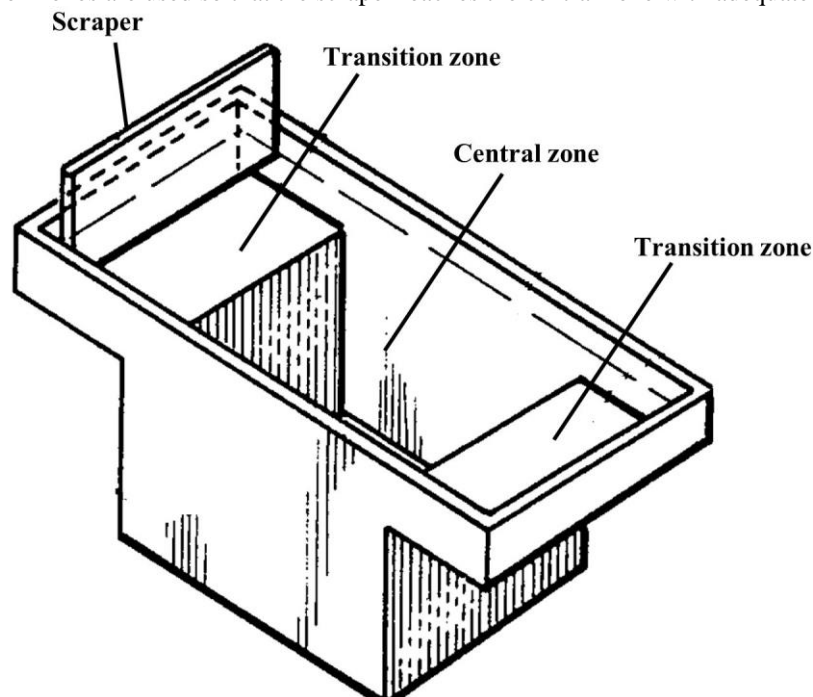
According to patent WO1995015842A1 [116], filled in 1994, the conventional use of a single blade recoating system presents problems with wetting the solid parts, causing menisci close to discontinuities between liquid and solids, hindering good flatness of the layer in formation, as illustrated in Figure 10. This problem can be alleviated by including a transition area for the spreader, as suggested by the same patent, and illustrated in Figure 11. In this case, the part is 3D printed only in the central zone, and the transition zones are used so that the spreader reaches the printing area at its ideal speed. However, the increase in the area covered by the spreader generates an increase in time and consequently in the costs involved in the process.

Figure 10 – Meniscus formation generated in simple blade recoating.



US5238497A Source: Adapted from Patent WO1995015842A1 [116].

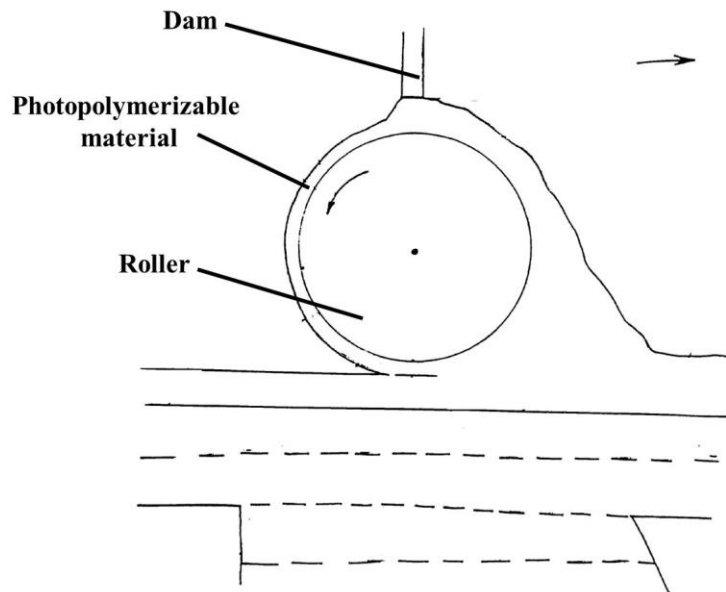
Figure 11 – Recoating system with transition zones. Parts are 3D printed just in the central zone and the transition zones are used so that the scraper reaches the central zone with adequate speed.



US5238497A Source: Adapted from Patent WO1995015842A1 [116].

The patent WO1996023647A2 [117], filled in 1996, presents a recoating system with an “active recoater blade” [112] composed of a counter-rotating roller which translates across the working surface rotates counter to the direction of translation, and associated with a dam, creates layers of the photopolymerizable material, as shown in Figure 12.

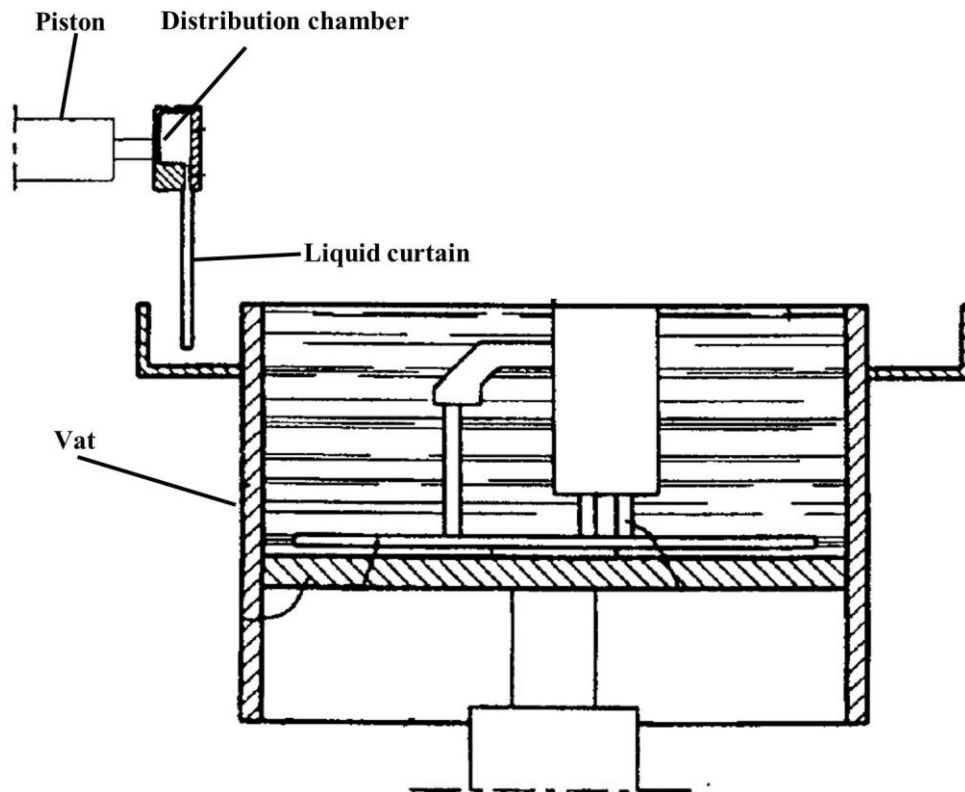
Figure 12 – Recoating system with “active recoater blade”. A roller translates across the working surface and rotates counter to the direction of translation, and associated with a dam, creates a layer of photopolymerizable material.



US5238497A Source: Adapted from Patent WO1996023647A2 [117].

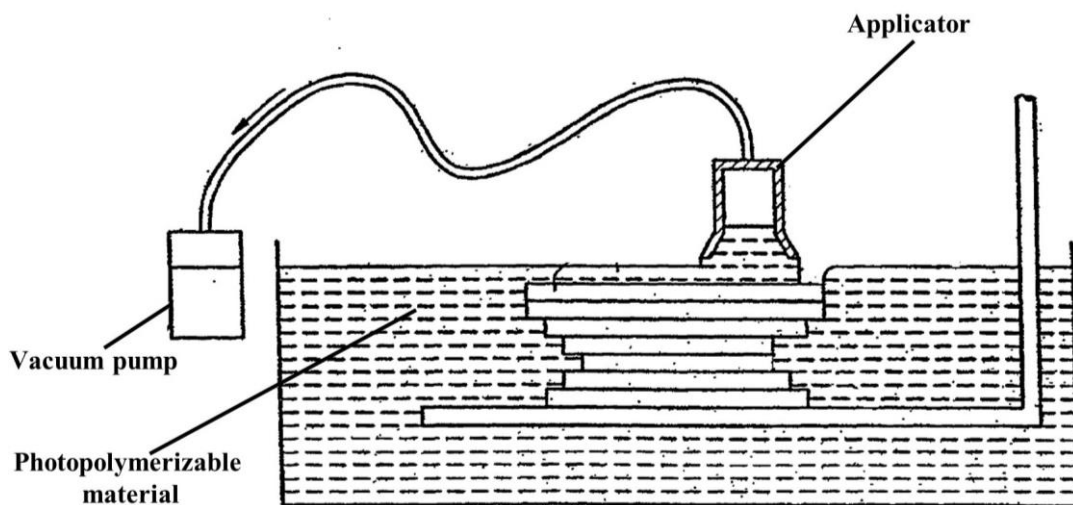
The patent EP0928242B1 [118], filled in 1997, presents a recoating system that pumps the photopolymerizable material from a reservoir to the distribution chamber, creating a liquid sheet, also called liquid curtain (Figure 13). They are moved horizontally back and forth by a piston, and so thin layers are created [119]. This recoating system is currently used in a commercial 3D printer (Mammoth, Materialise) [110].

Figure 13 – Recoating system with “liquid curtain”. A distribution chamber is moved horizontally back and forth by a piston, while the photopolymerizable material is pumped into the distribution chamber, creating a liquid curtain.



Source: Adapted from Patent EP0928242B1 [118]

Figure 14 – Zephyr® recoating system. The photopolymerizable material is maintained by a vacuum pump and deposited by an applicator.

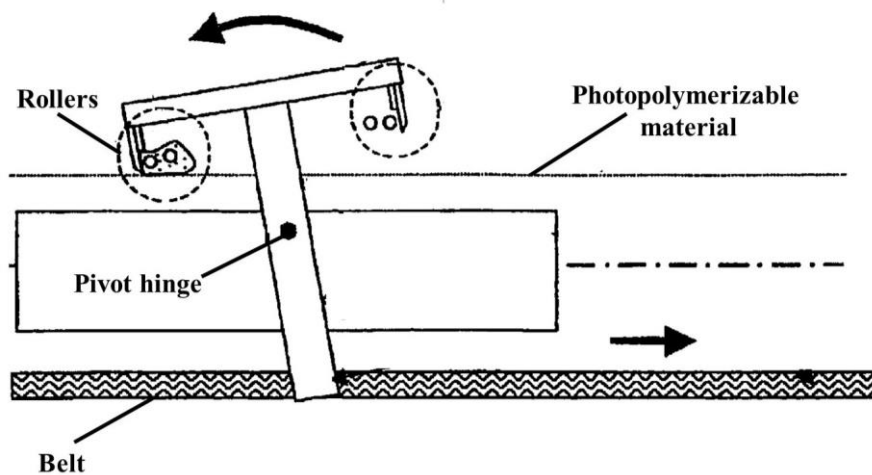


Source: Adapted from Patent EP0807014B1 [120].

The patent EP0807014B1 [120], filled in 1996, presents the Zephyr® recoating system (Figure 14), in which the photopolymerizable material is maintained by a vacuum pump and deposited by an applicator (symmetric hollow blade with a resin reservoir [110]). This system is used in commercial 3D printers such as Promaker 600 (Prodways) and current 3D system printers [40].

The patent US6764636B1[112], filled in 2000, presents a recoating system based on rollers with an additional degree of freedom. A belt promotes the translation of the system and a rotation around the pivot hinge, causing the rollers to come into contact with the photopolymerizable material, promoting its spreading, as shown in Figure 15.

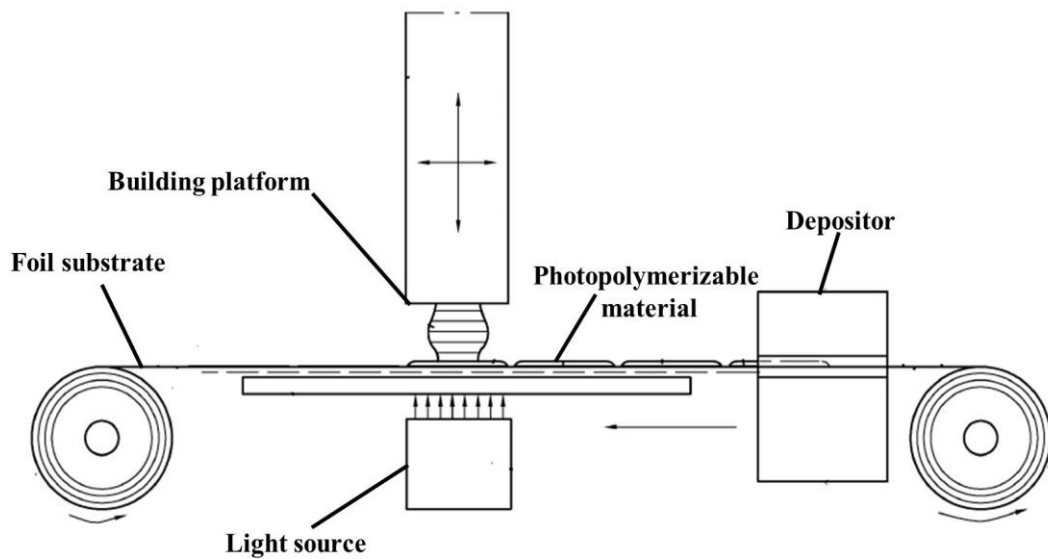
Figure 15 – Recoating system based on rollers with an additional degree of freedom provided by a pivot hinge.



US5238497A Source: Adapted from Patent US6764636B1 [112].

The patent WO2015107066A1 [121], filled in 2015, presents the approach used in the Admaflex 3D printer (Admatec). This system does not use a vat. Instead, it uses a tape casting configuration to create a thin layer of photopolymerizable material. The sections are projected by the light source and the layers are successively forming the part in the building platform (Figure 16). Still, 3DCeram systems use a feeding piston to supply a small amount of the photopolymerizable material (high viscous pastes) that will be spread by a blade recoater [122]. However, a related patent was not found.

Figure 16 – Recoating system based on a tape casting configuration.



US5238497A Source: Adapted from WO2015107066A1 [121].

Furthermore, subsequent patents [123–125] presented improvements to recoating systems with similar operating principles to those already discussed. Thus, Table 1 summarizes the patented recoating systems solutions.

Table 1 – Patented recoating systems

Patent	Filed in	Recoating system solution
EP0361847B1	1989	Simple blade
EP0484182A1	1991	Brush elements
US5238497A	1991	Spreader with pumping of raw material
US5447822A	1994	movable rigid plate covered by thin film
WO1995015842A1	1994	Transition area for the spreader
WO1996023647A2	1996	Active recoater blade
EP0807014B1	1996	Vacuum pump and applicator
EP0928242B1	1997	Liquid curtain
US6764636B1	2000	Rollers with additional degree of freedom
WO2015107066A1	2015	Tape casting

Source: Elaborated by the author.

2.6 Photosensitive Ceramic Suspensions

Parts of this section have been published as a journal paper [24].

One of the main limitations of the widespread of ceramic AM is the shortage of suitable feedstock [11,21,47]. In this context, creating a ceramic photosensitive suspension for vat photopolymerization is challenging. These suspensions are indispensably composed of monomers, photoinitiators, and ceramic powder. The reaction of monomers and photoinitiators in such slurries is typically based on photopolymerization by free radicals activated by light (UV or visible) [14], which initiate and propagate the polymerization reaction, forming a polymeric structure (cross-linking occurs if the monomers have multiple functionalities) [126,127]. Dispersants [30,128–131], diluents [33,132–134], defoamers [135,136], plasticizers [32,133], and light absorbers [32,84,137–140] are other possible components of a photocurable suspension. All the components must be carefully selected to create a proper feedstock.

VP ceramic suspensions must fulfill some process requirements [25]. For instance, ceramic suspensions must contain a high amount of ceramic filler for ensuring high density and suitable mechanical properties after sintering. A ceramic loading greater than 40 vol% is necessary for avoiding defects during post-processing, such as delamination [26] and cracks [27]. Cracks and voids are the primary cause of defects in ceramics since they reduce their mechanical strength due to low fracture toughness [78]. Low viscosity is another essential requirement. VP commonly employs a movable blade to recoat each cured layer with a micrometric layer of uncured resin. The uniformity and homogeneity of this recoating layer are essential requirements in ceramic VP. According to Dufaud et al. [141], the shear rate, $\dot{\gamma}$, caused by the recoating blade moving at a speed v in a layer with thickness e can be approximated by Equation 1 (drag flow in parallel plates). During recoating, the shear rate usually ranges between 30 and 100 s⁻¹ [142], and the viscosity of the suspensions should be lower than 3 Pa.s towards the achievement of proper fluidity [9,26,37]. This upper limit has been observed in most studies [25,28,33,78,128,130,131,134,143], although a few have worked with formulations exceeding 15 Pa.s [3,64,65,140] in some industrial printers [64,65]. Excessive viscosity hampers the attainment of uniform thin layers (typically between 25 and 100 micrometers) [28]. However, the meeting of both requisites is a difficult task, since the higher the solid loading, the higher the viscosity.

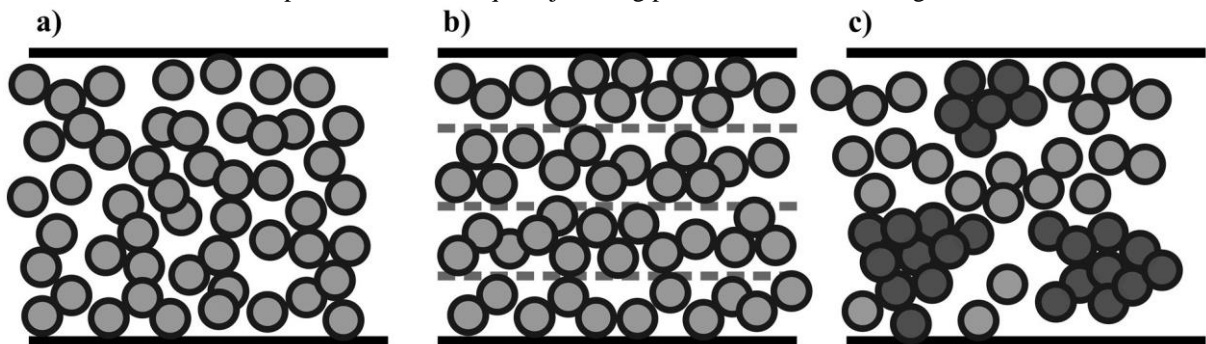
$$\dot{\gamma} = v/e \tag{1}$$

2.6.1 Rheological Behavior

2.6.1.1 Non-Newtonian behavior

Highly loaded ceramic suspensions for photopolymerization are usually strongly non-linear due to the dispersed solid phase [144], although the monomers and diluents used as a continuous phase generally display a Newtonian behavior [145]. Because of the multiphase characteristic of ceramic suspensions, the rheological behavior is influenced by the properties of the continuous medium, dispersed phase, and, remarkably, interactions between phases [144]. In low to moderate solid loadings, ceramic suspensions exhibit a shear-thinning behavior [3,4,132,140,143,146–151,9,25,30,65,128–131] characterized by a viscosity decrease with an increasing shear rate. Shear-thinning occurs through deflocculation of the particles and their increased arrangement in layers, caused by a shear rate increase [152], as illustrated in Figure 17 (a and b). Such behavior is desirable in ceramic VP [25,141,147], since it prevents the sedimentation of the suspension at rest and promotes adequate flow when a shear rate is applied [78].

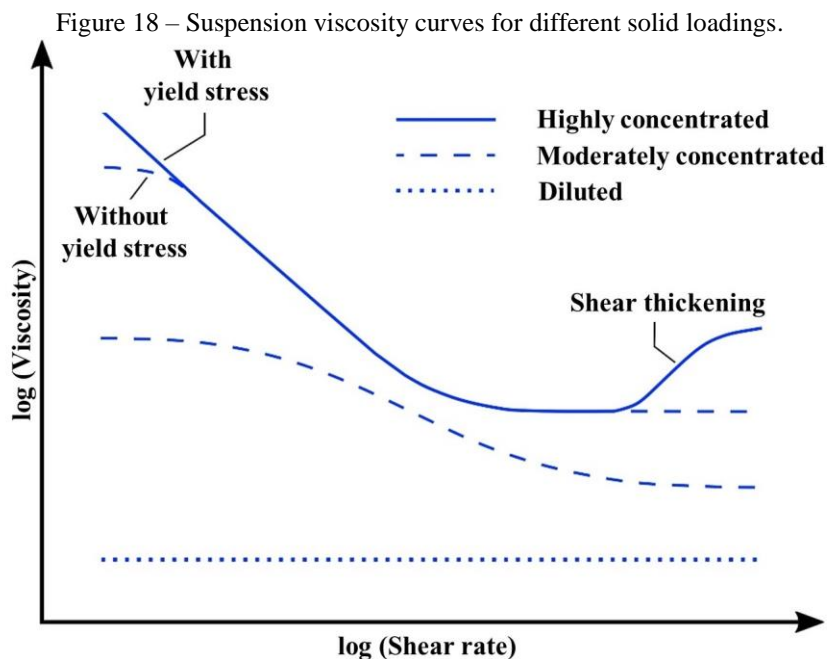
Figure 17 – Organization of particles according to the flow in a highly loaded suspension. a) Particles at rest; b) the ordering of particles in layers promotes shear-thinning; c) destruction of the layered organization of the particles and subsequent jamming promote shear-thickening.



Source: Adapted from [24,153].

On the other hand, highly loaded ceramic suspensions may display a shear thickening behavior, characterized by a viscosity increase with increasing shear rate, mainly in colloidal solutions (particles of at least one dimension between 1 nm and 1 μm) subjected to high shear rates [154]. This phenomenon can be explained by a disarrangement in the layered flow of the particles, which start jamming (Figure 17c), dissipating energy, and, consequently, increasing viscosity [155,156].

The rheological behavior is strongly affected by the solid fraction. Figure 18 depicts some behaviors characteristic of ceramic suspensions with different concentrations of solids. Very diluted suspensions tend to maintain a Newtonian behavior, moderately concentrated solutions display a shear thinning behavior with Newtonian plateaus at low and high shear rates, and highly concentrated solutions may show shear thickening at high shear rates. Brownian motion dominates the suspension behavior of colloidal suspensions for moderate and highly concentrated suspensions, maintaining the particles randomly distributed in a state of thermodynamic equilibrium, with some aggregation, thus resulting in higher viscosity [144,157] at the first Newtonian plateau (low shear rate $\dot{\gamma} \rightarrow 0$). On the other hand, at the second Newtonian plateau (moderate to high shear rate), the flowing particles achieve an optimum layered arrangement, resulting in minimum viscosity [144,157].

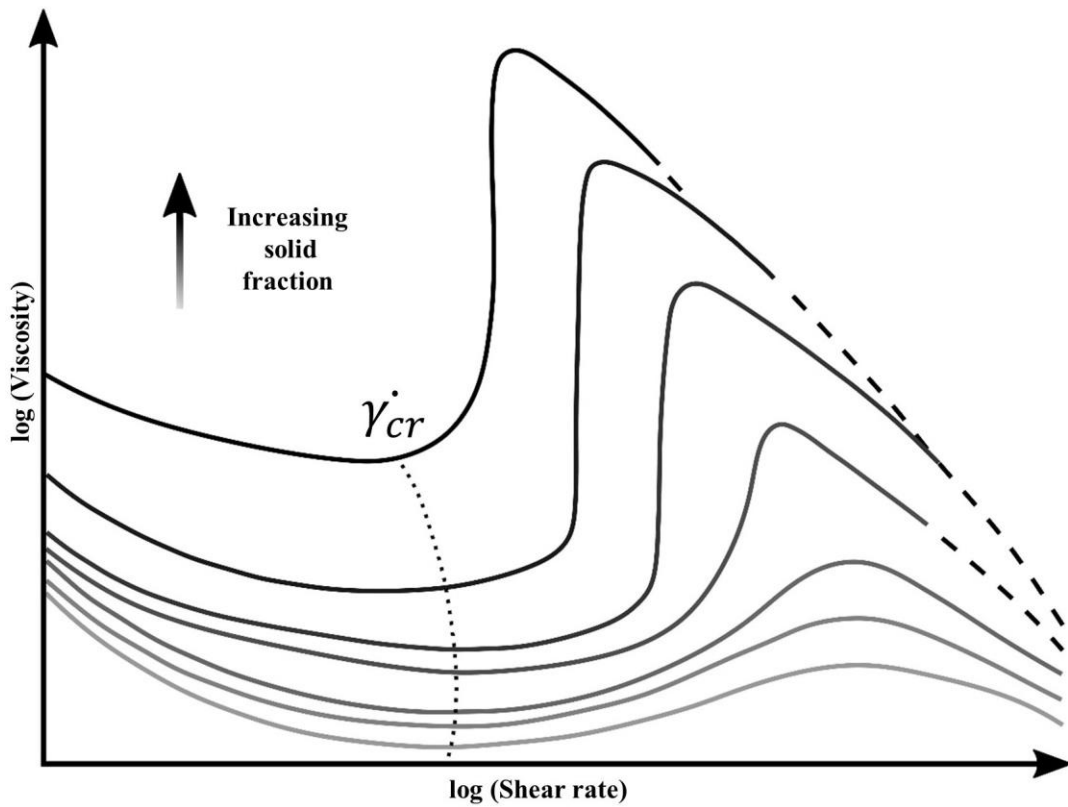


Source: Adapted from [24,144]

Several studies reported a transition from shear-thinning to shear-thickening behavior [29,33,78,158]. The presence and intensity of this shear-thickening transition are related to factors, such as choice of monomers [64], dispersants [66], dispersant quantity [28,66], particle size [107,156], and particle size distribution of ceramic powder [159]. The critical shear rate, $\dot{\gamma}_{cr}$, characterizes the onset of shear thickening behavior [144]. Figure 19 shows $\dot{\gamma}_{cr}$ decreases with an increasing volume percentage of solids and higher solid loadings also results in a more intense shear thickening behavior [145], undesirable for the photopolymerization of ceramic suspension, since it hampers a uniform spreading of new layers. Therefore, it must be avoided

by either reducing the shear rate (increasing production time) or modifying the suspension formulation (e.g., lowering solid loading or adding diluent or dispersant).

Figure 19 – Representation of the rheological behavior of suspensions that show a transition from shear-thinning to shear-thickening behavior. The critical shear rate $\dot{\gamma}_{cr}$ decreases with increasing solid loading.



Source: Adapted from [24,160].

2.6.1.2 Yield stress

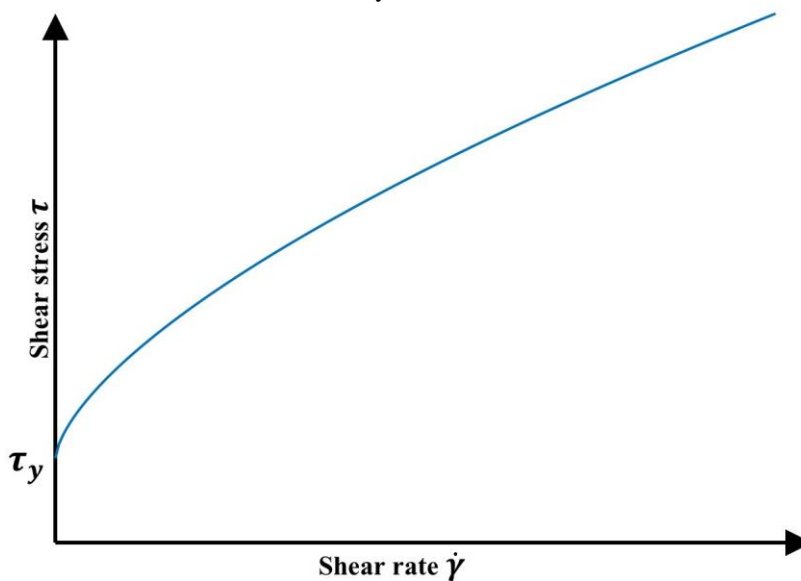
Ceramic suspensions with high solid loading may show yield stress τ_y , only flowing when the yield stress is exceeded. When subjected to minor efforts, they exhibit a solid-like behavior [161] caused by the interactions of the particles, which form a tridimensional microstructural network, preventing flow [130,162]. Although yield stress has been considered a problem for recoating new layers [26,130], some authors claim it is desirable in some applications, such as the manufacture of suspended parts with no support [161] and prevention of spontaneous flow [163]. As expected, the yield stress increases with a solid loading increase [28,130].

Herschel-Bulkley's model [164] relates stress τ to shear rate $\dot{\gamma}$ and yield stress τ_y , as shown in Equation 2. The adjustable parameter K is called the flow consistency index, and the

exponent n is the flow behavior index, representing a deviation from a Newtonian behavior ($n = 1$) [28]. If n is lower than one, it denotes a shear-thinning behavior; however, if it is higher than one, it represents a shear-thickening behavior. Several studies of ceramic VP have employed this model [28,62,146,163]. Figure 20 depicts a typical flow curve of a suspension with yield stress.

$$\tau = \tau_y + K\dot{\gamma}^n \quad (2)$$

Figure 20 – Representation of the rheological behavior of a suspension with yield stress according to Herschel-Bulkley's model.



Source: Adapted from an article resulting from this thesis [24].

2.6.1.3 Stability

Suspension stability is closely related to rheology. As a requirement to produce high-quality parts, photocurable ceramic suspensions should be homogeneous and stable for extended periods [29]. Unstable suspensions can promote concentration gradients on printed parts, especially for parts that require long printing times [141,165]. Critically, unstable suspensions with deposition rates faster than layer printing time can cause sedimentation gradients on each layer, causing part delamination and failure during sintering [159]. The two main mechanisms that can negatively affect stability are sedimentation due to gravity and flocculation due to interparticle attraction [166].

Concerning sedimentation, the terminal settling velocity of the particles is a result of the equilibrium of viscous and gravitational forces [141,167]. Stokes's sedimentation law, which

includes only the effects of gravitational and viscous forces, has been employed to evaluate particle terminal velocity [106,130,141,158,159]. However, attention should be taken as this equation is only valid for very diluted suspensions ($\phi < 1$ vol%) [158,166]. Richardson and Zaki [168] updated Stokes's Law, including the solid fraction effect (Equation 3), and validated the equation for particles larger than 100 μm .

$$V_{\text{settling}} = \frac{d^2(\rho_{\text{solid}} - \rho_{\text{fluid}})g}{18\eta_{\text{fluid}}} (1 - \phi)^{4.65} \quad (3)$$

Some general principles can be driven from this equation. The following factors can reduce suspension sedimentation: reducing particle size d , reducing density difference ($\rho_{\text{solid}} - \rho_{\text{fluid}}$), increasing the fluid viscosity η_{fluid} , and increasing solid fraction ϕ [159]. Usual ceramic formulations for VP have high solid loading and small particles; therefore, applying this equation would result in negligible theoretical sedimentation velocity.

However, in colloidal suspensions, Stokes's Law is not valid [169] (consequently, neither is Richardson-Zaki's equation). As particle size reduces, gravity and buoyancy become negligible [167], while interparticle forces, Brownian motion, and diffusion caused by concentration gradient become relevant [130,167,169]. For small particles, flocculation is the primary destabilization mechanism, enhancing sedimentation because large particle aggregates sediment faster. Therefore, dispersants are fundamental for minimizing interparticle attraction and maintaining suspension stability. Dispersants will be further discussed in section 3.4.

To evaluate stability, many authors use simple sedimentation tests [28,30,141,143,166,170,64,84,106,128,130–132,140]. In these tests, the suspensions are placed in graduated cylinders and have their sedimentation interfaces height measured in predetermined time intervals, enabling qualitative comparisons of multiple suspensions tested simultaneously. However, the visual evaluation of the suspension might be insufficient to expose the underlying destabilization mechanisms occurring at microscopic levels [171]. Moreover, the literature lacks a consensus or a standard practice on the solid concentration to be used and the duration of the experiment. More studies are necessary to define the maximum sedimentation velocity allowed for ceramic suspensions used in VP for both printing and storage stability. A more advanced stability measurement can be performed using light backscattering [140,165,171]. Such equipment (suitable for concentrated suspensions) measures the transmittance and backscattering of an infrared beam directed to the sample. When particle concentration decreases (either by flocculation or sedimentation), the backscattered

light intensity reduces, thus enabling a quantitative identification of sedimentation and flocculation. [171]. Finally, the analysis of fractal patterns on drainage suspension films is an interesting proposal for a fast evaluation of dispersant stabilization effectiveness [158,166]. Within a few minutes, this technique obtained results comparable to sedimentation tests, which demand many hours or days.

2.6.2 Influence of formulation on the rheological behavior

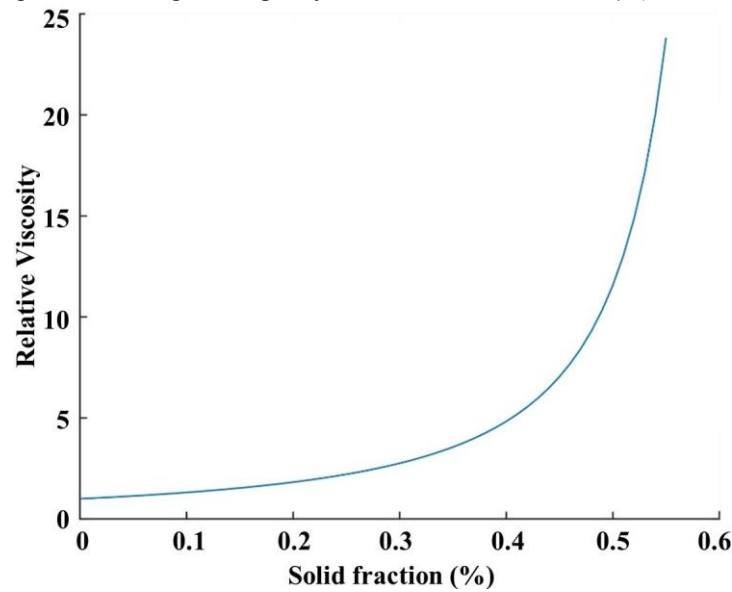
2.6.2.1 Volumetric solid fraction

As previously addressed, the volumetric solid fraction plays a crucial role in the rheological behavior of the suspension, since it affects both critical shear stress and yield stress of the ceramic slurry. Because solid loading is inversely related to the suspension viscosity, finding an optimum compromise between such factors is essential.

A vital step towards an optimum compromise is to relate solid loading and suspension viscosity quantitatively. Modeling colloidal suspension behavior can be complex since it involves several phenomena, such as buoyancy, hydrodynamic flow, Brownian motion, Van der Waals interaction, and dispersion mechanisms. Many authors have simplified analyses using hard spheres models, which consider all particles rigid spheres of the same size, suspended in a Newtonian medium, with no interaction or gravitational effects [172].

Such models relate both viscosity and volumetric percentage of solid loading in suspensions for a given shear rate. Krieger-Dougherty's model [173], a prominent hard spheres model, has shown excellent agreement with experimental data in several studies involving ceramic suspension for VP [28,107,130,132,148,170]. It is described by Equation 4 where η_r is the relative viscosity, η_s is the suspension viscosity, η_0 is the medium viscosity, ϕ is the percentual volumetric solid loading, ϕ_m is the maximum volumetric solid loading (maximum packing), and B is Einstein's coefficient (also called intrinsic viscosity). Adjustable parameters ϕ_m and B are dependent on particle shape and size distribution and can be fitted experimentally. Parameter B equals 2.5 for monodispersed, neutrally buoyant, non-interacting, hard spherical particles. In this model, the relative viscosity increases sharply as the solid fraction approaches the maximum, as illustrated in Figure 21.

$$\eta_r = \eta_s/\eta_0 = (1 - \phi/\phi_m)^{-B\phi_m} \quad (4)$$

Figure 21 – Krieger-Dougherty's model with $B = 2.5$ and $\phi_m = 63.7\%$.

Source: Adapted from an article resulting from this thesis [24].

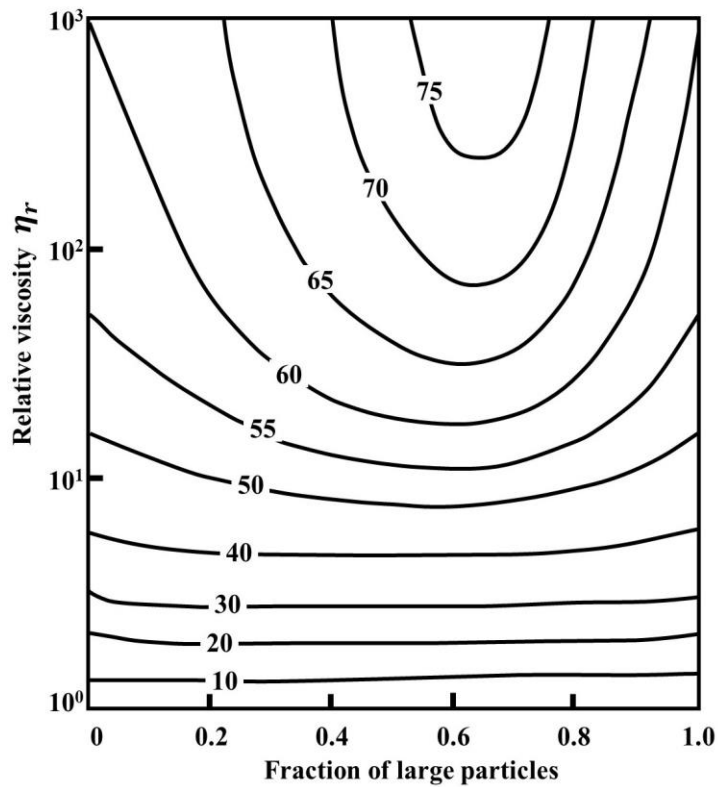
2.6.2.2 Particle size and shape

The addition of rigid particles to a liquid alters the hydrodynamic flow field. At low concentrations, the average interparticle distance is large, resulting in a minor viscosity increase due to a small hydrodynamic disturbance [162]. However, as the distance between particles decreases, the interparticle interaction becomes prominent. Notably, if the particles are smaller than $1\ \mu\text{m}$, the colloidal forces caused by Brownian motion and Van der Waals dominate the suspension behavior [154,157,162]. Therefore, fine powders result in higher viscosity than coarser ones and are more prone to agglomeration due to their large specific areas [131]. On the other hand, fine particles are more reactive than larger ones during sintering, which results in denser parts with better mechanical properties [23,132,174]. Therefore, the average of the particles in ceramic slurries for additive manufacture usually ranges between 90 and 500 nm [4,8,129,130,143,146,156,158,175–178,28,179,180,33,36,37,66,76,107,128].

Another essential aspect is particle size distribution. Figure 22 displays the effect of particle size on the relative viscosity for different levels of solid loading [157]. As can be seen, the size distribution exerts a negligible effect on dilute suspensions, since the average interparticle distance is considerable. However, as the solid fraction increases towards its maximum packing, the particle size distribution effects are significant. A large particle size ratio enables smaller particles to flow in the interstices of the larger ones [145,157,181–183], as illustrated in Figure 23. Consequently, suspensions with a broader particle size distribution may show higher fluidity. Wozniak et al. [145] mixed nanometric and micrometric particles, obtaining a bimodal suspension with lower viscosity (as predicted by Farris's theory [184]) and

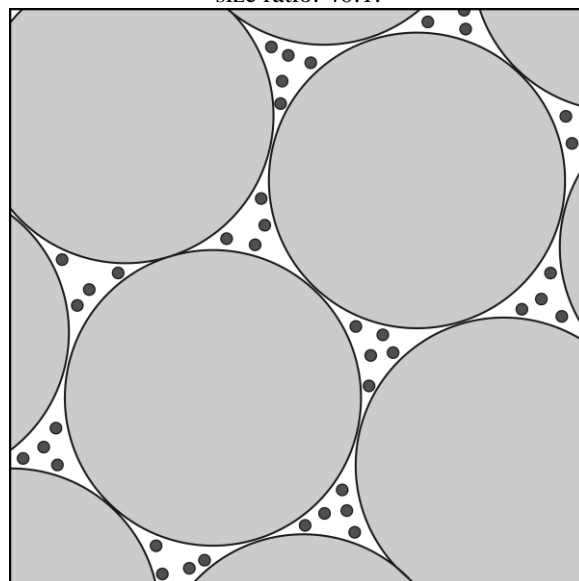
less shear-thickening behavior than monomodal suspensions. An optimal particle size distribution can be estimated by this theory, resulting in lower viscosity and maximum packing [65,184].

Figure 22 – Effect of the fraction of large particles on the viscosity of a bimodal suspension, for different levels of solid loading (10 to 75 vol%). The particle size ratio is 5:1.



Source: Adapted from [24,157].

Figure 23 – Schematic representation of smaller particles free to flow in the interstices of large particles. Particle size ratio: 40:1.



Source: Adapted from an article resulting from this thesis [24].

Moreover, nanoparticles can increase the stability of a suspension made of coarse particles. The fine particles increase the viscosity of the fluid surrounding the coarser particles [168,184], thus reducing the settling velocity, as indicated by Equation 3. Ding et al. [30] used 1 wt% of nanoparticles to avoid sedimentation of a micro-sized slurry for as long as 60 hours. Song et al. [140] and Pfaffinger et al. [84] also used nanoparticles to increase suspension stability at the cost of considerably increasing viscosity.

Superficial area and particle shape (which can be characterized by the aspect ratio) also considerably modify the rheology. In suspensions with non-spherical particles (with a higher aspect ratio), the effective maximum solid loading is reduced [157], resulting in higher viscosity. For instance, homogeneous suspensions of fibers with large aspect ratios are difficult to prepare and handle [107].

2.6.2.3 Monomers and diluents

According to Krieger-Dougherty's model (Equation 4), the suspension viscosity is proportional to the medium viscosity multiplied by the effect of the addition of particles. Therefore, the medium viscosity should be as low as possible so that suspensions with high solid fraction and moderate viscosity can be achieved.

The monomer is the main constituent of most photocurable resins, which highlights the importance of a proper monomer selection. Different types of acrylate (and methacrylate) monomers are used in the formulations of most reviewed studies (see Table 2). Commercial formulations will not be discussed here since both their composition and chemical nature have not been fully reported.

The number of reactive functional groups of a monomer plays a crucial role in polymerization. Multifunctional monomers promote cross-linking during polymerization, increasing the printed part strength and hardness compared to monofunctional monomers [25,26,158]. Figure 24 illustrates the polymerization of a monofunctional monomer and a multifunctional one and the effect of cross-linking. In general, the greater the number of functional groups, the greater the viscosity, as inferred from Table 2. For instance, monofunctional monomers are also called reactive diluents due to their low viscosity [25,185].

Table 2 – Properties of monomers used in ceramic vat photopolymerization.

Index	Monomer	Functionality	Molar mass g mol ⁻¹	Density g cm ⁻³	Viscosity mPa.s	Refractive index	Reference
	Acrylamide	1	71	1.322	Solid	-	[37,132,149,178,179,181,186]
2HEA	2-Hydroxyethyl acrylate	1 ^{OH}	116	1.011	8-10	1.445-1.45	[25,129,130,145]
HEMA	2-Hydroxyethyl methacrylate	1 ^{OH}	130	1.073	6-11	1.453	[25,147,187]
4HBA	4-Hydroxybutyl acrylate	1 ^{OH}	144	1.039-1.041	10-25	1.452-1.454	[145]
APTMS	3-(Trimethoxysilyl)propyl acrylate	1 ^{Si}	234	1.055	-	1.429	[140]
KH-570	3-(Trimethoxysilyl)propyl methacrylate	1 ^{Si}	248	1.045	-	1.431	[143,188]
ACMO	4-Acryloylmorpholine	1	141	1.122	12-15	1.512	[64,131]
IBOA	Isobornyl acrylate	1	208	0.98-0.99	2-9	1.476	[25,27,147,185]
IDA	Isodecyl acrylate	1	212	0.875	1-10	1.440-1.442	[25]
PHEA	2-Phenoxyethyl acrylate	1	192	1.104	5-15	1.518	[25]
MBAM	N-N'-Methylenebisacrylamide	2	154	1.235	solid	-	[37,132,149,178,179,181,186]
BDDA	1,4-Butanediol diacrylate	2	198	1.051	8	1.456	[147]
HDDA	1,6-Hexanediol diacrylate	2	226	1.01 – 1.03	5-10	1.455-1.457	[8,25,129,130,133,140,143,146,147,150,151,158,27,159,177,180,185,188–193,28,194–197,36,64–66,78,128]
HDEODA ⁺	1,6-Hexanediol ethoxylate diacrylate	2	314	1.01-1.05	10-30	1.461	[33]
DEGDA	Di(ethylene glycol) diacrylate	2	214	1.118	12	1.463	[147]
TEGMA	Tri(ethylene glycol) dimethacrylate	2	286	1.07-1.09	5-30	1.461	[98]
TTEGDA	Tetra(ethylene glycol) diacrylate	2	302	1.11	5-30	1.465	[187]
PEGDA ⁺	Poly(ethylene glycol) diacrylate (200-400)	2	308-508	1.11-1.12	15-65	1.463-1.467	[14,35,129,131,145,151,193]
TPGDA	Tri(propylene glycol) diacrylate	2	300	1.030	10-15	1.450	[15,198]
PPGDMA ⁺	Poly(propylene glycol) dimethacrylate (400)	2	536	1.002-1.01	30-50	1.450	[185]
NPGPO2DA	Neopentyl glycol (PO)2 diacrylate	2	328	1.007	10-30	1.440-1.447	[27,64]
BPAE2DMA	Bisphenol A bis(2-hydroxyethyl ether) dimethacrylate	2	453	1.120	1800	1.542-1.544	[141]
UDMA	Diurethane dimethacrylate	2	471	1.110	8500	1.485	[98]
TMPTA	Trimethylolpropane triacrylate	3	296	1.109-1.11	80-140	1.474	[8,25,28,130,140,143,158,188,194]
TMPETA ⁺	Trimethylolpropane ethoxylate triacrylate	3	693	1.102-1.11	60-120	1.471	[185,187]
Di-TMPTA	Di(trimethylolpropane) tetraacrylate	4	467	1.101-1.15	350-800	1.479	[33,36,64,65]
EPTTA ⁺	ethoxylated pentaerythritol tetraacrylate	4	550-718	1.139-1.16	100-200	1.475	[133,146,150,159,177,180,190,191]
DPHA	Dipentaerythritol penta-/hexa- acrylate	5/6	523-579	1.155	4000-7000	1.488-1.49	[33]

Data on properties were compiled from papers and commercial suppliers (Sigma-Aldrich, Green Chemical, Alpha-chemistry, Esschem Europe). This table is provided only for comparative purposes, since the measurement conditions may change.

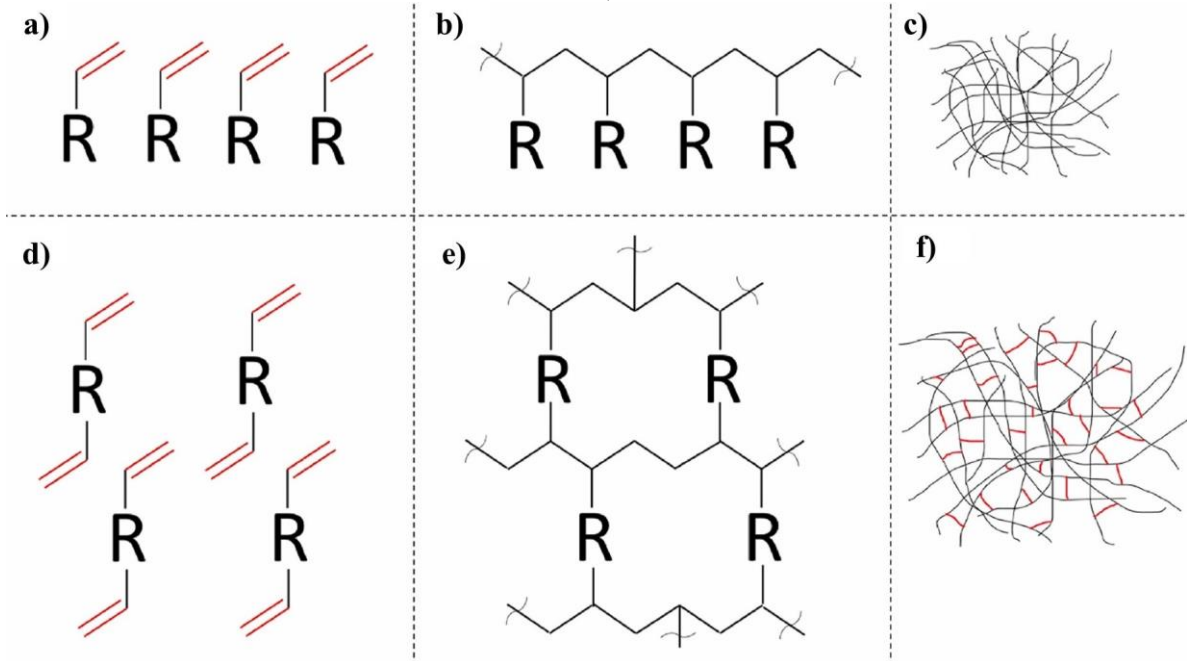
^{OH}Monomers with hydroxyl functional group

^{Si}Silane couplings

⁺ Polymeric compounds may display different properties due to differences in average molecular weight.

Source: Adapted from an article resulting from this thesis [24].

Figure 24 – Comparison of mono and multifunctional monomers: a) monofunctional monomers; b) linear polymerization of monofunctional monomers; c) entanglement of linear polymeric chains; d) bifunctional monomers; e) network polymerization of bifunctional monomers; f) polymeric network with cross-linking (in red).



Source: Adapted from an article resulting from this thesis [24].

Nonreactive solvents are also commonly used in ceramic resin formulations. Although inert diluents do not contribute to the mechanical resistance of the green printed parts, they improve refractive index matching [26] and plasticity [133] and reduce viscosity [33,134,185] and polymeric shrinkage [33,133] (which minimizes warping and delamination of the green parts). Furthermore, 1-octanol also displays antifoaming properties [141]. However, very volatile diluents, such as methanol and ethanol, are not recommended since they promote more warping and cracking than diluents that decompose during debinding [33,106]. A list of diluents found in ceramic photopolymerizable resins is provided in Table 3.

Table 3 – Properties of diluents used in ceramic vat photopolymerization.

Diluent	Molar mass g mol ⁻¹	Boiling point °C	Density g cm ⁻³	Viscosity mPa.s	Refractive index	Reference
Water	18	100	1.00	0.89	1.333	[37,132,149,178,179,181,186]
Methanol	32	65	0.791	0.5	1.329	[98,106,175,199]
Ethanol	46	78	0.789	1	1.36	[106,187]
Isopropyl alcohol (IPA)	60	82	0.785	2	1.377	[140]
1-Octanol (capryl alcohol)	130	196	0.827	7.2	1.429	[150,177,191,192]
Benzyl alcohol	108	203-205	1.045	5.5	1.539	[66,78]
Phenoxyethanol (POE)	138	244-246	1.107	-	1.539	[187]
1,5-pentanediol	99	202	1.028	86	1.47	[3,106]

Glycerol (glycerin)	92	182	1.25	954	1.474	[37,132,149,179,181,186]
Polyethylene glycol (PEG) ⁺	200-600	>150	1.124-1.128	60-100	1.46-1.47	[3,33,106,133,150,180,192]
Polypropylene glycol (PPG) ⁺	400	200	1.01	50-100	1.447-1.451	[146]
Decahydronaphthalene (decalin)	138	189-191	0.896	2-3	1.474	[158,185]
1-Methyl-2-pyrrolidone (NMP)	104	242	0.994	2	1.45	[106]
Butoxyethyl acetate (BEA)	160	192	0.942	2	1.413	[33]
Camphor	152	204	0.99	solid	-	[134]

Data on properties were compiled from papers, commercial suppliers (Sigma-Aldrich), and PubChem chemistry database. This table is provided only for comparative purposes, since the measurement conditions may change.

⁺ Polymeric compounds may display different properties due to differences in average molecular weight.

Source: Adapted from an article resulting from this thesis [24]

The affinity of the liquid medium with ceramic particles is fundamental for suspension homogenization. Ceramic particles such as alumina, silica, and zirconia have hydroxyl groups on their surfaces, which makes their powders hydrophilic [128]. For instance, the use of OH-terminated monomers (e.g., 2-HEA, 4-HBA, and HEMA) promotes hydrogen bonds and a solvation layer around the particles, thus reducing viscosity even without dispersant [25,129,145,187]. Reactive acrylate silane coupling monomers are also used for functionalizing ceramic surfaces [140,143,188]. Aqueous suspensions are another possible solution for particle affinity. Those reported in the literature [37,132,149,178,179,181,186] are primarily based on the formulation presented in a seminal paper on ceramic stereolithography by Griffith and Halloran [26]. Besides ceramic powder, the formulation includes water-soluble acrylamide and methylenebisacrylamide (MBAM) as monomers, a photoinitiator, dispersant, and water with glycerol as solvents. MBAM has two reactive sites and acts as a cross-linker. The advantage of aqueous formulations is their low viscosity compared to viscous non-polar acrylates. However, one of their drawbacks is a large amount of water, which must be removed before sintering. The shrinkage caused by drying can be as high as 14%, eventually promoting delamination and warping [132,178]. Desiccation with liquid PEG400 seems to produce a more uniform water removal, reducing warping problems [178]. Another disadvantage of this type of suspension is that the mechanical strength of green printed parts is lower than those of non-aqueous suspensions [107].

Furthermore, the refractive index of the medium should be considered. According to the Beer-Lambert law, the cured depth thickness is inversely proportional to the square of the difference between the refractive index of the medium and the particles $(n_{ceramic} - n_{medium})^2$ [26,181]. Therefore, a liquid medium whose refractive index is closer to that of ceramics

increases the cured layer and the overall printability [26,145]. Table 4 shows the refractive indexes of some printed ceramics. Since the refractive index of water is lower than those of most ceramics ($n = 1.33$), aqueous formulations result in thinner cured depth due to the higher refractive index difference. Glycerol is added to aqueous formulations for increasing the medium refractive index without compromising the suspension viscosity significantly [26].

Table 4 – Refractive index for some printable ceramic materials.

Ceramic	Refractive index	Reference
Alumina (Al_2O_3)	1.52-1.70	[26]
Silica (SiO_2)	1.56	[26]
Silicon Nitride (Si_3N_4)	2.10	[26]
PZT	2.5	[141]
Zirconia (ZrO_2)	2.176-2.2	[25,28]

Source: Adapted from an article resulting from this thesis [24].

Most formulations reported for ceramic VP are based on non-aqueous formulations, given the greater depth of cure and better mechanical resistance of the resulting green parts in comparison to those of aqueous solutions. However, the hydrophilic character of the surface of ceramic particles reduces the powder dispersibility in a non-polar medium [107]. A way to solve the affinity problem is to make the hydrophilic surface of the oxide compatible with the hydrophobic medium through dispersants [200,201] (which will be further explained in the next section).

Among the non-aqueous formulations for ceramic VP, the most used acrylate monomer is HDDA (1,6-hexanediol diacrylate), employed for ceramic VP since 1996 [26]. This difunctional acrylate shows good agreement among low viscosity, mechanical resistance (due to cross-linking), and diffusion-controlled degradation during debinding [158]. However, its high polymerization shrinkage [185] creates internal stresses during curing, which leads to delamination and brittle behavior of the part [140,146,158]. Although some authors used HDDA alone [23,128,195–197], better results were achieved when it was combined with monomers of higher functionality for enhancing cross-linking and with inert diluents or monofunctional monomers. For instance, several authors combined HDDA with TMPTA [8,28,30,130,140,143,158,188,194], a viscous trifunctional acrylate with lower polymerization shrinkage, for increasing the hardness of the printed part [140]. Other combinations of monomers and diluents are provided in Table 5.

Table 5 – Some combinations of monomers and diluents for ceramic VP.

Monomer	Inert diluent	Reference
HDDA		[23,128,195–197]
HDDA + EPTTA		[190]
HDDA + IBOA + PNPGBDA		[27]
HDDA + Genomer 5695	Benzyl alcohol	[66,78]
HDDA + 2HEA + TMPTA		[130]
HDDA + TMPTA		[8,28,30,140,194]
HDDA + TMPTA	Decalin	[158]
HDDA + TMPTA + Acrylate silane coupling		[143,188]
HDDA + TMPTA + Acrylate silane coupling	Isopropyl alcohol	[140]
HDDA + Di-TMPTA		[36,64,65]
HDDA + PEGDA		[151,193]
HDDA + PPTTA	PEG	[133,180]
HDDA + PPTTA	PPG	[146]
HDDA + PPTTA + PUA	PEG + 1-Octanol	[150,177,191]
HDDA + PUA	PEG + 1-Octanol	[192]
Acrylamide + MBAM	Water (+ glycerol)	[37,132,149,178,179,181,186]
HEMA + TEGDA	POE	[187]
HEMA + TMPETA		[187]
PEGDA		[35]
PEGDA + ACMO		[131]
PEGDA + 2HEA		[145]
PEGDA + 4HBA		[145]
PEGDA + 3,3-Dimethylacrylic acid	PPG	[14]
PNPGBDA + Di-TMPTA		[64]
TEGMA + UDMA		[98]
TMPTA + IDA		[25]
TMPTA + IBOA		[25]
TPGDA		[15,198]

Source: Adapted from an article resulting from this thesis [24] .

2.6.2.4 Dispersants

Ceramic particles, in which the surfaces are filled with several hydroxyl groups, have a strong tendency to agglomerate [131], thus increasing the suspension viscosity. Van der Waals forces promote an attractive potential between particles, especially in fine powders [131], causing the particles to aggregate in a strong flocculated state [154,162,202–204]. The Van der Waals potential can be reduced by suspending the particles in an index-matched solvent [145,154].

Dispersants can improve the manufacturability of highly loaded ceramic slurries [131] since their type and quantity significantly affect the rheological behavior [28] and stability [143] of suspensions. Their effectiveness can be evaluated by the viscosity and stability of the suspension.

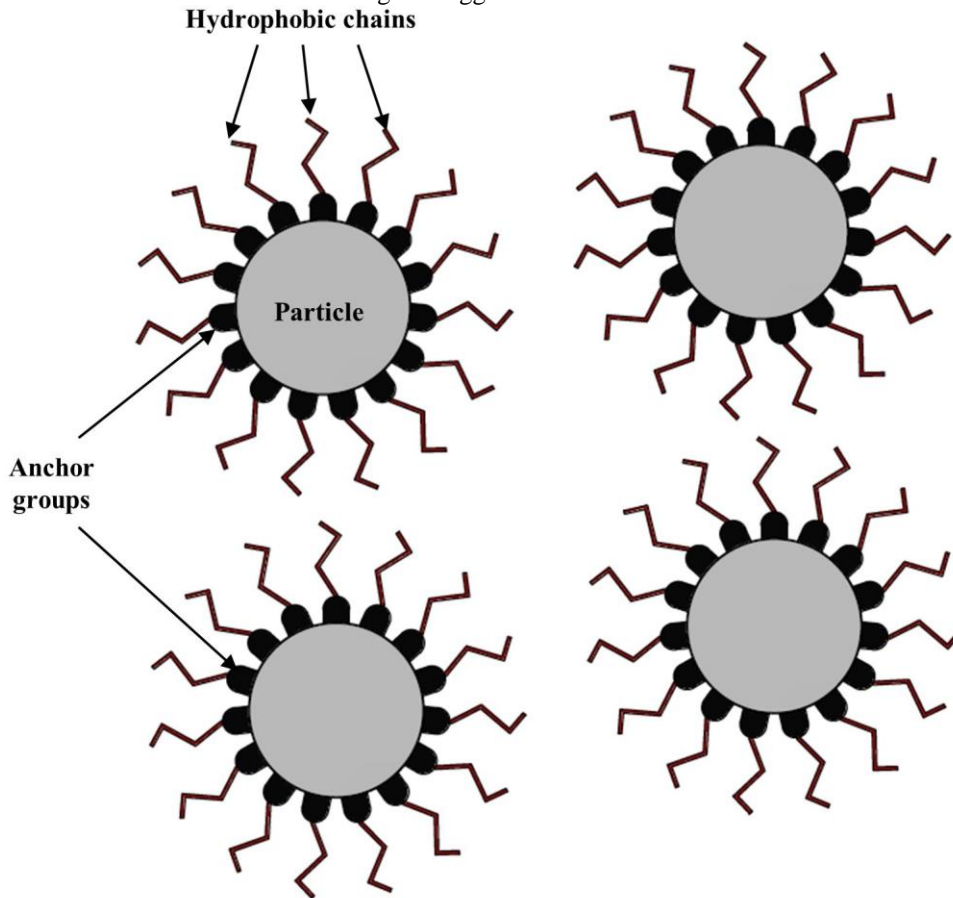
2.6.2.4.1 Dispersion and adsorption mechanisms

Dispersion mechanisms are classified into three main types. The first is electrostatic stabilization. In aqueous suspensions, a repulsive electrostatic potential can be generated if the surfaces of the particles are electrically charged. Opposed sign ions on the liquid are attracted to the particle surface forming a repulsive electric potential, which exponentially decreases with the distance [144,154] and is proportional to the dielectric constant of the suspension medium [144,154,162,204]. Water has a high dielectric constant, while those of non-polar solvents are much lower. Therefore, effective electrostatic stabilization is exclusive to aqueous suspensions [154,157,162] and can be neglected in non-polar polymeric solvents [205]. Furthermore, electrostatic stabilization alone might be insufficient for the achievement of a stable suspension. According to the DLVO theory, if the particles have sufficient energy to overcome the electrostatic repulsive barrier, they might fall on the primary minimum forming a very stable aggregate [154,162]. None of the reviewed articles used this type of stabilization solely.

The second type of dispersion mechanism is steric stabilization, which occurs through the adsorption of long organic molecules at the surface of the particles, generating repulsion force when the polymeric layer of two neighboring particles overlaps [162] and avoids their aggregation [144,154]. Unlike electrostatic stabilization, steric stabilization can disperse non-aqueous suspensions [144]. Due to the hydrophilic surface of ceramic particles, the stabilizing materials must have a hydrophilic anchor group that interacts with the particle surface and a hydrophobic chain soluble in the liquid medium. Consequently, a steric barrier that stabilizes the dispersed particles in the suspension is created [28,131,200], as illustrated in Figure 25.

The following conditions are required for a good steric dispersion [162,204]: complete coverage of particle surface by the steric layer, sufficient thickness of the adsorbed layer (>5 nm), medium as a good solvent for the stabilizing chain, and strong attachment of dispersant with the surface particle achieved with anchor groups of strong affinity with the surface. On the other hand, if the polymer is not attached to the surface, but freely moves dissolved in the solvent, it can produce depletion agglomeration instead of dispersion [154,162]. Therefore, the high affinity of the dispersant with both ceramic particle and solvent medium is fundamental for good dispersion, which can be evaluated with the use of contact angle measurements [64].

Figure 25 – Schematic illustration of steric stabilization. Dispersant molecules have polar anchor groups adsorbed in the ceramic surfaces and hydrophobic chains soluble in the medium, creating a protective layer against agglomeration.



Source: Adapted from an article resulting from this thesis [24].

Steric stabilization offers advantages when compared to electrostatic stabilization. Its steric repulsive potential is steeper than electrostatic potential [162]; therefore, the total potential has no primary minimum, enabling an easy redispersion of agglomeration [162,206]. Furthermore, steric stabilization is independent of the ionic concentration of the liquid medium and promotes good dispersion at intermediate pH values, whereas in electrostatic stabilization, a better dispersion is achieved at extreme pH values [162,206].

Finally, the third type of dispersion mechanism is electrosteric stabilization, which combines both types of stabilization. Polyelectrolytes, which are polymers charged along the length of the polymeric chain (in contrast to those with charged species only at the molecule terminations) [207], promote a steric barrier and an electrostatic potential [154]. The superficial charge of the particles, altered by the pH, can either increase or decrease polymer adsorption on the surface [154,206]. The electrosteric mechanism yields good results for aqueous suspensions. Wang et al. [149] tested some of the most used dispersants for aqueous suspensions, namely ammonium polyacrylate, sodium polyacrylate, polyvinylpyrrolidone, and

polyacrylic acid, and reported ammonium polyacrylate, which is a polyelectrolyte, resulted in the lowest viscosity suspension.

The adsorption of steric dispersants can be classified as either chemical or physical [203]. In chemical adsorption, molecules chemically react with the surface, forming covalent bonds. This process requires a considerable amount of energy since it involves disruption and formation of covalent bonds, which can have the magnitude of hundreds of kilojoules [208]. Thus, this type of adsorption usually requires an additional step before mixing the powder with the resin [203]. The ceramic particles are previously mixed with the dispersant and a solvent (such as ethanol [128,130,131,146,151,158,193] or acetone [129]) and then stirred in an ultrasonic mixer, ball mill, or planetary mill. Finally, the powder is dried for the elimination of the solvent and eventually heated for enhancing chemical reactions, and then sieved. This two-step process is employed for suspensions that use carboxylic acids (monocarboxylic [23,128,129,131] and dicarboxylic acids [130]) and silane couplings [64,131,140] as dispersants. The effectiveness of the dispersant adsorption in the ceramic surface can be assessed by FTIR spectroscopy of the modified particles [28,64,129,130,142,170].

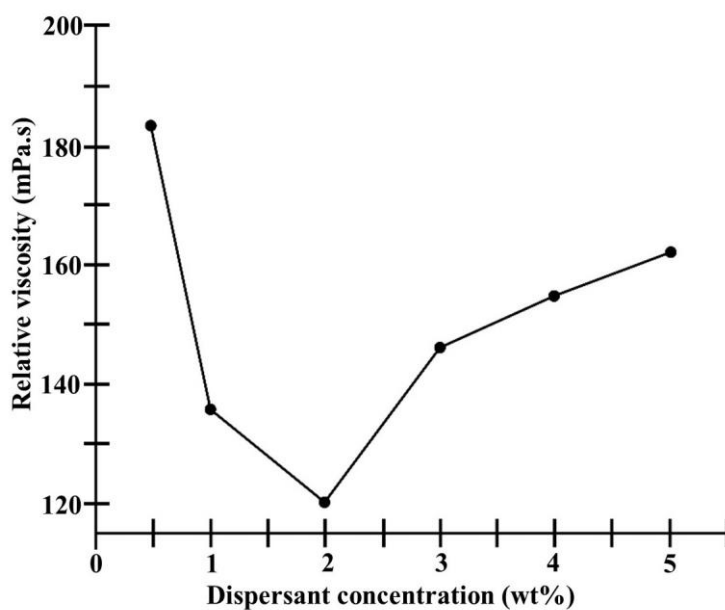
On the other hand, in physical adsorption, Van der Waals bonds occur between the adsorbent and the adsorbent surface and do not require a large amount of energy, reaching a maximum of a few kilojoules [208]. Examples of such interactions are hydrogen bonds between hydroxyl groups present on the surfaces of oxides and the oxygen of carbonyl groups of esters [209] or ethoxy segments [210,211]. Mixing requires no preliminary step, enabling ceramic particles, dispersants, and resins to be mixed at once [203]. Several commercial dispersants with long polymeric chains were mixed in this single-step process (e.g., KOS110 (Guangzhou Kangoushuang) [8,28], BYK w969 [25], DISPERBYK-180 [27] (BYK-Chemie), and Variquac CC 42 (Evonik) [190,212]).

2.6.2.4.2 Optimum amount of dispersant

It must be highlighted that the addition of dispersants has an optimum point of minimum viscosity, resulting in a more viscous suspension for lower or higher amounts of dispersant [37]. This phenomenon was reported by Zhang et al. [28], who varied the amount of dispersant in a suspension with 40 vol% zirconia particles at a constant shear rate (Figure 26). Wang et al. [132] demonstrated the dosage of dispersant should be proportional to the superficial area of the powder rather than to its weight since adsorption is a superficial effect. A low amount of dispersant can result in incomplete coverage of the particle surface, hence, flocculation will

occur [203,213]. On the other hand, a large amount of dispersant above the adsorption limit increases the suspension viscosity, since the excess dispersant is diluted in the medium [30,213]. The use of the optimum amount of dispersant, which is associated with the limit of adsorption of the Langmuir isothermal adsorption model [130,203], reduces suspension viscosity [28], shear-thinning behavior [28], and yield stress [28,130].

Figure 26 – Viscosity curve as a function of dispersant concentration.



Source: Adapted from [24,28].

2.6.2.4.3 Types of dispersants used in photosensitive ceramic suspensions

Polyvinylpyrrolidone (PVP K15) [37,178,179,181] and polyelectrolyte ammonium polyacrylate (PAA-NH₄) [132,149] were used as dispersants for water-soluble formulations. Although they can also be employed with non-polar acrylates formulations, other dispersants seem to be more effective [106,128].

Several types of materials have been used as dispersants in formulations for vat photopolymerization based on non-polar acrylates, including several commercial hyperdispersants, which have at least one hydrophilic anchor group and one hydrophobic polymeric chain [213]. Although their chemical structure is not publicly available, the anchors are commonly functional groups of high polarity, such as amine [25,27,159,180,190,193,33,107,131,133,142,147,151,156], carboxyl [8,28,30,131,170,189,193], silane [64,131,140,143,188] and phosphoric acid/oxide

[151,158,195,196]. Table 6 shows a summary of dispersants reported in the literature that have yielded good results.

Table 6 – Dispersants used in formulations of ceramic slurries vat photopolymerization.

Name	Chemical description	Reference
Ammonium polyacrylate	Polyelectrolyte	[106,128,132,149]
Polyvinylpyrrolidone	Steric dispersant used in aqueous suspensions	[37,106,178,179,181]
Oleic acid	Unsaturated carboxylic acid (18 carbons)	[23,106,128,129,131,142,195]
Sebacic acid	Short-chain dicarboxylic acid (10 carbons)	[130,195]
KH560	Silane Coupling 3-glycidoxypropyltrimethoxysilane	[64,131]
MAEP	Monoalcohol ethoxylate phosphate	[195]
TOPO	Trioctylphosphine oxide	[158]
Not specified (BYK-Chemie)	Alkylamine dispersant	[133]
Not specified (BYK-Chemie)	High molecular copolymer	[194]
Not specified (BYK-Chemie)	A type of copolymer containing a phosphoric acid group	[151]
ANTI-TERRA-U 100 (BYK-Chemie)	Salt of unsaturated polyamine amides and low-molecular acidic polyesters	[180]
BYK-w 969 (BYK-Chemie)	A solution of a hydroxy-functional alkylammonium salt of an acidic copolymer A mixture of 2-phenoxyethanol and alcohol ammonia salt of an acidic polyester	[25,147]
DisperBYK (BYK-Chemie)	A solution of an alkylammonium salt of a low-molecular-weight polycarboxylic acid polymer	[131,193]
DisperBYK-103 (BYK-Chemie)	A solution of a copolymer with filler affinic groups	[142]
DisperBYK-111 (BYK-Chemie)	Copolymer with an acid group (also used combined with reactive acrylate silane couplings)	[140,142,143,188]
DisperBYK-142 (BYK-Chemie)	A solution of a phosphoric ester salt of a high molecular weight copolymer with pigment-affinic groups (Particularly suitable for stabilizing pigments in epoxy resins)	[196]
DisperBYK-180 (BYK-Chemie)	Alkylol ammonium salt of a copolymer with acidic groups	[27,142]
DisperBYK-2001 (BYK-Chemie)	A solution of a structured acrylate copolymer with pigment-affinic groups (electrosteric mechanism)	[134]
Hypermer KD-1 (Croda)	polyester/polyamine condensation polymer with a cationic head group	[33,156]
KOS110 (Guangzhou Kangoushuang Trade)	Copolymer dispersant containing a carboxylic acid group	[8,28,30,170,189]
Solsperse 41000 (Lubrizol)	100% active polymeric dispersant compatible with UV-curable systems	[66,197]
Triton X-100 (Sigma-Aldrich)	Octylphenol Ethoxylate is a non-ionic surfactant with a hydrophilic polyethylene oxide chain and an aromatic hydrocarbon hydrophobic group.	[142,147,156,214]
Variquac CC 42 NS (Evonik)	Polypropoxy quaternary ammonium chloride.	[107,131,190]

Source: Adapted from an article resulting from this thesis [24] .

Dispersants with carboxyl acids include fatty acids (long hydrocarbon chains with a single carboxyl group [215]), either saturated (e.g., stearic acid [128,129,131]) or unsaturated, with a double carbon bond (C = C) (e.g. oleic acid [23,106,128,129,131,142,195]), short-chain dicarboxylic acids [130], and commercial dispersants with one or more carboxyl groups (e.g. KOS110 [8,28,30,170,189] and DISPERBYK [131,193]). When used with acrylates, oleic acid shows better dispersion than stearic acid [128,129,131,195] and sebacic acid [195]. Its unsaturated chain seems to have a better affinity with the double bonds of non-polar acrylates, which explains its effectiveness [106,128]. On the other hand, stearic acid has displayed worse dispersion properties for polar ceramic particles dispersed in non-polar acrylates [64,128,129,131,141,195] and tends to foam, which demands an antifoaming agent [141]. The size of carboxylic acid affects dispersion. Sebacic acid, a dicarboxylic acid with ten carbons, has shown more effective in dispersing alumina in acrylate non-polar formulations than smaller dicarboxylic acids [130], due to the longer chain and consequent higher steric potential.

2.6.2.5 Best reported formulations concerning rheological behavior

Although most studies work with formulations with solid loading ≥ 40 vol% and viscosity ≤ 3 Pa.s, exceptions are studies that use highly viscous ceramic slurries in differentiated equipment. Li et al. [107] used Admaflex 130 (ADMATEC Europe BV, The Netherlands) to manufacture zirconia parts with viscosity around 7 Pa.s. This DLP equipment applies a tape casting technology for creating layers [156], and its transport system can handle high-viscosity suspensions [32]. Xing et al. [64,65] used Ceramaker 300 system (3D CERAM, France) to print ceramic parts with slurries with viscosity as high as 28.2 Pa.s.

Table 7 shows details of the formulations that fulfilled the desired requisites (≥ 40 vol% solid loading and ≤ 3 Pa.s viscosity). Formulations from the same authors were grouped for facilitating comparisons. Griffith and Halloran [26] and Wang et al. [132] printed ceramic parts using suspensions with a solid loading of 50 vol% or more. However, they used aqueous suspensions, which provided a cured ceramic green body of low strength [107], thus hampering post-processing, which explains its restricted use. On the other hand, all non-aqueous formulations described included monomer HDDA, which is generally a good fit due to its low viscosity (around 9 mPa.s [25]) and ability to create cross-linked networks [216].

Table 7 – Dispersants used in formulations of ceramic slurries for vat photopolymerization. Studies from the same research group are displayed in sequence.

Reference	Ceramic material	Particle size μm	Superficial area $\text{m}^2 \text{g}^{-1}$	Solid fraction vol%	Viscosity mPa.s	Monomer	Diluent	Dispersant																																																																																																										
[132]	Hydroxyapatite	5	0.6	52	1520	Acrylamide + MBAM 25 wt%, 1.5 wt%	Water + glycerol: 67 wt%, 6.5 wt%	Ammonium polyacrylate 0.3 mg/m ²																																																																																																										
[132]		1	2.1	52	2870				[26]	Silica	2.29	-	50	110	Acrylamide + MBAM 9:1 wt	(Water + glycerol) 50-70 vol%	Not detailed	[134]	Calcium Phosphate	1.57	4.2	48	160	HDDA	Camphor 40 wt%	DisperBYK-2001	[66]	Zirconia 3Y	0.09	7	45	2300	HDDA + Genomer 5695 52 wt%, 13 wt%	benzyl alcohol 35 wt%	Solsperse 41000 1 wt%	[66]	Zirconia 3Y + Alumina 4:1 wt	0.09 - 0.2	7 - 14.5	48	3000	[78]	Zirconia 3Y	0.09	7	44	1220	HDDA + Genomer 5695 54 wt%, 17 wt%	benzyl alcohol 29 wt%	Melpers 4350 3 wt%	[130]	Alumina	0.4	4.1	45	1620	HDDA+2HEA+TMPTA 6:3:1 vol	-	Sebacic acid 0.4 wt%	[145]	Alumina	0.4	3.7	40	2020	HDDA	-	Oleic acid 0.1 wt%	[151]	BaTiO ₃	0.5	2.3	40	230	HDDA+PEGDA400 1:1 vol	-	BYK 1 wt%	[193]	Alumina + Zirconia 3Y 3:1 wt	0.4	4.1	40	200	HDDA+PEGDA400 1:1 vol	-	BYK 5 wt%	[193]	0.4 - 0.2	-	40	380	[30]	SiC + nano SiC 99:1 wt.	15 - 0.4	-	40	480	HDDA+TMPTA 1:1 wt	-	KOS110 + 17000 5 wt%	[143]	Cordierite	0.35	-	40	1490	(HDDA + TMPTA) (1:4 vol)	-	Disperbyk-111 5 wt%	[156]	Zirconia 3Y	0.385	9	40
[26]	Silica	2.29	-	50	110	Acrylamide + MBAM 9:1 wt	(Water + glycerol) 50-70 vol%	Not detailed																																																																																																										
[134]	Calcium Phosphate	1.57	4.2	48	160	HDDA	Camphor 40 wt%	DisperBYK-2001																																																																																																										
[66]	Zirconia 3Y	0.09	7	45	2300	HDDA + Genomer 5695 52 wt%, 13 wt%	benzyl alcohol 35 wt%	Solsperse 41000 1 wt%																																																																																																										
[66]	Zirconia 3Y + Alumina 4:1 wt	0.09 - 0.2	7 - 14.5	48	3000				[78]	Zirconia 3Y	0.09	7	44	1220	HDDA + Genomer 5695 54 wt%, 17 wt%	benzyl alcohol 29 wt%	Melpers 4350 3 wt%	[130]	Alumina	0.4	4.1	45	1620	HDDA+2HEA+TMPTA 6:3:1 vol	-	Sebacic acid 0.4 wt%	[145]	Alumina	0.4	3.7	40	2020	HDDA	-	Oleic acid 0.1 wt%	[151]	BaTiO ₃	0.5	2.3	40	230	HDDA+PEGDA400 1:1 vol	-	BYK 1 wt%	[193]	Alumina + Zirconia 3Y 3:1 wt	0.4	4.1	40	200	HDDA+PEGDA400 1:1 vol	-	BYK 5 wt%	[193]	0.4 - 0.2	-	40	380	[30]	SiC + nano SiC 99:1 wt.	15 - 0.4	-	40	480	HDDA+TMPTA 1:1 wt	-	KOS110 + 17000 5 wt%	[143]	Cordierite	0.35	-	40	1490	(HDDA + TMPTA) (1:4 vol)	-	Disperbyk-111 5 wt%	[156]	Zirconia 3Y	0.385	9	40	2900	SP-RC700, Sprint Ray commercial resin	PEG400 25 vol%	Variquat CC-42 3 wt%																													
[78]	Zirconia 3Y	0.09	7	44	1220	HDDA + Genomer 5695 54 wt%, 17 wt%	benzyl alcohol 29 wt%	Melpers 4350 3 wt%																																																																																																										
[130]	Alumina	0.4	4.1	45	1620	HDDA+2HEA+TMPTA 6:3:1 vol	-	Sebacic acid 0.4 wt%																																																																																																										
[145]	Alumina	0.4	3.7	40	2020	HDDA	-	Oleic acid 0.1 wt%																																																																																																										
[151]	BaTiO ₃	0.5	2.3	40	230	HDDA+PEGDA400 1:1 vol	-	BYK 1 wt%																																																																																																										
[193]	Alumina + Zirconia 3Y 3:1 wt	0.4	4.1	40	200	HDDA+PEGDA400 1:1 vol	-	BYK 5 wt%																																																																																																										
[193]		0.4 - 0.2	-	40	380				[30]	SiC + nano SiC 99:1 wt.	15 - 0.4	-	40	480	HDDA+TMPTA 1:1 wt	-	KOS110 + 17000 5 wt%	[143]	Cordierite	0.35	-	40	1490	(HDDA + TMPTA) (1:4 vol)	-	Disperbyk-111 5 wt%	[156]	Zirconia 3Y	0.385	9	40	2900	SP-RC700, Sprint Ray commercial resin	PEG400 25 vol%	Variquat CC-42 3 wt%																																																																															
[30]	SiC + nano SiC 99:1 wt.	15 - 0.4	-	40	480	HDDA+TMPTA 1:1 wt	-	KOS110 + 17000 5 wt%																																																																																																										
[143]	Cordierite	0.35	-	40	1490	(HDDA + TMPTA) (1:4 vol)	-	Disperbyk-111 5 wt%																																																																																																										
[156]	Zirconia 3Y	0.385	9	40	2900	SP-RC700, Sprint Ray commercial resin	PEG400 25 vol%	Variquat CC-42 3 wt%																																																																																																										

Source: Adapted from an article resulting from this thesis [24].

Studies that employed more than 40% solid loading mixed monomers with inert diluents. A notable exception is the study of Zhang S. et al. [130], which used a monofunctional polar monomer with low viscosity (2-HEA) combined with cross-linkers HDDA and TMPTA and showed highly loaded suspensions with no inert diluents are feasible.

All selected studies used dispersants, and some included reactive acrylate surfactants with good affinity with ceramic particles, such as hydroxyl-terminated 2-HEA [130] and silane coupling KH-570 (3-methacryloxypropyltrimethoxysilane) [143]. This reactive surfactant simultaneously promotes the dispersion of the particles in the suspension and enhances the mechanical resistance of the printed part.

Moreover, particle size and shape exerted a prominent effect. Studies that employed higher solid loadings used particles larger than 1 μm diameter [26,30,132,134], which minimize the attraction forces and reduce viscosity – however, they are not ideal for sintering. If the mechanical resistance and porosity of a part are not a significant concern, larger particles might be a viable option. However, excellent results were also achieved for submicrometric particles with the use of superior ceramic grades of small surface area (more spherical particles), which enhanced flowability [66,78,130,145,151,193].

2.6.3 Curing Behavior and photosensitive parameters

Parts of this subsection have been published as a conference paper [24].

Understanding the curing behavior of the photosensitive suspensions is another important aspect to ensure the geometrical accuracy and good mechanical properties in the ceramic parts manufactured by VP [3]. In the DLP AM, the cure depth is a key factor for the interlayer combination [128] and it should be higher than the layer thickness to provide sufficient layer integration [3,33,78]. On the other hand, if the cure depth is too high, the accuracy will be impaired [3].

The photopolymerizable ceramic suspensions generally follow the Beer-Lambert Law [26,63,131,143], described by Equation 5.

$$C_d = S_d \ln\left(\frac{E}{E_c}\right) \quad (5)$$

Where C_d is the cure depth, S_d is the sensitivity of the suspension, also called penetration depth, E is the incident light energy density, and E_c is the critical energy (the minimum energy density to initiate polymerization for a suspension).

The penetration depth and the critical energy are photosensitive parameters of the suspension and thus are a reference for the performance of these materials [143]. They can be determined, using Equation 5, by fitting experimental data on the relationship between the incident light and the cure depth. The calculation of such parameters provides information for determining printing conditions as exposure energy, which should provide a cure depth larger than the layer thickness to ensure proper adhesion between the layers [25,78,128,139]. Therefore, delamination is avoided [3,78,143] and parts with good mechanical properties can be generated [3]. On the other hand, excessive energy exposure leads to over-polymerization and a decrease in the process accuracy [3,78]. Thus, a cure depth between 1.10 and 1.35 times the layer thickness is indicated [3].

2.6.3.1 Photoinitiators

An appropriate photoinitiator must be selected to initiate the photopolymerization reactions, considering mainly its compatibility with the adopted monomers and the relationship between its light absorption spectrum and the wavelength emitted by the light source [31,32,43].

Table 8 presents the photoinitiator already used in research related to ceramic VP.

Abbreviation	Name	Type	Longest absorbed wavelength (nm)	Related articles
BP	Benzophenone (diphenylmethanone)	2	330 [217]	[158]
CQ	Camphorquinone	2	> 468 [217]	[33,98]
DMPA (Irgacure 651)	2,2- dimethoxy-2- phenylacetophenone	1	370 [217]	[62,140]
HCPK (Irgacure 184)	1-Hydroxycyclohexyl phenyl ketone	1	380 [218]	[36,64,65,129,133,140,159 ,180,190]
HMPP (Irgacure 1173)	2-hydroxy-2-methyl-1- phenyl-propan-1-one	1	330 [217]	[66,78]

BAPO (Irgacure 819)	phenylbis(2,4,6-trimethylbenzoyl)phosphine oxide	1	465 [219]	[15,27,35,134,140,194]
TPO	Diphenyl(2, 4, 6-trimethylbenzoyl) phosphine oxide	1	415 [219]	[8,14,188,189,196,23,28,30,128,130,143,146,151]
TPO-L	ethyl (2,4,6-trimethylbenzoyl) phenylphosphinate	1	420 [217]	[25]

Source: Elaborated by the author.

Photoinitiators can be divided into two groups: free radical and cationic. Photoinitiators used in research related to ceramic vat photopolymerization (Table 8) are based on free radical chemistry. These photoinitiators produce radicals from the energy of a light source, being common for applications where acrylates are used. Besides, the free radical initiators can be divided according to the mechanism of free radical generation [217]. The Type I photoinitiators are single molecules that cleave into radicals when exposed to light of a compatible wavelength. The selection of a photoinitiator of this type strongly depends on the light source. Most of these initiators are not indicated for visible light, except the BAPO, which has a considerable absorption range in visible light. In turn, the Type II photoinitiators must be associated with a co-initiator (such as tertiary amines) to generate the free radicals [220], which makes them more complex and less efficient than Type I photoinitiators [221].

2.7 Post-Processing

As previously presented, ceramic vat photopolymerization is a multi-step process, and thus the green 3D printed body requires subsequent post-processing to eliminate the organics (debinding) and to increase density (sintering) [10,20,21]. Post-processing is critical to successfully obtaining ceramic parts. The debinding must have adequate heating rates to avoid cracks [25,33]. Furthermore, the sintering temperature has a strong influence on the properties of the ceramic components [4,34–37].

Ceramic vat photopolymerization is not indicated to produce large dense parts due to the high amount of organic material associated with the process and that would lead to cracks in the debinding of thick sections [11,79]. Suppliers specify 10 mm as the maximum wall thickness to be produced [45,79,222]. In fact, debinding is a very challenging process for

ceramic parts manufactured by vat photopolymerization since, in general, the slurries have more than 50 vol% of organic material [44].

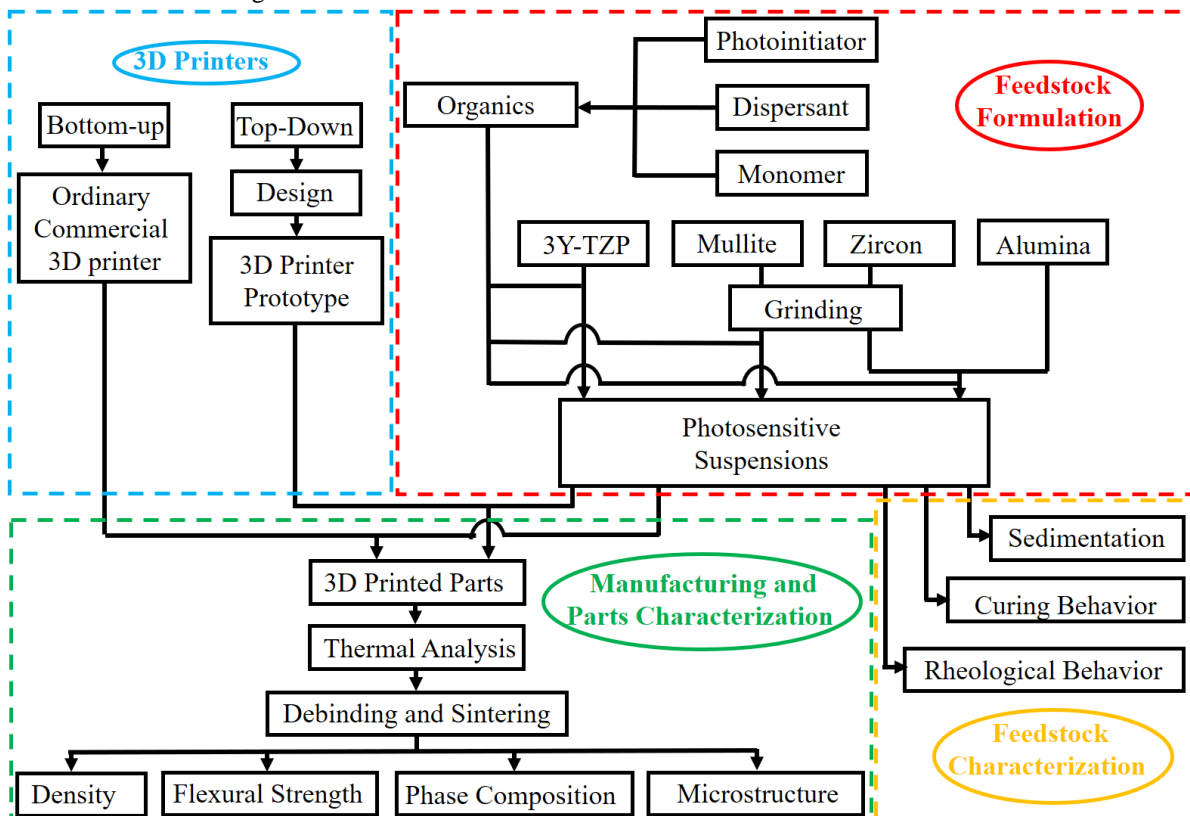
Thermal analysis is an important tool to define the post-processing protocol. Thermogravimetric analysis (TGA) is widely used to study the thermal decomposition of the ceramic green parts produced by vat photopolymerization [33,39,146,193,195]. This technique measures changes in mass with temperature using a thermobalance [223]. In this way, it is possible to observe the temperature range in which the decomposition of organic materials occurs, as well as to determine temperatures at which the decomposition is high. Such information must be considered to define the heating rates and possible holding times used during debinding.

In addition to atmospheric air, different atmospheres can be used as vacuum [37,106,181], nitrogen [64,76,92,151,158,224,225], and argon [226–230]. Such atmospheres avoid oxidation (exothermic decomposition) [106,158,231] promoting decreased volatilization/pyrolysis rate of organics, which may reduce deformation in this step [230]. However, the residual carbon in the debound body would produce gas during the following sintering process, which may lead to cracks [178]. Thus, a two-step debinding has been used [150,176–179,191,192,232], in which a first debinding step under vacuum decomposes the organic material at a controlled rate, and subsequently the debinding step under atmosphere air guarantee complete removal of the residual carbon [176,192].

3 MATERIALS AND METHODS

In this work, to test the formulated hypothesis, two 3D printers were used. For that, a top-down DLP 3D Printer for ceramic materials was designed, and a prototype was built, while an ordinary bottom-up commercial 3D printer (not specialized in ceramic materials) was selected. The ceramic powders were selected to evaluate distinct groups of ceramics: nanometric powders (3Y-TZP) and submicrometric powders (electrofused mullite). In addition, a combination of a natural raw material (zircon) with alumina was used to investigate in situ formation of mullite-zirconia composites in 3D printed parts. After evaluating the emission spectrum of the 3D printers, the organic materials were selected, and the photosensitive slurries were developed. Ceramic green bodies with complex geometries and specimens were 3D printed, debound, sintered, and characterized. The materials and methods employed are described next, and a schematic is shown in Figure 27. This thesis has already led to the publication of articles, and in this way, part of the specified methods has been published in journals [43,44,47], conference proceedings [41,42,233], and a book chapter [40].

Figure 27 – Schematic of the materials and methods used in this thesis.



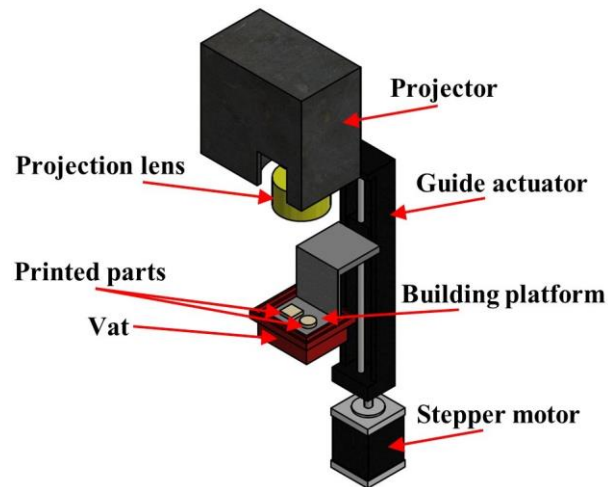
Source: Elaborated by the author.

3.1 DLP 3D Printer prototype

In this work, the design development of a top-down DLP 3D printer for ceramic materials was based on the design methodology structure proposed by Ulrich and Eppinger [234] and Pahl et al. [235]. First, the planning and task clarification considered the previous prototype of our research group [39] and the opinions of potential users (professionals related to the manufacture of advanced ceramics) to define the design requirements [42]. Some of these requirements are contradictions (when improving one technical requirement tends to worsen the other). Applying TRIZ, the emerged contradictions were converted into a pair of engineering parameters that had some possible principles of inventions indicated by Altshuller's Table of Contradiction [236,237]. Such principles were subsequently taken into consideration in the search for possible solutions, which take place in the next design phase (conceptual design). After defining the solution principle (concept), a preliminary design was proposed, and a prototype was built. The detailed design, which encompasses documentation and preparation for production, is beyond the scope of this work.

Some basic components (Figure 28) employed in the new version of the top-down DLP 3D printer prototype were reused from the previous version [38]. Thus, a commercial slide projector (X2, InFocus) which contains a mercury-vapor lamp and whose UV filter was removed was used as a light source. A projection lens was placed between the projector and the building platform to provide an image of the size of the building area. To move the building platform, it was employed a linear guide actuator (KR33A, THK) driven by a stepper motor with a torque of 1 N.m (NEMA 23). In addition, the control system of the previous prototype was maintained: a CPU (central processing unit) with Creation Workshop Software was used to process the STL files, create light projections, and control the movement of the platform and the recoating system with an Arduino Mega 2560 and a stepper driver TB6560 [38]. Designing an economical and compact recoating system (not shown in Figure 28) able to handle high viscosity photopolymerizable materials was the major challenge.

Figure 28 –Schematic diagram of a top-down DLP test bench.



Source: Adapted from an article resulting from this thesis [40].

3.2 Light source irradiance

As specified in the previous section (3.1), the light source employed in this project was a commercial projector with a mercury vapor lamp that had its UV filter removed. The emission spectrum of this lamp was obtained using a Fiber Optic UV-Vis Spectrometer (USB4000, Ocean Optics) which was positioned in the 3D printer where the formation of layers occurs, to guide the photoinitiator selection and calculate the useful irradiance.

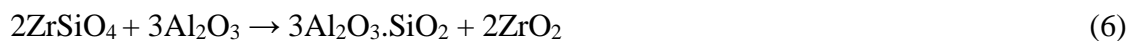
3.3 Ceramic Powders

The ceramic powders were selected to evaluate distinct groups of advanced ceramics: nanometric powders, submicrometric powders, and a combination of a natural raw material with a calcined powder. The selection of powders targeted materials with diverse applications. In addition, the materials chosen either aimed at evolution to the works of our research group or the application of materials still unexplored by the vat photopolymerization.

Partially stabilized zirconia is a high-performance ceramic material with desirable flexural strength, toughness, thermal insulation, and biocompatibility, which make it suitable for applications in several areas such as aerospace, automotive, biomedical, and dental [56,199]. Thus, yttria-stabilized tetragonal zirconia polycrystalline ceramic was selected as the nanometric powder. The commercial 3Y-TZP that had been employed in preliminary studies [38,39] of our research group was used, aiming to overcome the limitations presented so far (limited ceramic loading, high viscosity, poor stability, and short shelf life).

Mullite is an important refractory material, being suitable for several applications due to its high-temperature stability (melting point greater than 1800 °C), great thermal shock related to its low thermal expansion coefficient ($4\text{-}6 \times 10^{-6}/^{\circ}\text{C}$), outstanding high-temperature properties (which are superior to other advanced ceramics as zirconia and alumina), and strong heat and electrical insulation [238,239]. Also, electrofused mullite is an economical and viable raw material to produce refractory products [238]. However, its use as a raw material in AM has still been little explored and has never been reported in the DLP process [44]. Therefore, electrofused mullite powder was selected as the submicrometric powder.

Furthermore, mullite-zirconia composites are important refractory materials with desirable fracture toughness and strength [240], being suitable for high-temperature applications as power generation engines, combustors, and in the glass melting and steel industry [240,241]. Reaction sintering is widely used to obtain mullite-zirconia composites. Such a route is easily scaled up industrially with conventional ceramic equipment [242,243] and it has the advantage of being able to use readily available materials such as natural minerals as raw materials [240,242]. Alumina and zircon (ZrSiO_4) are extensively used as initial powders for being inexpensive raw materials [243]. The molar ratio 3:2 (alumina:zircon) is commonly used [240,244–247] for being the stoichiometric proportion for the formation of zirconia and mullite, as described in Equation 6 [245,248–250]. This reaction starts above 1400 °C [251] and 1600 °C may be required to complete it [240,245]. Although its manufacturing has been extensively studied by conventional processes, to the best of our knowledge, the additive manufacturing of mullite-zirconia parts has never been reported before the works related to this thesis. Hence, zircon and alumina were selected to investigate in situ formation of mullite-zirconia composites.



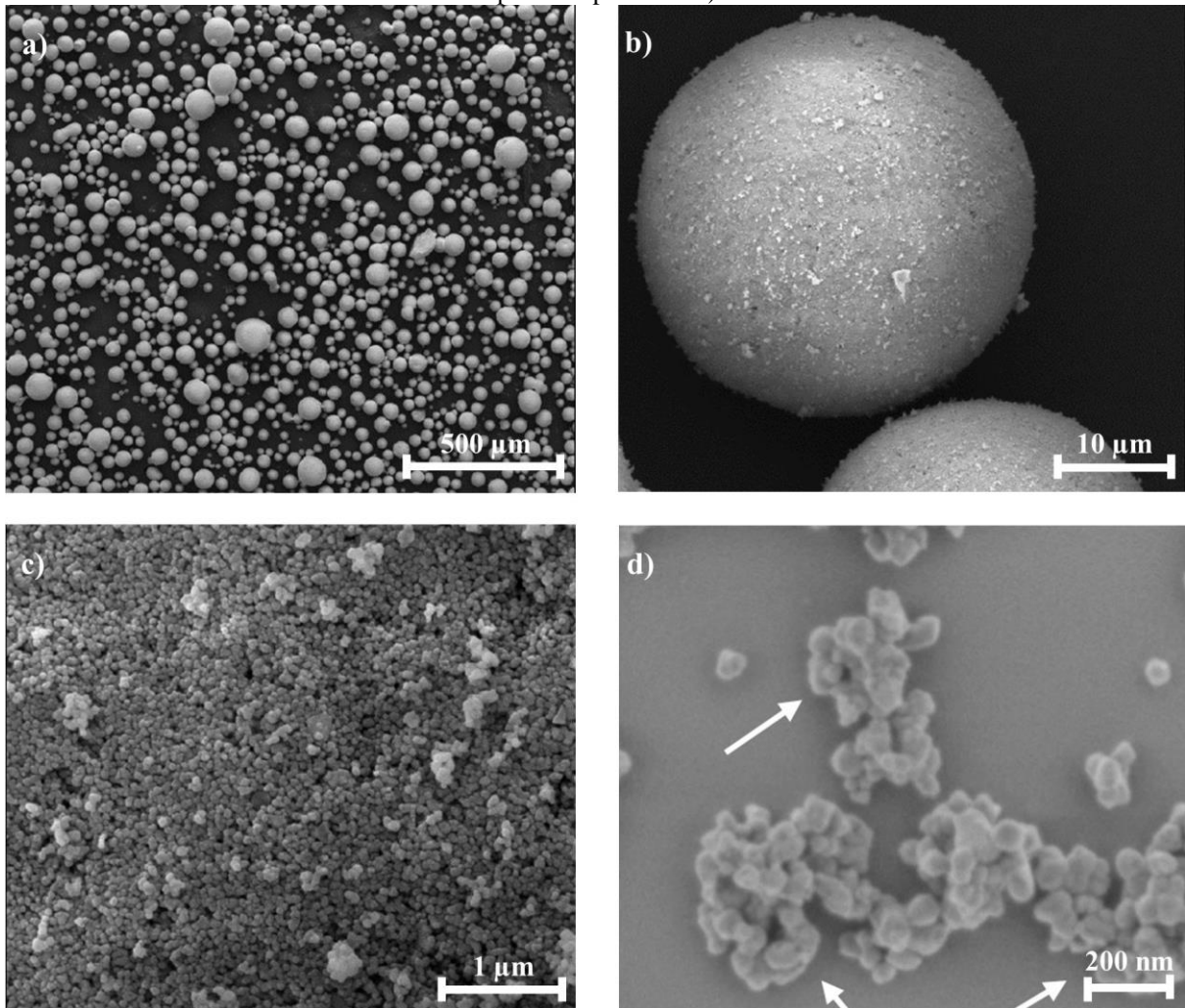
Thus, three sets of suspensions were developed, based on the following powders:

- Partially stabilized zirconia (3Y-TZP) powder (TZ-3Y-E, Tosoh Corporation, Japan) was used as received.
- Commercial electrofused mullite powder (MUB, Elfusa, Brazil) with particle size between 0.2 and 0.5 mm (35/70 MESH) was ground.
- Commercial zircon powder (325 MESH, Minasolo, Brazil) was ground and used with as-received calcined alumina powder (A1000 SG, Almatiss, USA).

3.3.1 Ceramic Powders preparation

According to the manufacturer's datasheet [252], the 3Y-TZP powder presents a particle size of $0.04\ \mu\text{m}$ and a specific surface area of $16 \pm 3\ \text{m}^2/\text{g}$. On the other hand, it is supplied as spray-dried granules ($D_{50}=60\ \mu\text{m}$) to ensure flowability and avoid agglomeration during storage [253], as shown in Figure 29. Although the powder particles are already small enough for the process and will be added to the suspension as received, a proper slurry preparation is required to break up agglomerates and homogenize the suspension, which will be discussed in the next section.

Figure 29 – SEM images of the 3Y-TZP powder (TZ-3Y-E). a) Granules. b) Magnified granule. c) Granule surface composed of particles. d) Particles.



Source: Adapted from [254,255].

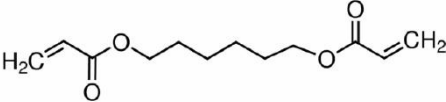
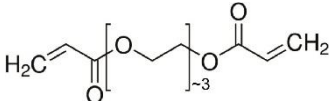
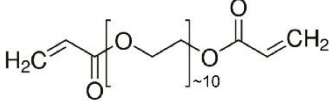
On the other hand, the mullite and zircon powders are coarse and need processing, aiming for a powder suitable for DLP suspensions. The grinding of the mullite and zircon powders was performed as described next. Jars with an internal volume of 300 ml ($\varnothing 70$ mm x h80mm) were filled with 500 grams of zirconia balls ($\varnothing 10$ mm), 70 ml of distilled water, and 30 ml of the powder to be processed. Also, ammonium polyacrylate (1 wt% of the mass of the powder) and ethylene glycol (0.8 wt% of the mass of the powder) were added as grinding additives. Then, the powder was wet ground in a ball mill for 7 days and subsequently in a vibrating ball mill also for 7 days. Subsequently, the powder was dried in the oven for 12 h at 100 °C. The powder was then submitted to manual action in the mortar and pestle and sieved (ASTM 50). The weight of the grinding media (zirconia balls) was measured before and after the described grinding protocol, to check their wear. The ground material was analyzed on an X-ray fluorescence spectrometer (EDX 720HS, Shimadzu) under a vacuum atmosphere with a 5 mm collimator aperture to check the presence of zirconia from the grinding media. Also, the phase composition of this material was identified by X-ray diffraction (XDR-7000, Shimadzu).

Besides, the particle size and specific surface area of the ground powder were measured by X-ray monitored gravity sedimentation principle (Sedigraph III Plus, Micromeritics) and BET method (FlowSorb II 2300, Micromeritics), respectively. Lastly, the density was measured by a Helium Gas Pycnometer (Accupyc 1330, Micromeritics).

3.4 Slurry development

In addition to the ceramic powder, the slurries were composed of monomer, dispersant, and a photoinitiator. Thereby, 1,6-Hexanediol diacrylate (HDDA, Sigma Aldrich, USA) and two different Poly(ethylene glycol) diacrylate molecules with different average molecular weights (PEGDA 250 and PEGDA 575, Sigma Aldrich, USA) were used as monomers. The characteristics of the resins used are shown in Table 9, whose viscosity was measured using a rotational viscometer (DV2T extra, Brookfield, Canada) between 23 and 25 °C. Phenylbis(2,4,6-trimethylbenzoyl)phosphine oxide (BAPO, Sigma Aldrich, USA). Six commercially available dispersants were tested: DISPERBYK-111, BYK-W-969, DISPERBYK-2001, DISPERBYK-2155, DISPERBYK-2158 (BYK-Chemie, Germany), and Triton X-100 (Sigma Aldrich, USA).

Table 9 – Monomers used in this thesis.

Monomer	Molecular Structure	Density (g/cm ³)	Viscosity (mPa.s)
1,6-Hexanediol diacrylate (HDDA)		1.01	8
Poly (ethylene glycol) diacrylate with average M _n 250 (PEGDA 250)		1.11	15
Poly (ethylene glycol) diacrylate with average M _n 575 (PEGDA 575)		1.12	48

Source: Adapted from an article resulting from this thesis [43].

The slurry preparation started with the mixing of the resin with the dispersant, followed by the gradual addition of the ceramic powder and photoinitiator (2 wt% of the resin). Then, the suspension was ball-milled with zirconia balls for 24 hours to break up agglomerates and homogenize the suspension.

3.5 Rheological Behavior

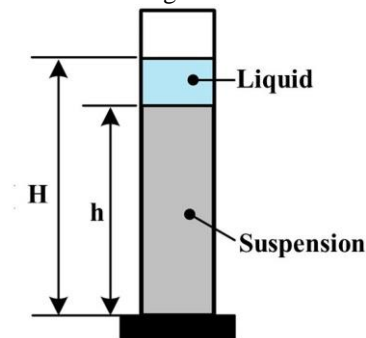
The rheological behavior of the ceramic slurries was characterized using a rotational viscometer (DV2T extra, Brookfield, Canada) between 23 and 25 °C. In the flow curves, the rheological parameters were adjusted according to the Herschel-Bulkley model (Equation 2, subsection 2.6.1.2). Also, the Krieger-Dougherty model (Equation 4, subsection 2.6.2.1) was used to estimate the relationship between viscosity and solid loading.

3.6 Stability

Each suspension's stability was investigated by sedimentation tests, as previously done by some related works [28,30,128,130,143,170]. Thus, 10 ml of each suspension was poured

into graded tubes. The measuring tubes were kept undisturbed for 30 days and the retained suspension volume fraction was recorded as a function of time.

Figure 30 – Schematic diagram of the sedimentation test



$$\text{The retained suspension} = \frac{h}{H} * 100\%$$

Source: Adapted from [64].

3.7 Curing and photosensitive parameters

Photosensitive parameters (penetration depth D_p and critical exposure energy E_c) were determined by the relationship between curing thickness and exposure energy to the light source. For this purpose, the photopolymerizable suspensions were poured into a petri dish and positioned in the DLP built 3D printer. The slurries were cured with different exposure times. The layers were rinsed with isopropyl alcohol (IPA) and their thickness was measured using a caliper, like what is described in the literature [139,143] and the photosensitive parameters were determined by fitting the experimental data to the Beer-Lambert Law (Equation 5, subsection 2.6.3).

3.8 Thermal analysis

To avoid cracks, adequate heating rates are necessary during the debinding [25,33]. Hence, the thermal decomposition of the ceramic green parts was analyzed by thermogravimetric analysis (SDT Q600, TA Instruments). A piece of the printed part was heated (10 °C/min) from room temperature to 1000 °C in air (50 mL/min). Other atmospheres have not been tested, as post-processing under different atmospheres would require a special furnace, not available for this work.

3.9 Additive manufacturing and post-processing

Both the built prototype and the commercial DLP 3D printer were used to manufacture green ceramic parts. The prototype uses the top-down approach with a dedicated recoating system. Details about the built prototype and its innovative recoating system are discussed in 4.1. It showed better printability for 100 μm layer thickness, which was selected for all tests on this equipment.

On the other hand, the selected commercial DLP 3D printer (LD-002H, Creality) uses the bottom-up approach with a monochrome LCD screen as the light source. In this case, 50 μm layer thickness was selected, as this is the standard specification for this equipment.

The printed parts were then rinsed with isopropyl alcohol (IPA) and dried in the oven for 12 h at 100 $^{\circ}\text{C}$. Finally, the samples were debound and sintered in an air environment in a box furnace (Blue M, Lindberg). The debinding protocol was defined based on the thermal decomposition, and it is presented in Table 11 (subsection 4.2.7). All samples were sintered with a two-hour hold in the maximum temperature, which varied between samples and will be specified in the results. Besides, some specimens sintered at 1500 $^{\circ}\text{C}$ were subject to a subsequent sintering step at 1650 $^{\circ}\text{C}$ for 2 hours in a gas furnace.

3.10 Sintered parts characterization

The linear shrinkage was determined using a digital caliper. The density of the sintered parts was measured based on Archimedes' Principle using an analytical balance with a resolution of 0.01 mg (AUW220D, Shimadzu) according to ASTM-C20. A Helium Gas Pycnometer (Accupyc 1330, Micromeritics) was used to measure the apparent density of the sintered parts, which was used to calculate the relative density.

Flexural three-point strength tests were performed on sintered 3D printed bars with no additional machining or surface polishing (25 mm x 2 mm x 1.5 mm), according to standard ASTM C1161. For this test, a universal testing machine (Bionix 370.02, MTS®) was used with a load cell of 15 kN, a span of 20 mm, and a crosshead speed of 0.2 mm/min.

The phase composition of the raw material and powder from parts sintered at different temperatures were identified by X-ray diffraction (XDR-7000, Shimadzu). Lastly, SEM samples were analyzed by scanning electron microscopes (SIGMA, WEISS and JSM7500F, Jeol). For this purpose, the samples were polished and thermally etched for 6 minutes at temperatures that depend on the sintering temperature, as defined by Equation 6, where T_{etch}

is the etching temperature (in °C), and T_{sint} is the sintering temperature (in °C). This procedure was empirically developed by our research group and published in an article resulting from this thesis [47].

$$T_{etch} = T_{sint} * 0.875 + 100 \quad (6)$$

4 RESULTS AND DISCUSSIONS

This section presents and discusses the results on four main topics:

- i) The design development of a DLP 3D Printer Prototype for ceramic materials
- ii) Photosensitive slurries based on as-received commercial nanometric ceramic powders: development, characterization, and use to produce ceramic parts in the built prototype.
- iii) Photosensitive slurries based on processed submicrometric ceramic powders: coarse ceramic powder grinding, slurry preparation and characterization, and used not only in the built prototype but also in an ordinary commercial 3D printer (not specialized in ceramic materials).
- iv) Additive manufacturing based on a mixture of a natural raw material (zircon) with alumina combined with reaction sintering to create in situ mullite zirconia composites parts.

4.1 DLP 3D Printer Prototype for ceramic materials: design development

Parts of this subsection have been published as a book chapter [40] and a conference paper [42]. Besides, a patent for the invented recoating system has been filed [256].

In the preliminary studies on ceramic additive manufacturing by DLP carried out by our research group, a built test bench was used, and the layers were manually spread, as shown in Figure 31. A recoating system based on a single blade was tested, however, it was not able to create uniform layers of the viscous ceramic slurries [39]. In this way, manufacturing was highly dependent on the operator and had low repeatability. Thus, in this work, the development of a new DLP 3D printer prototype capable of producing ceramics was proposed to overcome these obstacles.

Figure 31 – Manual spread of layers performed by previous works of our research group.



Source: Adapted from a previous dissertation by our research group [38].

Moreover, developing a low-cost machine, capable of handling different raw materials with high printing speed and accuracy was defined as the design requirement. Some of these requirements present contradiction (when improving one requirement tends to worsen the other), and TRIZ was applied to point out some possible principle of inventions (Table 10), which were taken into consideration in the design of the recoating system.

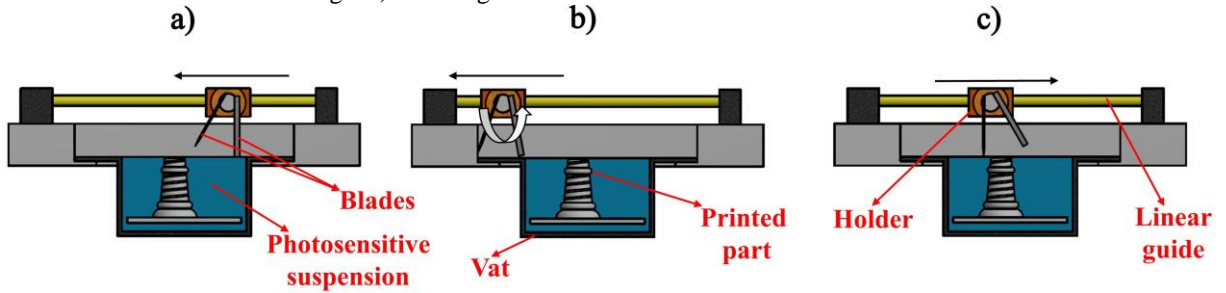
Table 10 – Application of TRIZ on requirements contradictions.

Contradiction	Conflicting Design Requirements	Engineering Parameters	Principles of invention
1	Price	Complexity	Dynamicity, Mechanical
	Number of raw materials	Adaptability	System, Pneumatic or hydraulic, Thermal expansion
2	Price	Complexity	Equipotentiality, Another
	Printing speed	Productivity	dimension, Mechanical system
3	Z Resolution	Accuracy of manufacturing	Preliminary Action, Mechanical
	Printing Speed	Productivity	Vibration, Color Changing, Inert atmosphere

Source: Adapted from an article resulting from this thesis [42].

A low-cost solution based on a two-blade system (instead of one, as usual) allows the use of the device for different materials, even those with high viscosity. The blades have sequential and distinct functions: the first blade spreads and the second blade levels and calibrates the thickness. Therefore, the two blades can have different shapes and materials. The position change that defines the active blade was based on some principle solutions indicated by TRIZ. Thus, the movement of blades for positioning occurs because of the intrinsic movement for layer formation, without wasting time for this specific action (“preliminary action”). For this, the blades and the holder can have relative movement to each other (“dynamicity”) and the blades can rotate in an additional dimension (“another dimension”). The concept is presented in Figure 32.

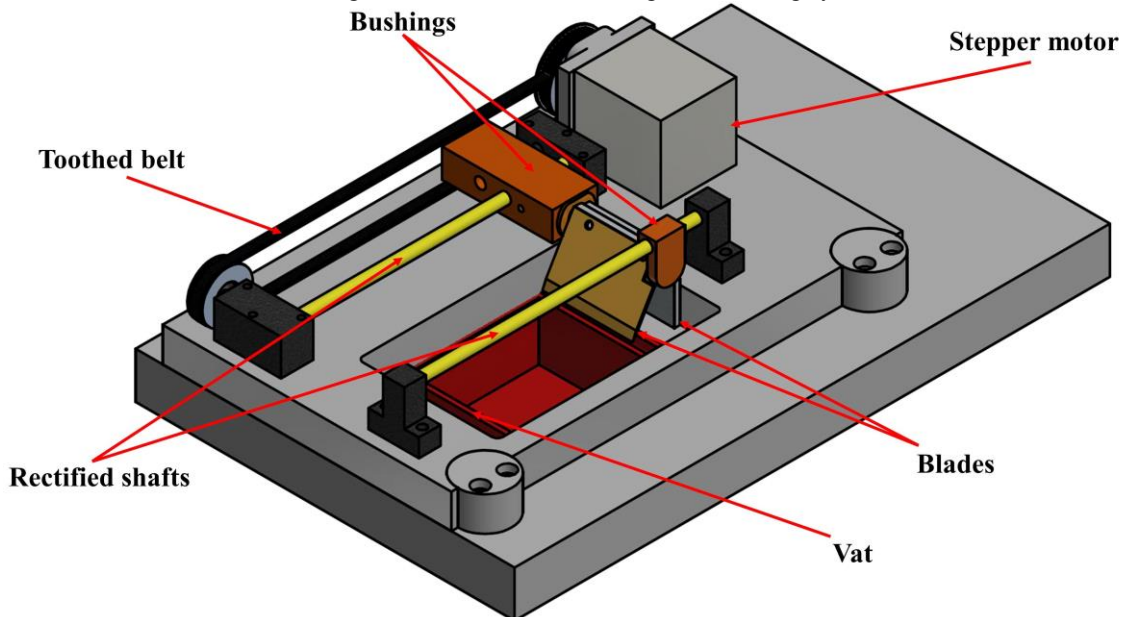
Figure 32 – Schematic diagram of the recoating system concept. a) Spreading with the first blade active. b) Active blade change. c) Leveling and thickness calibration with the second blade active.



Source: Adapted from an article resulting from this thesis [42].

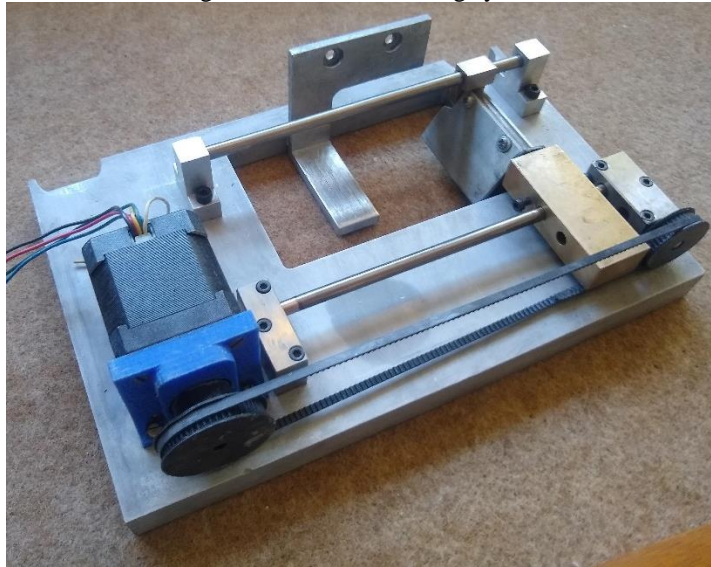
Figure 33 is a sketch of the designed recoating system. The linear forward and backward movement of the blade holder is created by rectified shafts and bushings, driven by a stepper motor with a torque of 0.5 N.m (Nema 17), and transmitted by pulleys and timing belts. Both blades (spreading and leveling) were made of aluminum with different thicknesses (1.5 and 3.0 mm). The built recoating system is shown in Figure 34.

Figure 33 – Sketch of the designed recoating system.



Source: Adapted from an article resulting from this thesis [40].

Figure 34 – Built recoating system



Source: Adapted from an article resulting from this thesis [40].

Figure 35 – 3D printer prototype built.



Source: Elaborated by the author.

Figure 35 shows the built prototype assembled in a manufactured stainless steel structure. In this work, the printing area was left open to facilitate monitoring. However, for future developments, it is indicated to use an enclosure for this area not only for better control of the ambient light and temperature [199] but also to reduce exposure to the 3D printing feedstock and their fumes which may cause irritation and/or allergy.

4.2 Additive Manufacturing of 3Y-TZP: slurry development and 3D printer prototype validation

Parts of this subsection have been published as a journal [43] and a conference paper [41].

The development of the ceramic suspensions had as a starting point the preliminary studies that had already been carried out by our research group [39]. Although these formulations were able to produce a few ceramic pieces, they had limitations related to rheological behavior, stability, and shelf life. Foremost, these suspensions would present high viscosity (~30 Pa.s) with a limited ceramic loading (<35 vol%). When preparing these formulations again, it was possible to notice that such formulations, based on the use of several solvents (N-methyl-2-pyrrolidone, xylene, isopropyl alcohol), changed over time and had to be used immediately after preparation. Within a few hours after preparation, considerable sedimentation could be observed, and a liquid phase separated at the top (Figure 36). After 24 hours of preparation, the slurry showed a significant loss in its ability to form layers (curing) and a significant increase in viscosity. The initial characteristics were not recovered even after repeating the preparation process, indicating that some reaction between the raw materials had occurred.

Thus, aiming to overcome the limitations of the previous formulations, solvent-free slurries were prepared using the same powder (TZ-3Y-E, Tosoh Corporation, Japan). Several dispersants and resins were tested, and a photosensitive suspension with suitable rheological behavior and stability was used to 3D print ceramic green parts in the DLP 3D printer prototype built. Conversely, the same suspension was not adequate in the commercial 3D printer. The samples manufactured in the prototype were debound and sintered, and the ceramic parts were characterized, as described next:

Figure 36 – Ceramic suspension based on preliminary studies of our research group, after 4 hours of preparation, presenting sedimentation and liquid phase separation (yellowish coloring) at the top.



Source: Elaborated by the author.

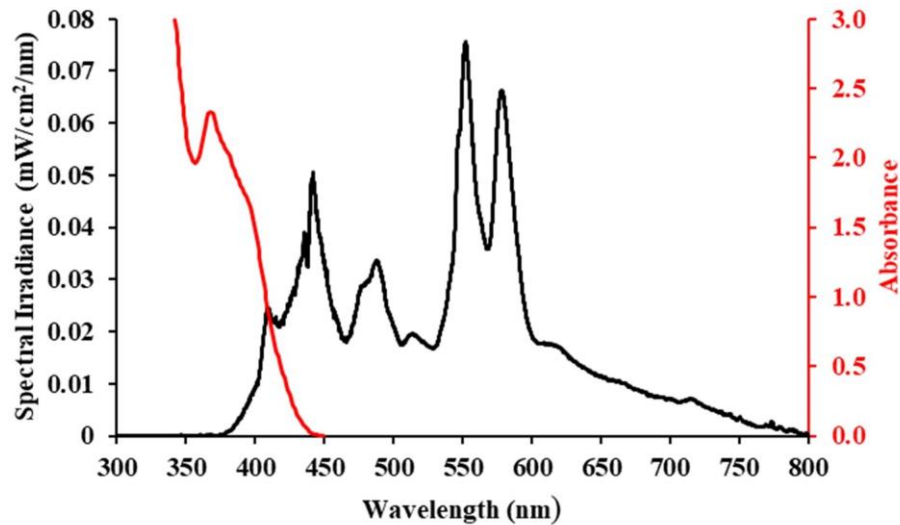
4.2.1 Choosing the photoinitiator and light source irradiance characterization.

Most related works use either laser (Hinczewski et al., 1998b; Li; Zhao, 2017; Sun et al., 2019) or monowaved led [25,33,146] centered at a specific wavelength that overlaps the absorption range of the initiator. Conversely, the built prototype uses a standard mercury vapor lamp from a commercial projector with most of the emission in visible light, which highlights the process of choosing the photoinitiator

A summary of the photoinitiators used in research related to ceramic VP was presented in Table 8 (subsection 2.6.3). Although CQ has a considerable absorption in visible light, it is a type 2 photoinitiator [217]. It would need a co-initiator as a tertiary amine [257], making the process more complex. Also, it is a relatively slow curing photoinitiator [217]. On the other hand, most photoinitiators are type I, and their application varies mainly with the absorption spectrum range. Among the most used photoinitiator for ceramic sensitive suspensions, HCPK does not respond and TPO has a small absorption in long wave UV. BAPO stands out for its effective absorption up to 420 nm [195,217,257], thus justifying its selection for use with the mentioned light source.

Figure 37 shows the absorbance graph of BAPO [217] and the measured emission spectrum of the mercury vapor lamp, which delivers approximately 7.9 mW/cm^2 with a broad emission spectrum (380-800 nm), of which just 0.5 mW/cm^2 is useful irradiance.

Figure 37 – Emission spectrum of the used mercury-vapor lamp and absorbance of the photoinitiator selected (BAPO).



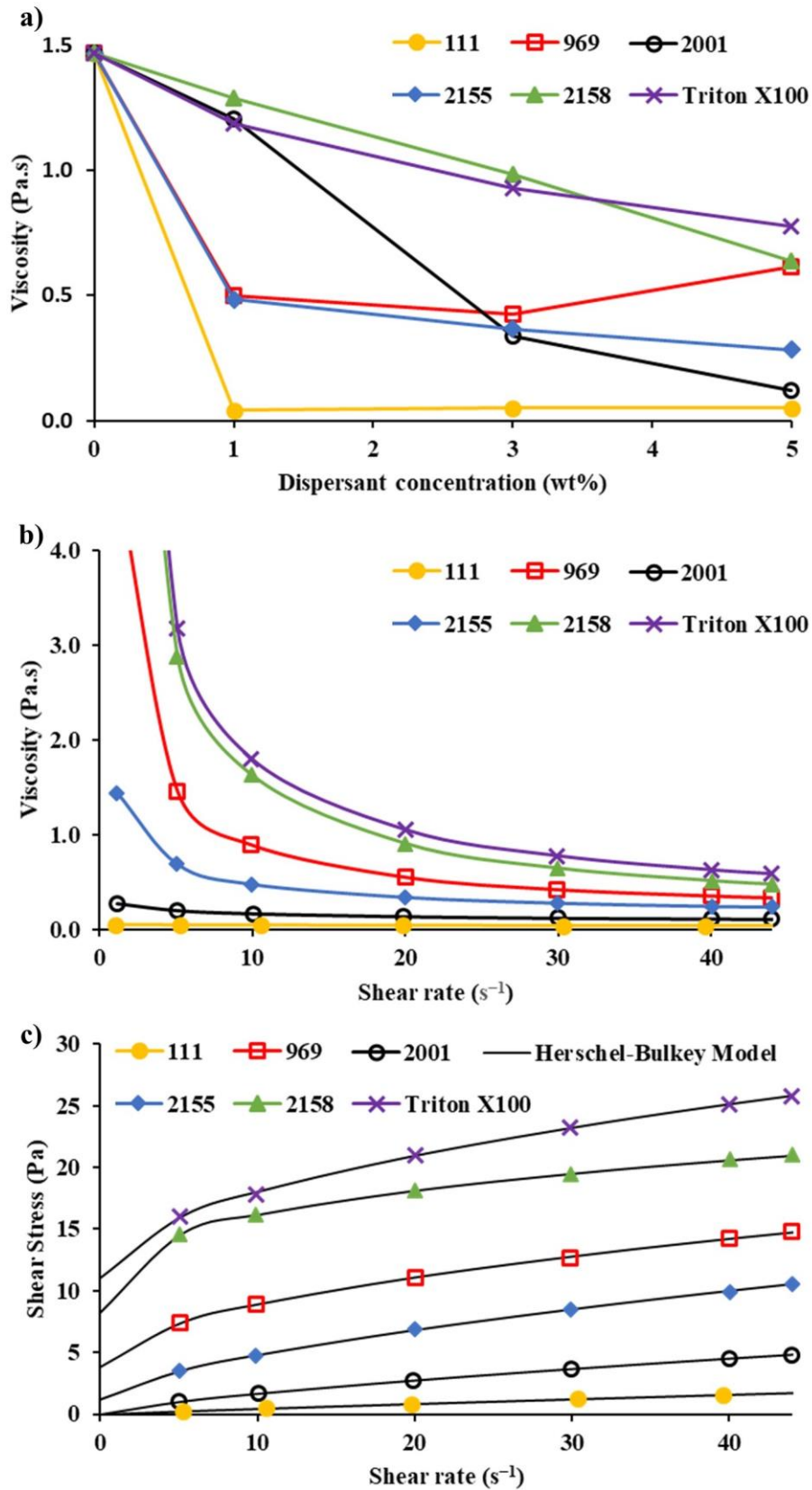
Source: Adapted from an article resulting from this thesis [41].

4.2.2 Choosing the dispersant

Choosing an appropriate dispersant is essential for developing ceramic suspensions with suitable stability and rheological behavior [28,131,143]. For this test, PEGDA 250 was chosen as the monomer, because even though it is a polyethylene glycol diacrylate, like the one used in the preliminary formulations (PEGDA 575), it has a considerably lower viscosity, as shown in (Table 9, page 79). Ceramic slurries with 15 vol% of ceramic loading were chosen to analyze the effects of dispersants on rheological behavior and stability. Although a higher percentage of ceramics is desired for the slurries used for DLP additive manufacturing (≥ 40 vol%), preliminary analyzes need to be performed at lower concentrations to find proper components, otherwise, most of the initial test suspensions would have high viscosity, outside the measurement range of the available viscometer, and could not be compared [43]. In addition, related works have performed sedimentation tests with ceramic loading below 20 vol%, because a higher solid loading would make it difficult to visualize sedimentation [106,128,130,131,140].

Figure 38a presents the viscosity with different dispersants with varying concentrations at a shear rate of 30 s^{-1} , showing that Disperbyk-111 had the lowest viscosity, even in a lower concentration. Moreover, Disperbyk-111 presented near-Newtonian behavior while all the other dispersants showed a shear-thinning behavior (decreased viscosity with an increase in shear rate), as shown in Figure 38b. In addition, Figure 38c shows the flow curve.

Figure 38 – Rheological behavior of 3Y-TZP ceramic slurries with 15 vol% solid loadings (a) with different dispersants with varying concentrations at a shear rate of 30 s^{-1} . (b) Viscosity curve with different dispersants in the concentration which provided the lowest viscosity. (c) Shear stress vs shear rate with different dispersants fitted by the Herschel-Bulkley model.

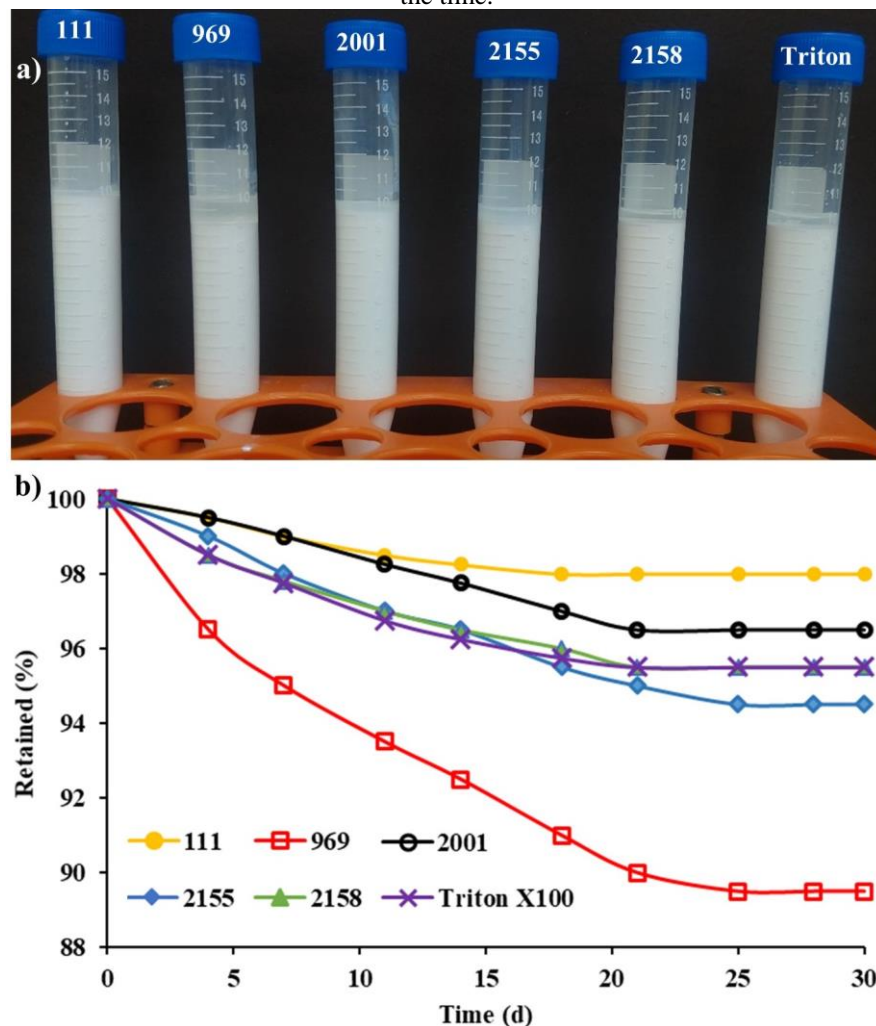


Source: Adapted from an article resulting from this thesis [43].

The rheological parameters were adjusted according to the Herschel-Bulkley model. The coefficient of determination (R^2) related to all the suspensions was higher than 0.999, indicating a good fit for the model. High yield stress is generally considered to be an obstacle to the spreading of new layers [26,130] and the yield stress tends to rise with increasing solid loading [28,130]. Therefore, Disperbyk-111 and Disperbyk-2001 have the advantage of having a negligible yield stress in 15 vol% suspensions. All the other dispersants had yield stress higher than 1.0 Pa, with Triton X-100 reaching the highest value (11.1 Pa).

The effects of dispersants on the stability of the ceramic suspensions are shown in Figure 39. A suspension with each dispersant was tested, picking the amount of dispersant that provided the lowest viscosity. The suspension with Disperbyk-111 had the best performance, with a retained volume fraction of 98 % after 30 days. For these reasons, Disperbyk-111 was chosen as the dispersant for the following tests.

Figure 39 – Sedimentation test of 3Y-TZP ceramic slurries with 15 vol% solid loading with different dispersants. (a) Suspensions with different dispersants after 30 days of settling. (b) Retained volume fraction as a function of the time.



Source: Adapted from an article resulting from this thesis [43].

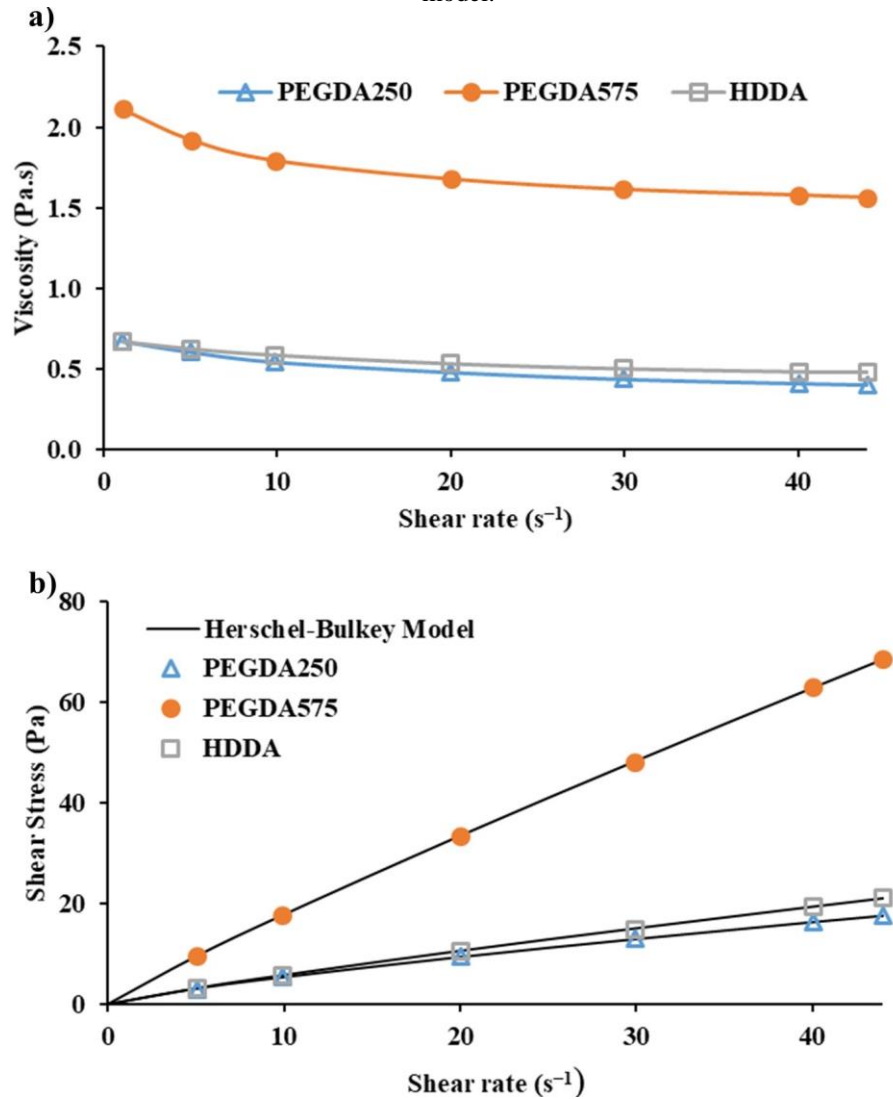
4.2.3 Choosing the resin

Once a proper dispersant was chosen, the solid loading could be increased for testing different resins. Ceramic slurries with 30 vol% of 3Y-TZP and 2 wt% of Disperbyk-111 were chosen to analyze the effects of using different resins on the rheological behavior of the suspensions. In this case, solutions with high concentration (e.g. 40 vol%) would still provide slurries with viscosity outside the viscometer's measurement range.

Figure 40a shows that the slurry using PEGDA 250 had the lowest viscosity (under 0.5 Pa.s at 30 s^{-1}) even though, on its own, this monomer has a considerably higher viscosity than HDDA (see Table 9 in section 3.4). These are two bifunctional monomers with similar molar mass; however, HDDA is hydrophobic and PEGDA 250 is hydrophilic with polar groups on the polymer chains, which makes it more compatible with ceramic particles with hydroxyl groups on their surfaces. Hydrophilic monomers lead to well-dispersed ceramic particles in suspensions [129]. Contrarily, nonpolar/hydrophobic monomers do not effectively disperse ceramic particles [129,130]. Hydrophobic monomers do not prevent agglomeration [131] and tend to provide higher viscosity dispersion [145]. Lastly, Figure 40b shows the flow curve with the Herschel-Bulkley model, which again proved to be a good fit ($R^2 > 0.999$) indicating the absence of yield stress for all slurries analyzed.

Moreover, HDDA presented a poorly curing behavior. While the two polyethylene glycol diacrylate formed layers thicker than $100 \mu\text{m}$ for 20-second light exposure, HDDA did not form layers even for light exposure of 100 seconds. Thus, PEGDA 250 was chosen as the monomer for the following tests due to its proper rheological and curing behavior.

Figure 40 – Rheological behavior of 3Y-TZP ceramic slurries with 30 vol% solid loading (a) viscosity curve with different monomers (b) Shear stress vs shear rate with different monomers fitted by the Herschel-Bulkley model.

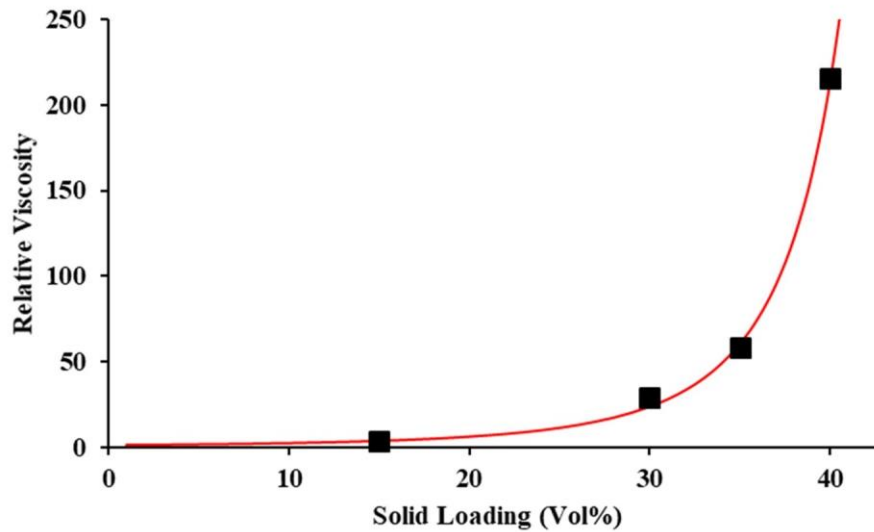


Source: Adapted from an article resulting from this thesis [43].

4.2.4 Influence of solid loading on the viscosity

Next, ceramic slurries with PEGDA 250 as the monomer and 2 wt% of Disperbyk-111 were chosen to analyze the effects of solid loading on the viscosity of the suspension. Figure 41 shows the viscosity at a shear rate of 30 s⁻¹ for suspensions with different ceramic volume fractions. The Krieger-Dougherty model was used to estimate the maximum solid fraction. The maximum solid volume fraction found $\phi_m = 52.2\%$, providing a satisfactory fit ($R^2 \cong 0.999$). As ϕ approaches ϕ_m , any increase in the solid volume fraction of the suspension represents a large increase in viscosity. Furthermore, the suspension with 40 vol% of solid loading presented a viscosity of 3.3 Pa at a shear rate of 30 s⁻¹.

Figure 41 – Influence of solid loading in 3Y-TZP ceramic slurries with 2wt% of Disperbyk-111 at a shear rate of 30 s^{-1} .



Source: Adapted from an article resulting from this thesis [43].

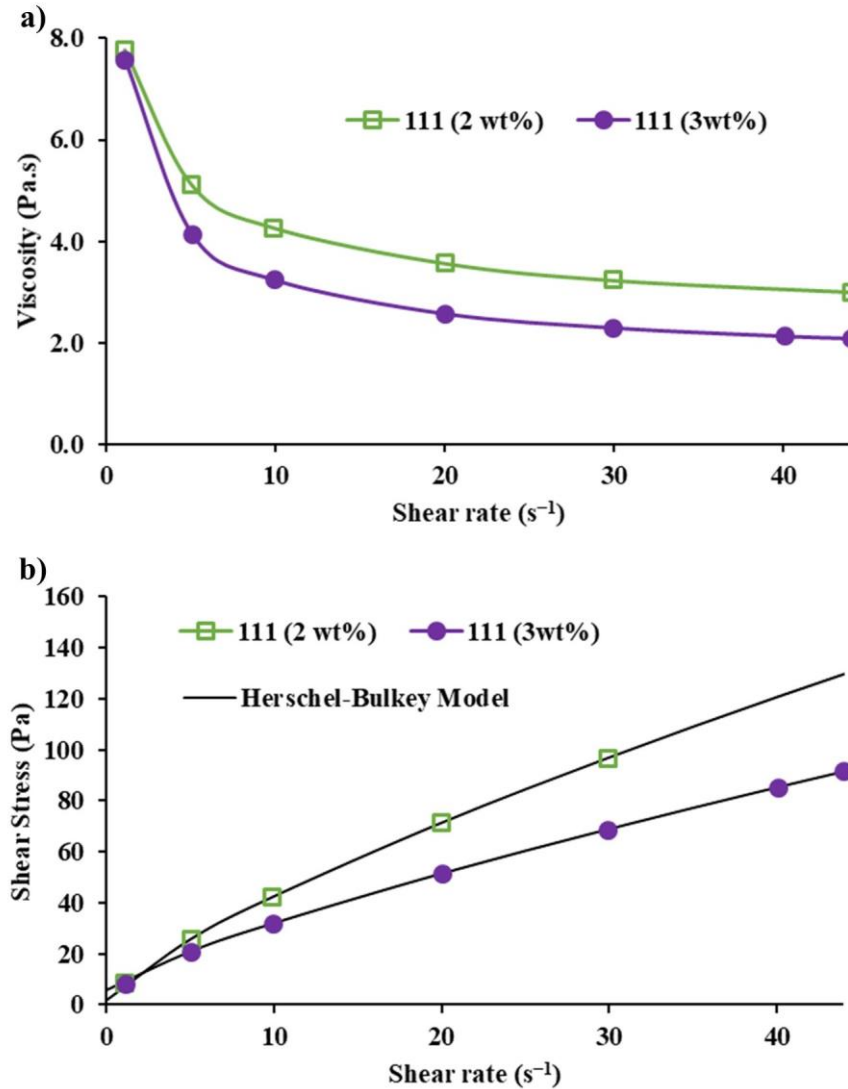
4.2.5 Choosing the dispersant concentration

The highest possible solid loading that provides adequate viscosity to the process is desired. However, 40 vol% exceeded 3 Pa.s, which is the viscosity limit [9,26,37] respected by most related works, as discussed in Section 2.6. Even though a concentration test has already been presented for Disperbyk-111 with suspensions of 15 vol% (subsection 4.2.2), in that case, the viscosities were very low, and no significant differences could be observed. Therefore, a new test was performed for suspensions with higher solid loading, looking for a suspension with a viscosity suitable for the process.

Ceramic slurries with 40 vol% of 3Y-TZP and PEGDA 250 as the monomer were chosen to analyze the effects of the concentration of Disperbyk-111 on viscosity, as shown in Figure 42a. The suspension with 1 wt% of Disperbyk-111 was very viscous and could not be measured because it was outside the measuring range of the rotational viscometer. An increase in the concentration of Disperbyk-111 caused a decrease in viscosity, and 3 wt% of this dispersant provided a 40 vol% ceramic slurry viscosity suitable for the DLP additive manufacturing ($2.3 \text{ Pa}\cdot\text{s}$ at 30 s^{-1}). The shear-thinning behavior presented by these suspensions is characteristic of VP ceramic slurries [3,9,36,65,129,140,146,150,170]. Such behavior is desirable in VP [25,141,147] because it avoids sedimentation of the suspension in a stationary state, and adequate flow when a shear rate is applied to the slurry [78]. Figure 42b shows the shear stress–shear rate curves. According to the Herschel-Bulkley model, the suspension with

Disperbyk-111 presented a yield stress of 5.9 Pa ($R^2 > 0.9999$). Such a moderate value of this property has been considered desirable to avoid spontaneous flows [163].

Figure 42 – Rheological behavior of 40 vol% solid loading 3Y-TZP ceramic slurries with different dispersant concentrations. (a) Viscosity curve; (b) Shear stress vs shear rate fitted by the Herschel-Bulkley model.



Source: Adapted from an article resulting from this thesis [43].

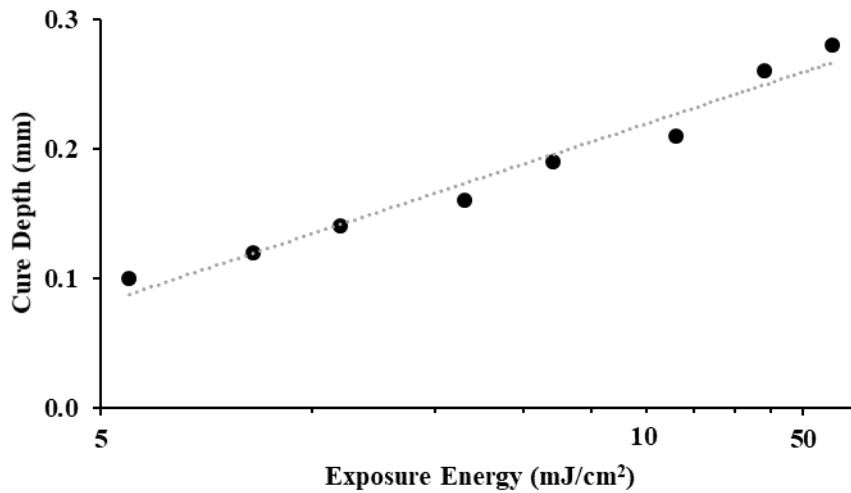
Moreover, all the sedimentation tests with a solid loading of 40 vol% (using BYK-111 as the dispersant) presented no noticeable sedimentation, indicating well-dispersed slurries with stability suitable for DLP additive manufacturing.

4.2.6 Photosensitive parameters

Figure 43 shows the relation between the cure depth and exposure energy. The critical energy found (1.78 mJ/cm^2) is comparable with the lowest values obtained in the literature for

photosensitive ceramic suspensions [143,146]. As presented in section 2.6.3, the cure depth should be from 1.10 to 1.35 of the layer thickness to ensure layer integration without impairing the accuracy. Thus, for the AM of ceramic parts with 100 μm layer thickness, the exposure time was set to 10 mJ/cm^2 .

Figure 43 – Cure depth vs exposure energy of the 3Y-TZP photosensitive ceramic suspension.

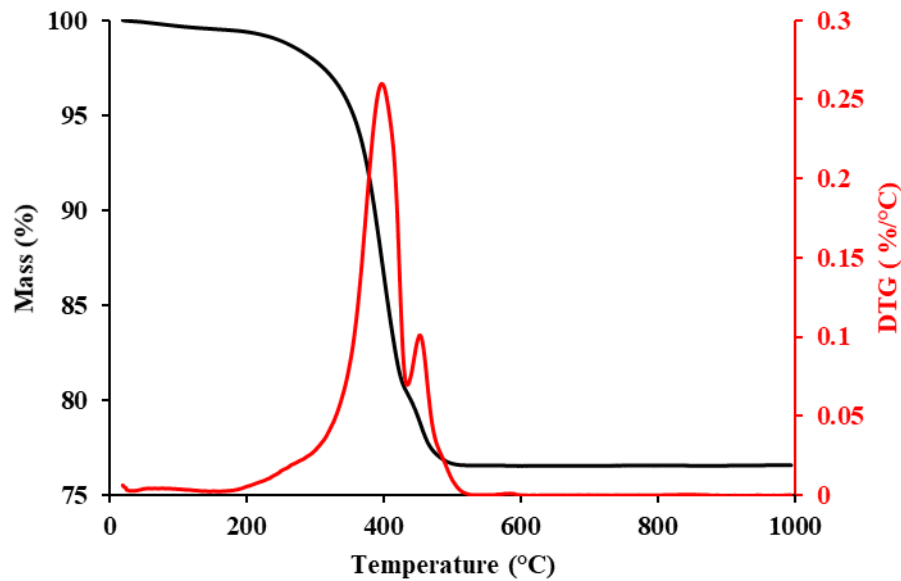


Source: Adapted from an article resulting from this thesis [41].

4.2.7 Thermal analysis

The thermogravimetric analysis is shown in Figure 44. The total weight loss was 23.4% and no mass change was recorded after 600 °C. Decomposition rates are higher between 350 and 470 °C (18.0% of weight loss) with a maximum peak at 400 °C. Using the thermal analysis, the debinding and sintering program was defined. The heating rate was reduced for higher decomposition rates and a hold point was introduced at the maximum peak temperature and other at 600 °C to ensure that all the organics were removed before the heating rate increased. Therefore, the parts were debound and sintered following the protocol (Figure 44): 1 °C/min from room temperature to 350 °C, 0.5 °C/min up to 600 °C with plateaus of 1 h at 400 °C and 600 °C, 5 °C/min up to 900 °C and 6 °C/min up to the sintering temperature (T_{sint}) and held for 2 hours. Different sintering temperatures (1400, 1500, and 1600 °C) were evaluated in this work.

Figure 44 – Thermogravimetric analysis of the 3Y-TZP green printed parts. b) Post-processing protocol.



Source: Adapted from an article resulting from this thesis [41].

Table 11 – Post-processing protocol used in this work.

Temperature (°C)	Heating rate (°C / min)	Holding time (min)
30-350	1	-
350-400	0.5	-
400-440	0.2	-
440-600	0.5	-
600	-	60
600- T_{sint}	5	-
T_{sint}	-	120

Source: Elaborated by the author.

4.2.8 3D printing

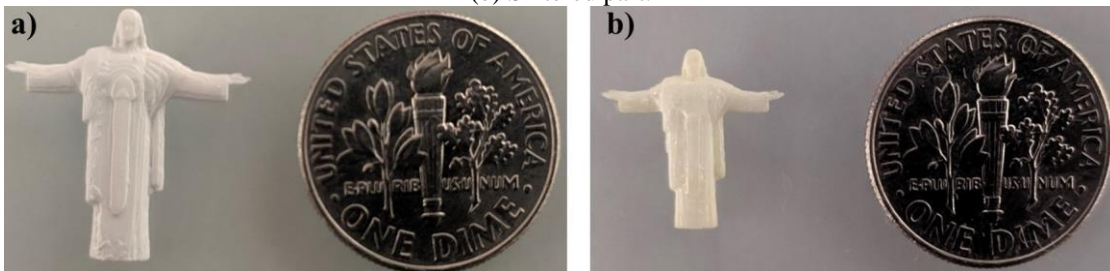
Ceramic slurries with 40 vol% of 3Y-TZP, 3 wt% of Disperbyk-111, and PEGDA 250 were chosen to test the manufacturability of the built prototype and of the commercial 3D printer. The DLP 3D printer prototype proved to be able to work with the prepared suspension and produced some ceramic green parts, as shown in Figure 45. The post-processing proposed in the previous subsection (see Table 11) was successfully performed, resulting in parts with no visible warping or delamination. Figure 46 shows a 3D printed part before and after sintering. These figures also represent the tiny details that can be obtained in ceramic parts by the manufacturing route used.

Figure 45 – 3Y-TZP green parts manufactured in the built prototype.



Source: Adapted from an article resulting from this thesis [41].

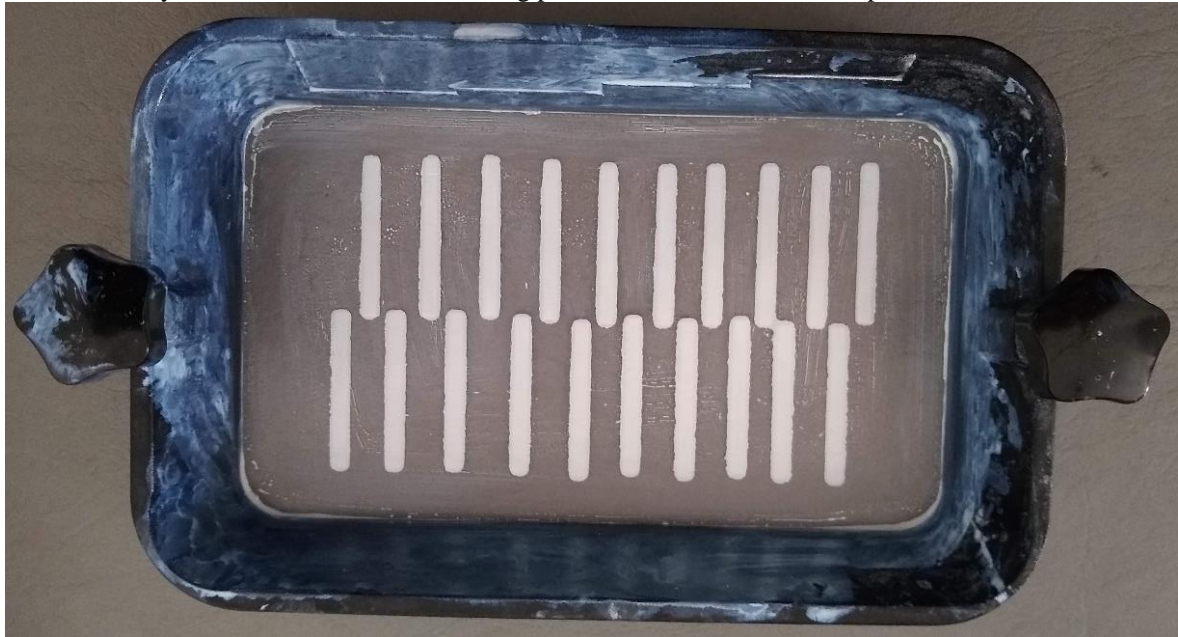
Figure 46 – 3Y-TZP printed adaptation of Christ the Redeemer Statue (Rio de Janeiro – Brazil). (a) Green part. (b) Sintered part.



Source: Adapted from an article resulting from this thesis [43].

On the other hand, the bottom-up commercial printer failed during the manufacturing process. In this case, the first layer sticks to the bottom of the vat, instead of adhering to the building platform (Figure 47), a problem called sticking [258]. This test evidences that different 3D printers have distinct requirements and that using a suspension with a viscosity lower than 3 Pa.s is not sufficient for any vat photopolymerization equipment.

Figure 47 – Top view of the vat after removal of the 3Y-TZP suspension, indicating a “sticking” printing failure: the first layer does not adhere to the building platform and sticks to the transparent bottom of the vat.



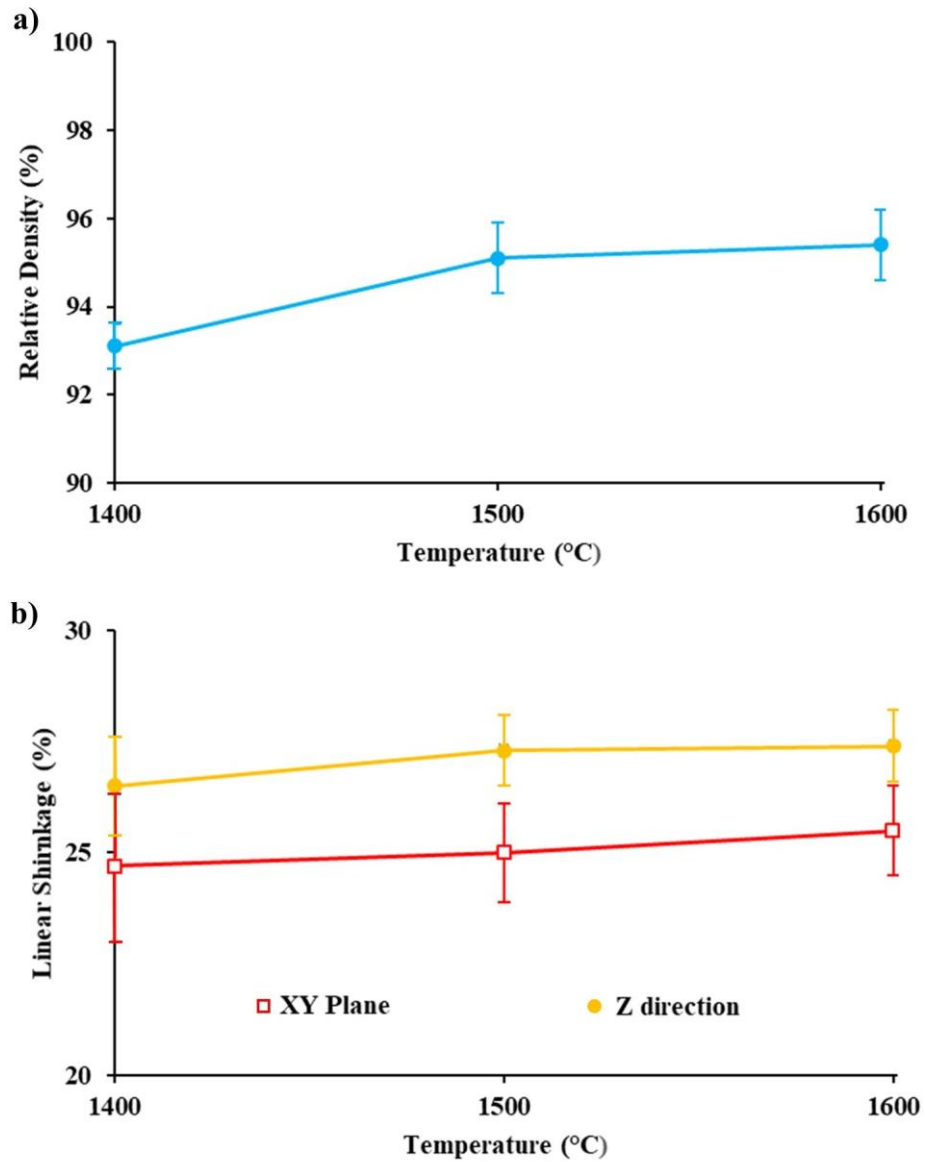
Source: Elaborated by the author.

4.2.9 Sintered parts characterization

The relative density of the sintered parts was found to be greater than 95 % and the shrinkage was 25.0 % in the X-Y plane and 27.3 % in the Z direction. Despite the significant shrinkage difference, such results agree with what has been presented in the literature, in which related studies obtained even greater differences [131]. The use of a solvent-free formulation provided a significant decrease in shrinkage compared to the parts made with the solvent-based formulation previously used by our research group (shrinkage of 34% [39]).

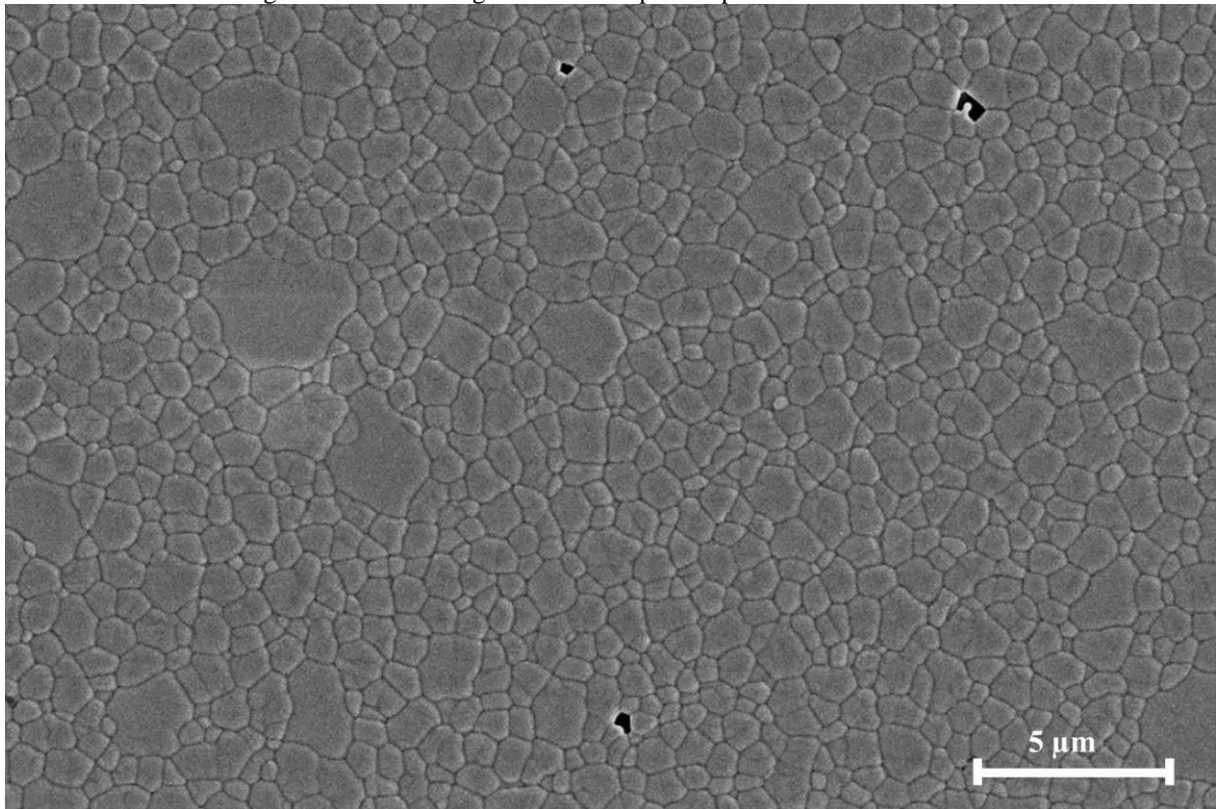
The linear shrinkage and relative density of the sintered ceramic parts increased with increasing sintering temperature (Figure 48). The shrinkage in the building direction was always higher than in the XY plane, evidencing the anisotropic nature of the process. Parts sintered at 1600 °C reached a relative density of 95.4% and their microstructure is represented in Figure 49. Although there is still residual porosity, abnormal grain growth can be noticed, with some grains being considerably larger than others [259]. Thus, a further increase in sintering temperature is not indicated, as large grains tend to impair properties such as mechanical strength [260].

Figure 48 – Characterization of 3Y-TZP printed parts sintered at different temperatures. a) Relative density. b) Linear Shrinkage.



Source: Adapted from an article resulting from this thesis [41].

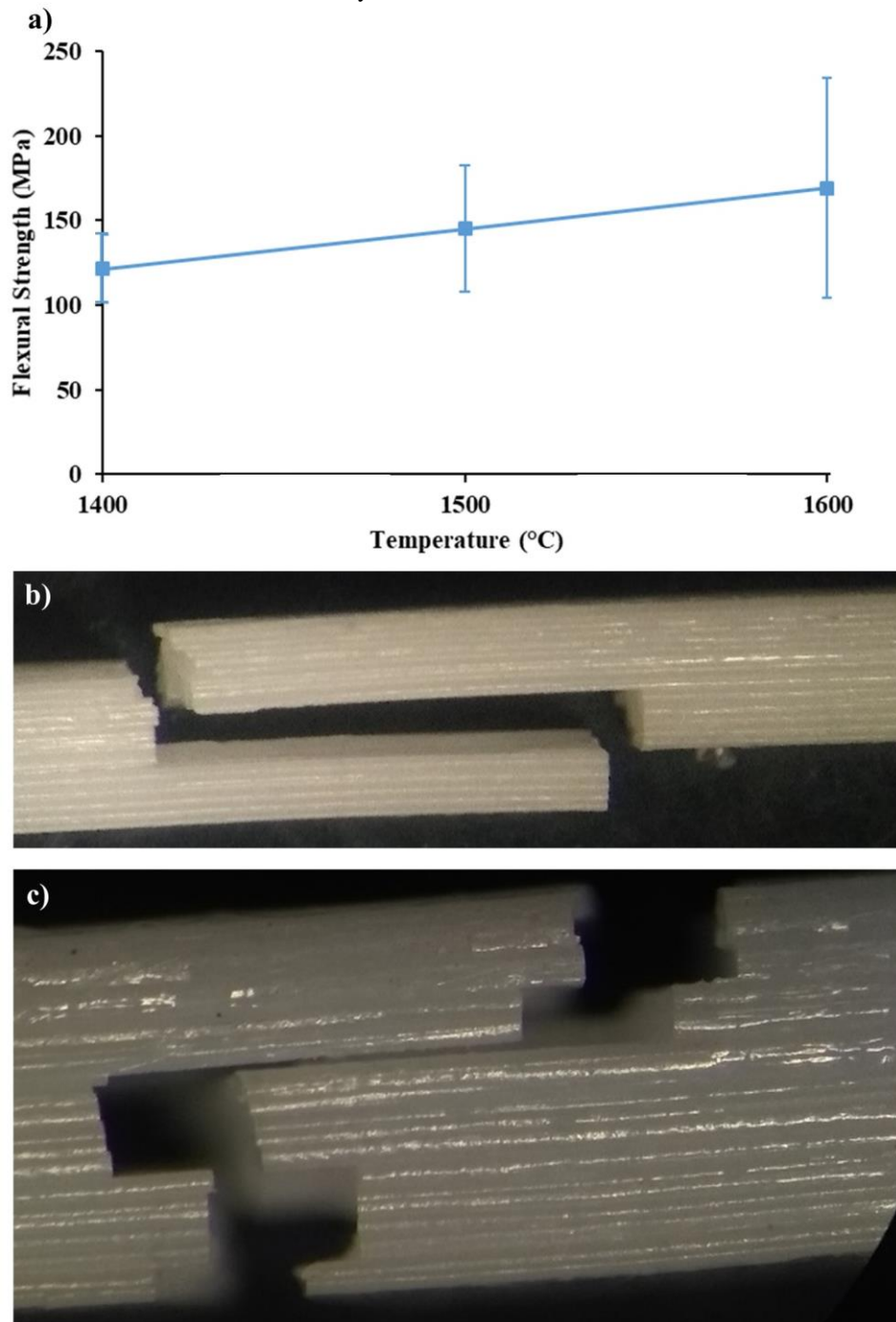
Figure 49 – SEM images of 3Y-TZP printed part sintered at 1600 °C.



Source: Elaborated by the author.

A tendency of increasing flexural strength with rising sintering temperature in the studied range can be observed in Figure 50a. Some parts sintered at 1600 °C exceeded 200 MPa, which is still significantly less than the value obtained for zirconia produced by conventional processes. Some specimens failed at the layers interface (Figure 50b), causing a great variation in the flexural strength obtained. Decreasing the layer thickness, adding components to the formulation as plasticizers, and variations in the post-processing may be the subject of future work and help to improve the properties of ceramic parts manufactured by DLP additive manufacturing.

Figure 50 – a) Flexural strength of the 3Y-TZP printed parts sintered at different temperatures. b) Specimens that failed at the layers interface in the flexural test.

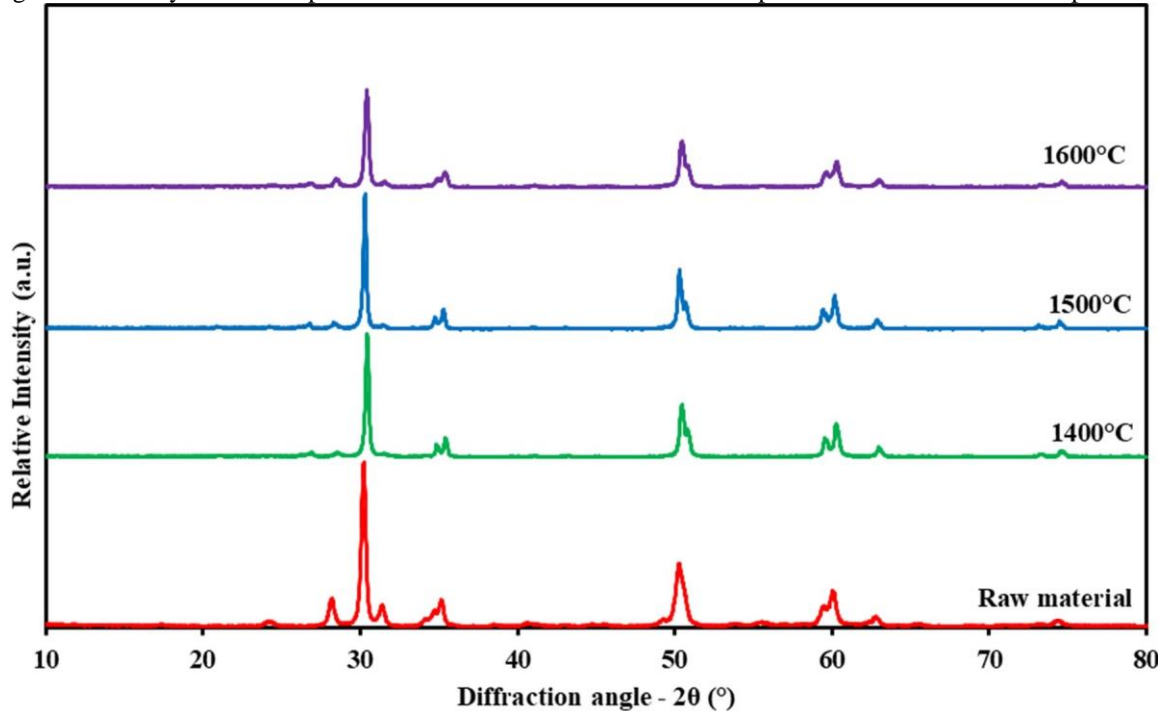


Source: Adapted from an article resulting from this thesis [43].

Figure 51 shows X-ray diffraction patterns for the raw material and parts sintered at different temperatures. The 3Y-TZP raw material presented not only a tetragonal but also a monoclinic phase, agreeing with what was presented in works that used the same raw material [254,261]. On the other hand, only the tetragonal phase was detected in all samples sintered at different temperatures (from 1400 to 1600 °C). This result was already expected, since the raw material has Y_2O_3 , which is a doping agent that partially stabilizes zirconia and avoids the

tetragonal to monoclinic phase transformation. Such transformation happens to unstabilized zirconia during the cooling (after sintering), causing volume expansion and resulting in cracked parts [261].

Figure 51 – X-ray diffraction patterns for the 3Y-TZP raw material and parts sintered at different temperatures.



Source: Elaborated by the author.

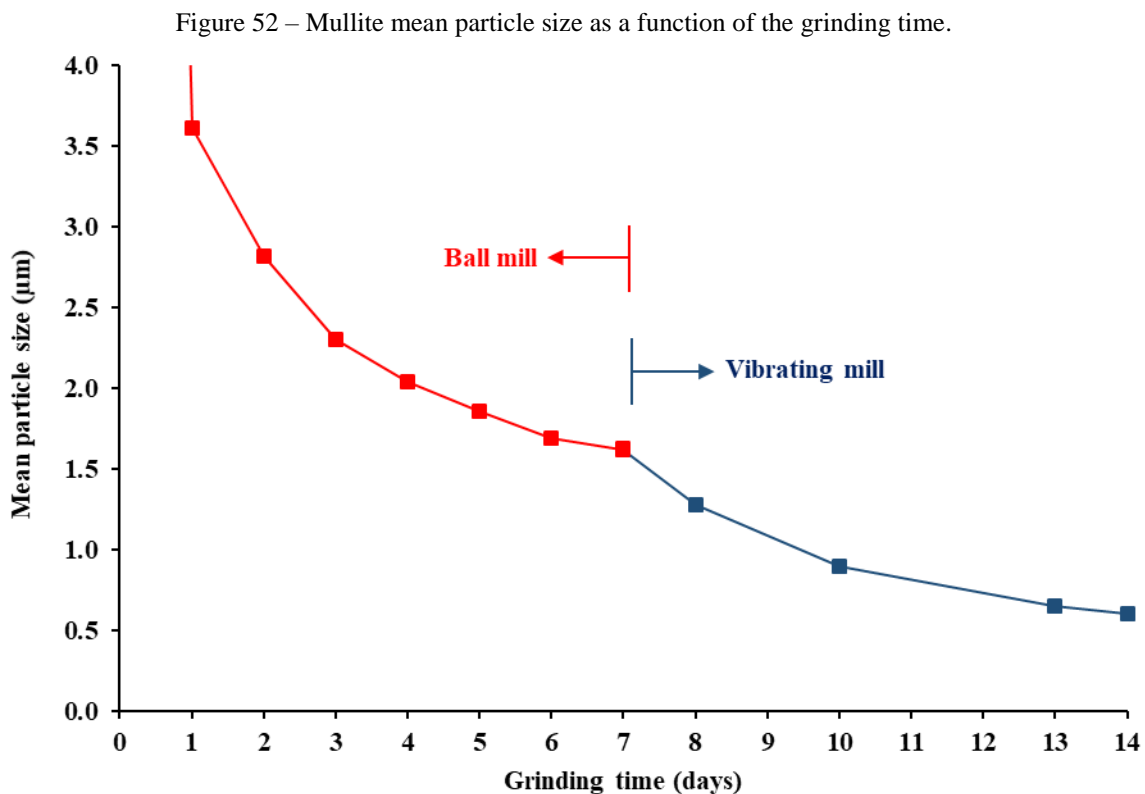
4.3 Additive Manufacturing of mullite: from coarse electrofused powder to ceramic parts using the built prototype and a low-cost commercial 3D printer

Parts of this subsection have been published as journal papers [44,46] and a conference paper [233].

Aiming to develop ceramic slurries compatible with both equipment (prototype and commercial 3D printer), a coarse ceramic powder was processed for use in the development of photosensitive ceramic suspensions based on the components (monomer, photoinitiator, and dispersant) chosen in the last section. The dispersant concentration was optimized and slurries suitable for the two machines were developed. After post-processing, 3D printed parts sintered at different temperatures were characterized (density, flexural strength, phase composition, and microstructure), as described next:

4.3.1 Ground powder characterization

Figure 52 presents the mean particle size as a function of the grinding time in a process consisting of sequential grinding in the ball mill and in the vibrating mill. The ball mill, with a predominantly impact grinding mechanism, reduced the average particle size by approximately 100 times on the first day. However, the rate of particle size reduction decreases with time and on the seventh day, the mean particle size was already approaching stabilization at around 1.6 μm , at which point there is a balance between breakage and agglomeration of particles [262]. Nevertheless, the particle size reached was still not within the submicron range recommended for ceramic vat photopolymerization [24]. Thus, the processing went through a new stage in the vibrating mill, with mixed impact and friction grinding mechanisms, also with decreasing grinding rates.

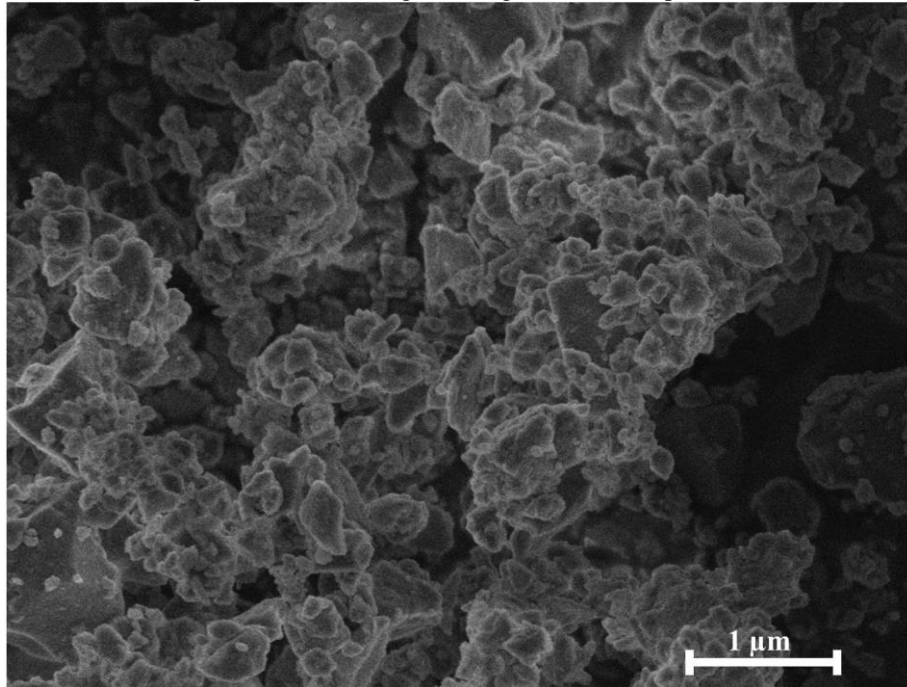


Source: Adapted from an article resulting from this thesis [233].

The obtained mean particle size (0.6 μm) is following the range adopted by most works related to ceramics vat photopolymerization [24]. Although finer particles would be more reactive during sintering [23,24,132], they would result in higher viscosity and hinder the preparation of highly loaded ceramic slurries [24]. Moreover, the measured specific surface

area was $15.7 \text{ m}^2/\text{g}$, like the one from the commercial 3Y-TZP powder used in this work. This is another parameter whose increase would also cause an increase in viscosity [107] and favor agglomeration [107,131]. Figure 53 presents the SEM images of the ground mullite powder. The presence of agglomerates justifies the proposed slurry preparation in a ball mill to break them and homogenize the suspension.

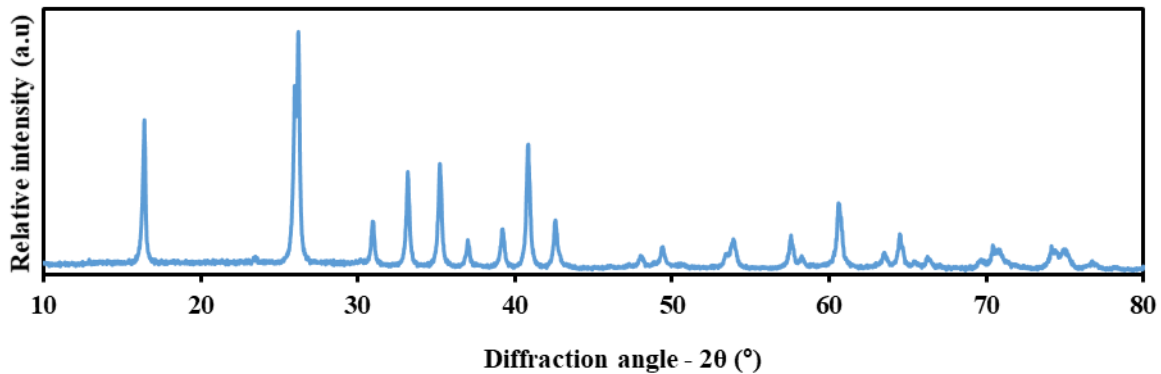
Figure 53 – SEM image of the ground mullite powder.



Source: Adapted from an article resulting from this thesis [233].

The wear analysis of the grinding media indicated a $1.0 \pm 0.1 \text{ g}$ decrease in the mass of zirconia balls during the 14-day grinding process. The presence of this zirconia was confirmed in the ground powder by X-ray fluorescence analysis. On the other hand, no peaks associated with zirconia were observed in the X-ray diffraction pattern and mullite was the only phase detected (Figure 54). The amount of zirconia was probably too small to favor the formation of secondary phases. Finally, the measured density of the ground mullite powder was $3.08 \text{ g}/\text{cm}^3$. This value is used for formulations and the calculation of relative densities during characterization.

Figure 54 – X-ray diffraction pattern for the ground mullite powder.



Source: Adapted from an article resulting from this thesis [233].

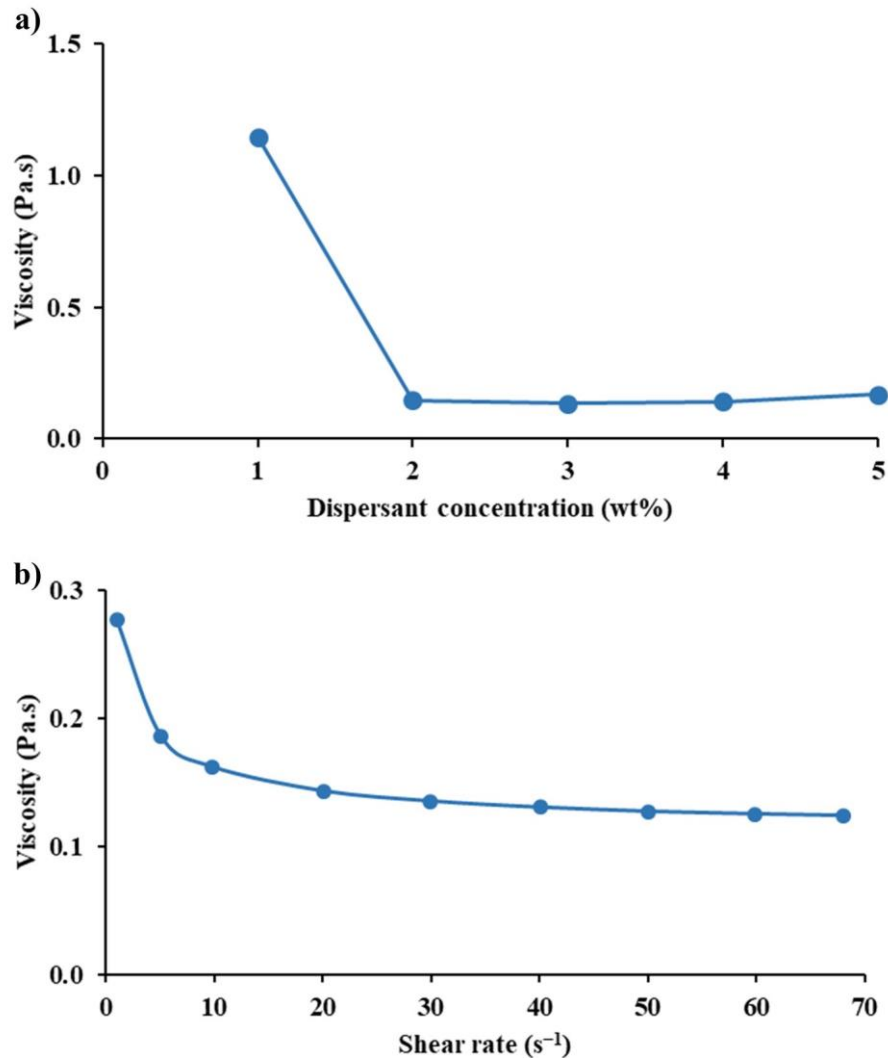
4.3.2 Choosing the dispersant concentration

First, slurries with 40 vol% of solid loading and dispersant concentration varying from 1 to 5 wt% (of the ceramic powder mass) were evaluated to find the optimal dispersant concentration.

Figure 55a presents the viscosity of 40 vol% ceramic loading slurries with varying concentrations of dispersants at a shear rate of 30 s^{-1} , showing that 3 wt% of Disperbyk 111 provided the lowest viscosity (0.135 Pa.s). All the prepared slurries showed shear-thinning behavior (decreased viscosity with increased shear rate, shown in Figure 55b). This behavior is desirable for DLP ceramic slurries [25,141,147] since it avoids the sedimentation of the suspension at rest and allows flow when a shear rate is applied [24,78].

The 40 vol% ceramic loading slurries with dispersant concentration up to 3 wt% presented negligible sedimentation in 30 days with retained volume fraction greater than 99%, indicating stable slurries suitable for DLP additive manufacturing. On the other hand, suspensions with 4 and 5 wt% of dispersant, presented up to 2 vol% of the liquid at the top of the suspension, which may indicate an excess in the amount of the dispersant.

Figure 55 – Rheological behavior of mullite slurries with 40 vol% solid loading (a) varying dispersant concentrations at a shear rate of 30 s^{-1} . (b) Viscosity curve with 3 wt% of dispersant (concentration which provided the lowest viscosity).



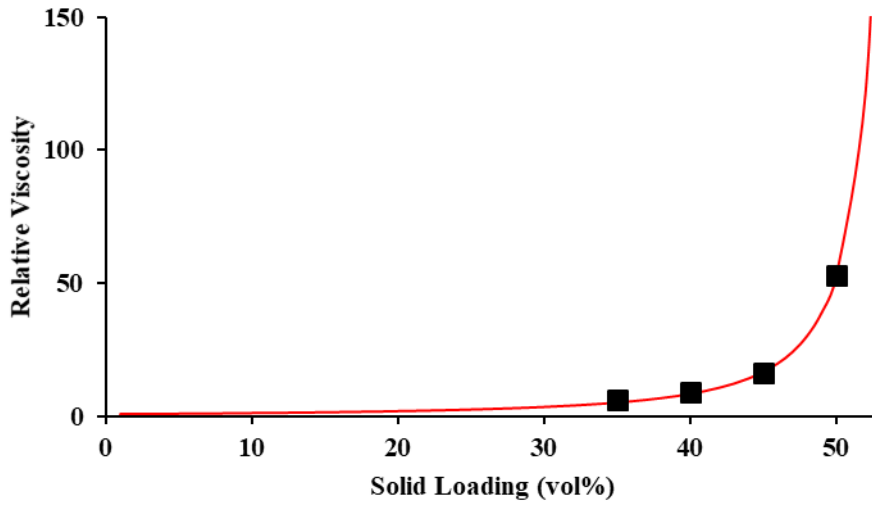
Source: Adapted from an article resulting from this thesis [44].

4.3.3 Influence of solid loading on the viscosity

The influence of the solid loading suspensions was considered by characterizing the rheology of slurries with the optimum amount of dispersant (3 wt%) and different ceramic loadings (from 35 to 50 vol%).

Figure 56 shows the viscosity of mullite suspensions with different ceramic volume fractions and with the found optimum amount of dispersant (3 wt%). The Krieger-Dougherty Model (Equation 4, subsection 2.6.2.1) [173] was used to relate viscosity and solid loading and to estimate the maximum solid fraction as 55.1 vol% ($R^2 \cong 0.999$).

Figure 56 – Influence of solid loading in mullite slurries at a shear rate of 30 s^{-1} .

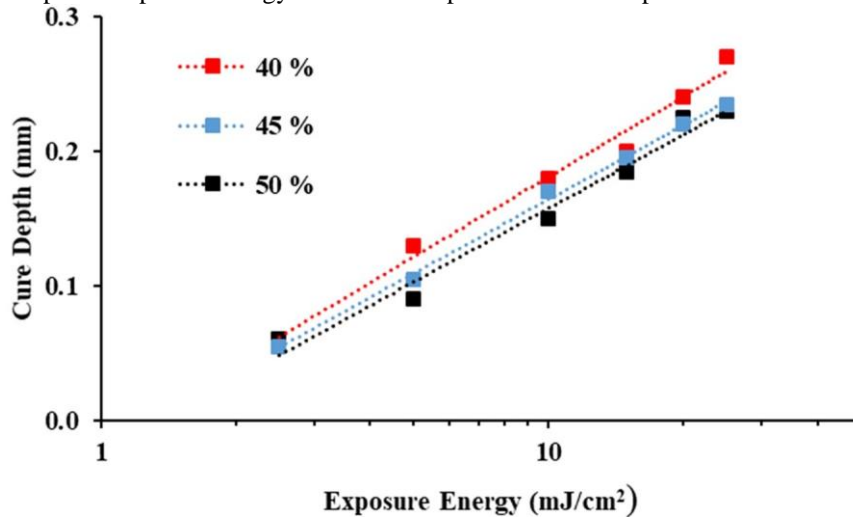


Source: Adapted from an article resulting from this thesis [44].

4.3.4 Photosensitive parameters

Figure 57 shows the relation between the cure depth and exposure energy of the mullite photosensitive suspensions with different solid loading. The critical energy found increased with an increase in the solid loading, varying between 1.21 and 1.35 mJ/cm^2 , being comparable with the values obtained in the literature for photosensitive ceramic suspensions [143,146].

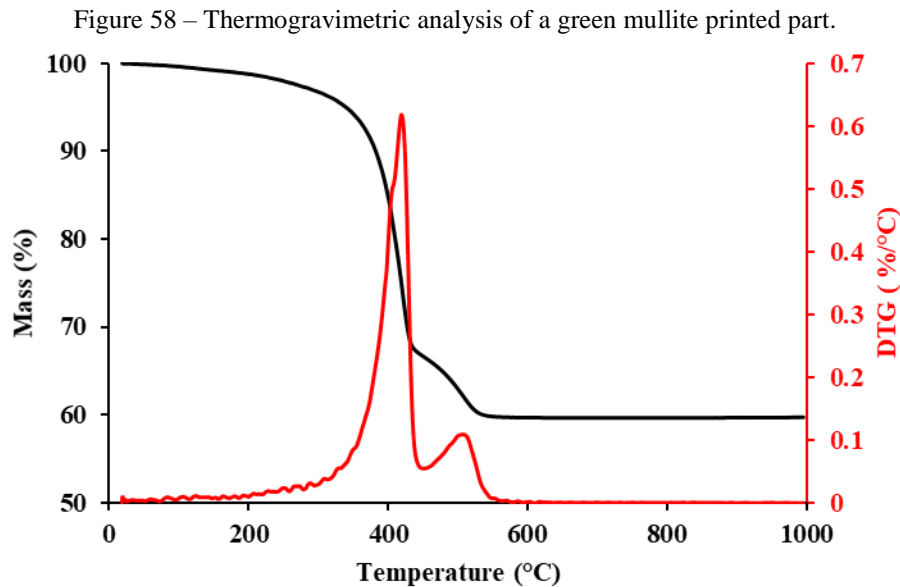
Figure 57 – Cure depth vs exposure energy of the mullite photosensitive suspensions with different solid loading.



Source: Adapted from an article resulting from this thesis [233].

4.3.5 Thermal analysis

The thermogravimetric analysis is shown in Figure 58. Since the organic components are the same as the zirconia formulation, the decomposition is similar (happening mostly between 350 and 600 °C, with the maximum peak around 400 °C). Thus, the same post-processing protocol was used (see Table 11 in subsection 4.2.7).

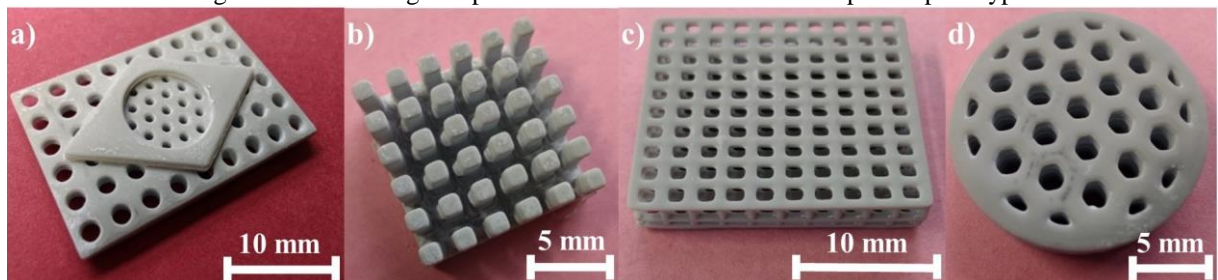


Source: Adapted from an article resulting from this thesis [44].

4.3.6 3D printing

Ceramic slurries with a solid loading of 40, 45, and 50 vol% were chosen to test the manufacturability on the built prototype and in the commercial 3D printer. The DLP 3D printer prototype proved to be able to work with all these suspensions, which was expected since it had already 3D printed using the zirconia slurry, which was even more viscous. Figure 59 shows some parts manufactured in the prototype.

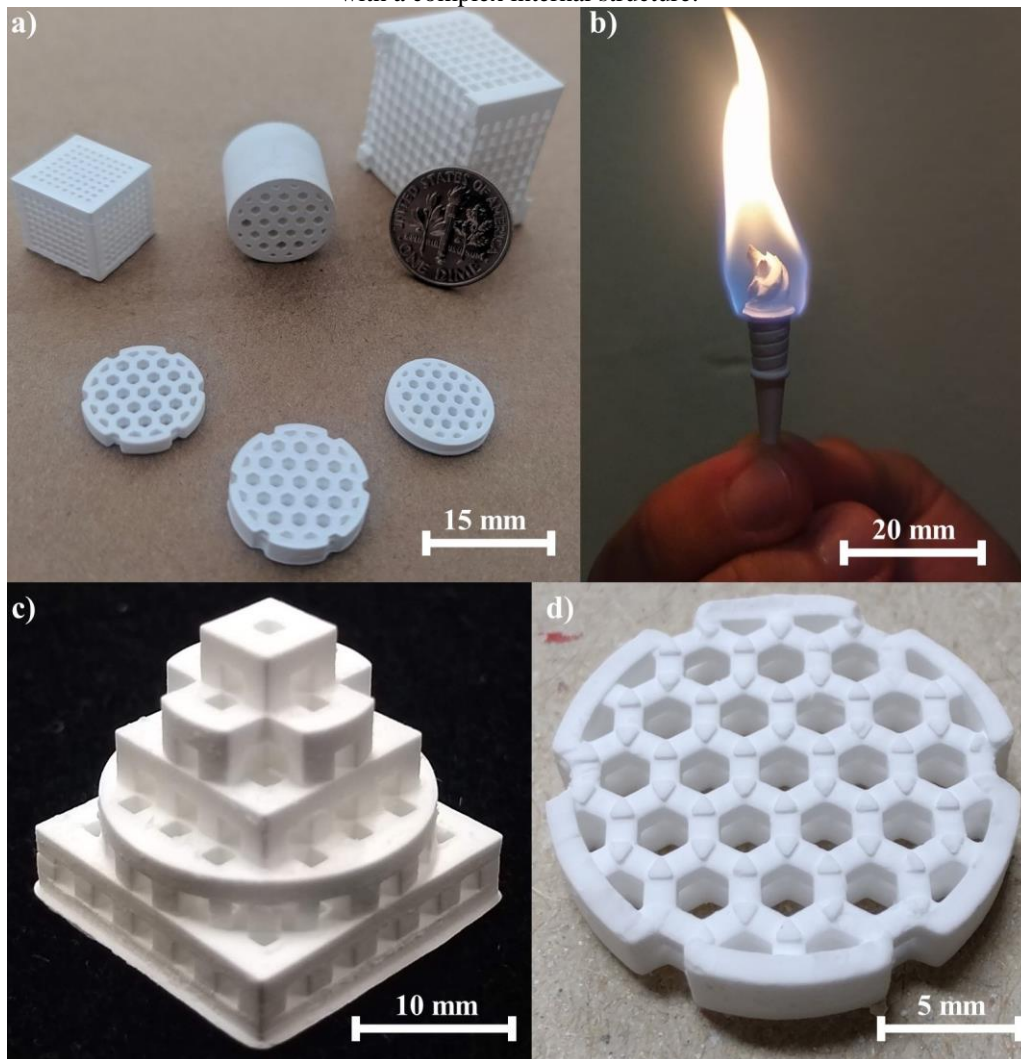
Figure 59 – Mullite green parts manufactured in the DLP 3D printer prototype.



Source: Elaborated by the author.

The commercial equipment was also able to manufacture parts with the mullite suspensions with the different solid loadings. Figure 60 shows sintered parts manufactured in the commercial 3D printer. Figure 60b is a pictorial reference to the high-temperature resistance and good thermal insulation of mullite, while Figure 60d shows a part with a complex internal structure.

Figure 60 – Mullite sintered 3D printed parts. a) Miscellaneous components. b) Torch. c) Pyramid. d) Scaffold with a complex internal structure.



Source: Adapted from an article resulting from this thesis [44].

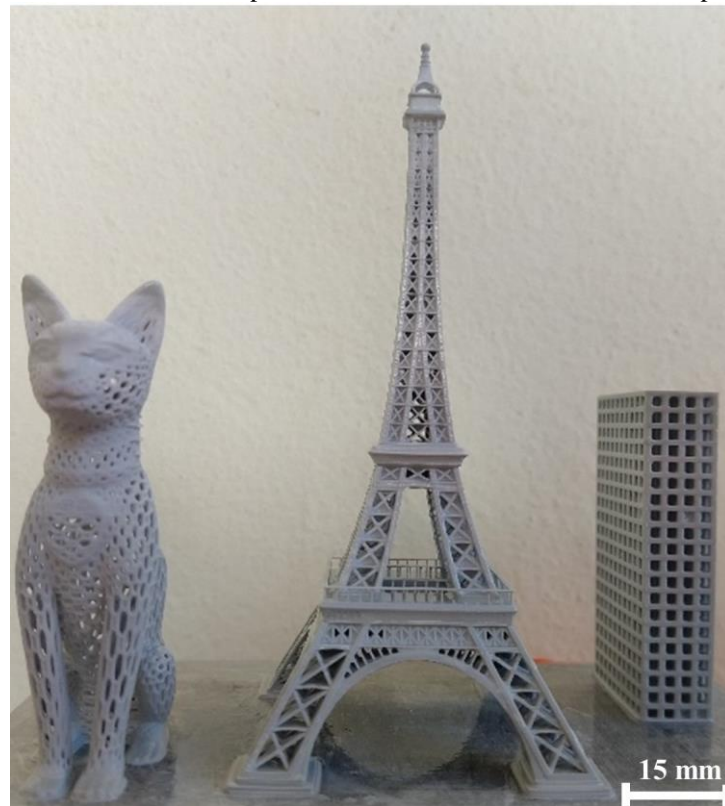
4.3.7 Comparison between built prototype and commercial 3D printer

Although both devices have proven capable of printing with mullite suspensions, it is important to point out some differences between them. The great advantage of the prototype is related to its dedicated recoating system, which allows it to deal with more viscous suspensions (over 2.0 Pa.s), as previously discussed in the subsection 4.2.8. On the other hand, the

commercial 3D printer stands out for its ability to print larger parts and reduce light emission time per layer.

The commercial equipment has a large print volume ($130 \times 82 \times 160 \text{ mm}^3$). This is possible, since the “bottom-up” approach, with the formation of layers, always occurring at the bottom of the vat, allows the equipment to operate without it being full, reducing the costs of experiments and waste [14,35,69]. In this way, such equipment is capable of manufacturing ceramic pieces that exceed 100 mm in height (as illustrated by the Eiffel Tower, in Figure 61).

Figure 61 – Green mullite parts manufactured in the commercial 3D printer.



Source: Elaborated by the author.

On the other hand, the formation of layers on the transparent bottom of the vat in the “bottom-up” approach requires a periodic detachment of the component being manufactured, which is aggravated for suspensions with high viscosity, which cause high adhesion of the part to the bottom of the vat [71] and also for parts with large cross-sections [263]. For example, in this work, parts with cross-sections greater than 1000 mm^2 failed even with the least viscous slurries. Large cross-sections increase the separation force between the newly cured layer and the bottom of the vat, which may cause the first layer to be stuck in the bottom of the vat (sticking fail, shown in Figure 47 in subsection 4.2.8) or part of the piece detaches from the build platform as shown in Figure 62. Trying to avoid such a problem, the part to be

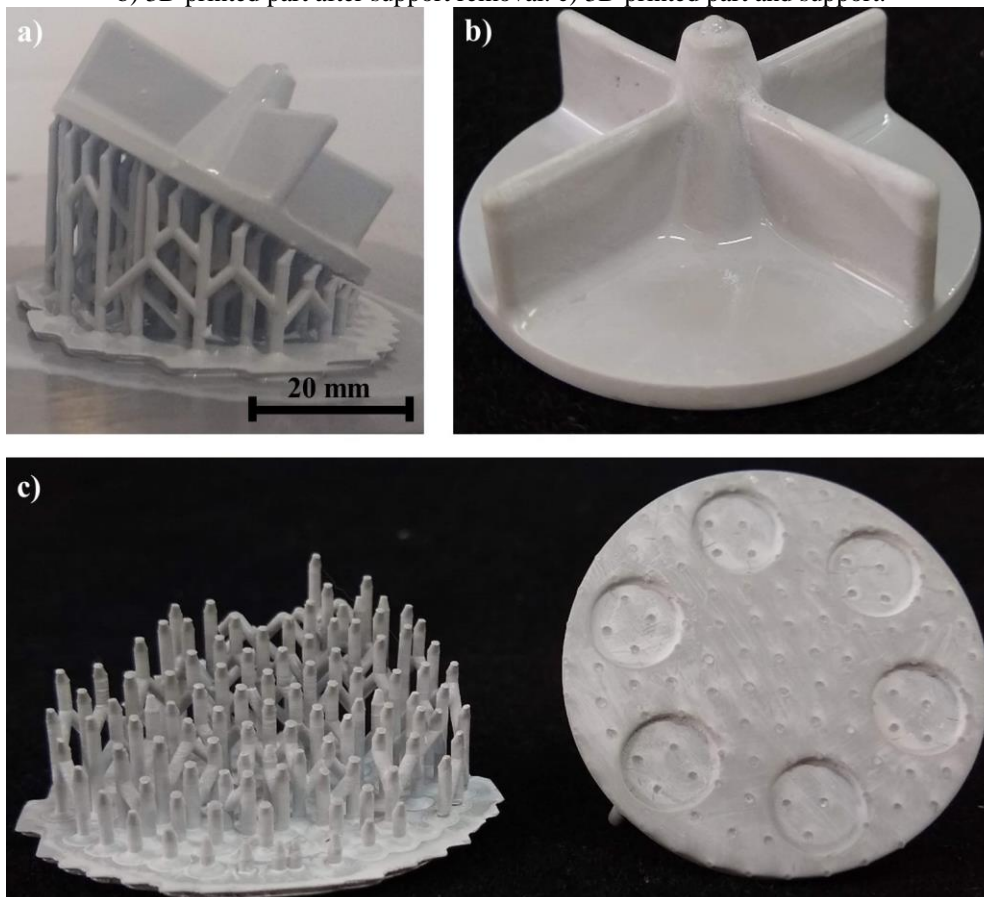
manufactured can be rotated (decreasing the maximum printing section) and supports added, as illustrated in Figure 63, which shows the part being printed successfully. However, the anisotropic shrinkage, characteristic of the process [7,8,43,131], generates post-processing cracks, as shown in Figure 64.

Figure 62 – 3D printing fail of a mullite green part: partial detachment from the build platform.



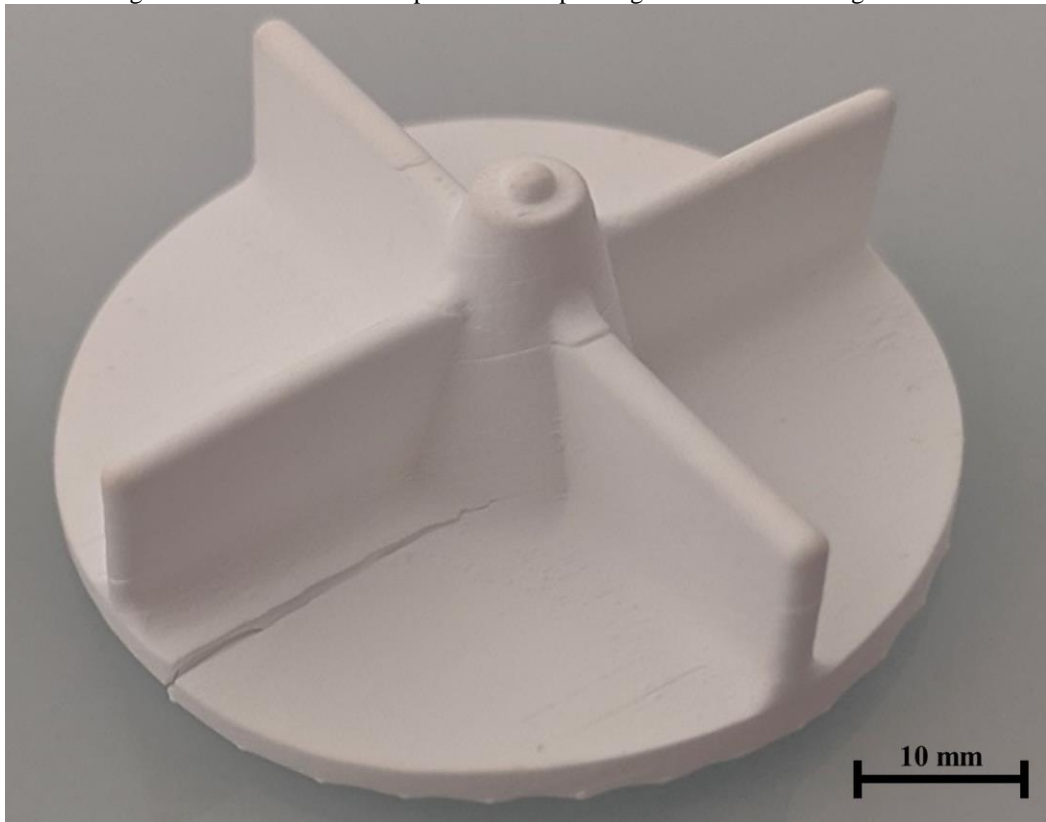
Source: Adapted from an article resulting from this thesis [46].

Figure 63 – Successful 3D printing of mullite part with inclined orientation. a) 3D printed part with the support. b) 3D printed part after support removal. c) 3D printed part and support.



Source: Adapted from an article resulting from this thesis [46].

Figure 64 – Mullite sintered part from 3D printing with inclined configuration.



Source: Adapted from an article resulting from this thesis [46].

Meanwhile, the “top-down” prototype, with the formation of layers occurring on the top of the vat, needs the vat to be full for the manufacture of parts to occur [264]. Therefore, the equipment has a lower printing volume ($50 \times 20 \times 25 \text{ mm}^3$) to enable experiments to be carried out without the use of a large amount of raw material, which restricts its application only to smaller pieces (Figure 59) than those produced by commercial equipment. It is possible to overcome this limitation by increasing the vat and the build platform, which, on the other hand, would increase the amount of material needed for fabrication.

The light emission time per layer of the prototype (20 sec) is more than 10x longer than the exposure time required in the commercial 3D printer. This is explained by the different light sources. The commercial printer has a monochromatic light source with a wavelength that corresponds to the photoinitiator's range of higher light absorption. On the other hand, the prototype uses a commercial slide projector with a mercury vapor lamp with emissions occurring predominantly in the visible light range and thus having only a small portion of useful irradiance, as previously discussed in section 3.2. Such a disadvantage would be overcome by using a projector with emission in the UV band.

4.3.8 Post-processing challenge

Although complex parts with tiny structures can be printed (Figure 65a), some submillimetric features may present distortion issues during post-processing. It might even make the part break (Figure 65b and c). The influence of solid loading, feature size, aspect ratio, and deposition direction on distortion may be the subject of future work. In addition, pieces with large wall thickness would lead to cracks in the debinding of thick sections [11,79]. Major suppliers of equipment and feedstock related to ceramic VP specify 10 mm as the maximum wall thickness to be produced [79,222].

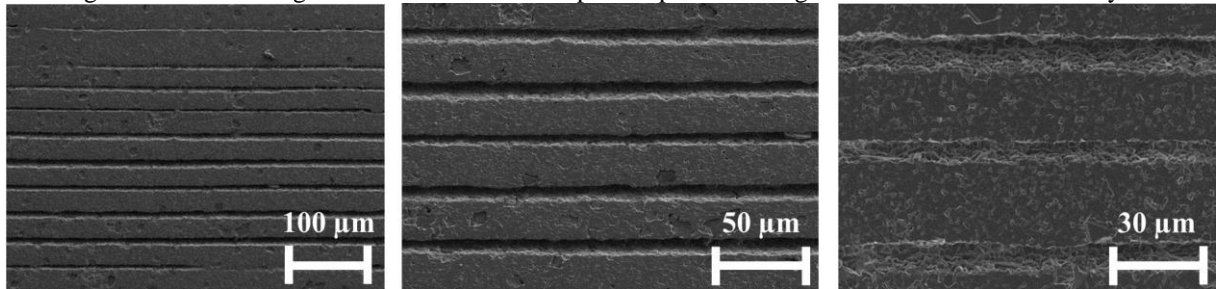
Figure 65 – Mullite 3D printed part with tiny structures. a) Green part (Eiffel Tower). b) Base of the tower after breaking during post-processing. c) Piece of the tower after breaking during post-processing.



Source: Adapted from an article resulting from this thesis [44].

Finally, it is important to point out that the interface between the layers remains a region of concern even after sintering, as illustrated in Figure 66. This finding corroborates the anisotropy of mechanical properties reported in related works [6,265–268].

Figure 66 – SEM images of sintered mullite 3D printed parts showing the interface between the layers.



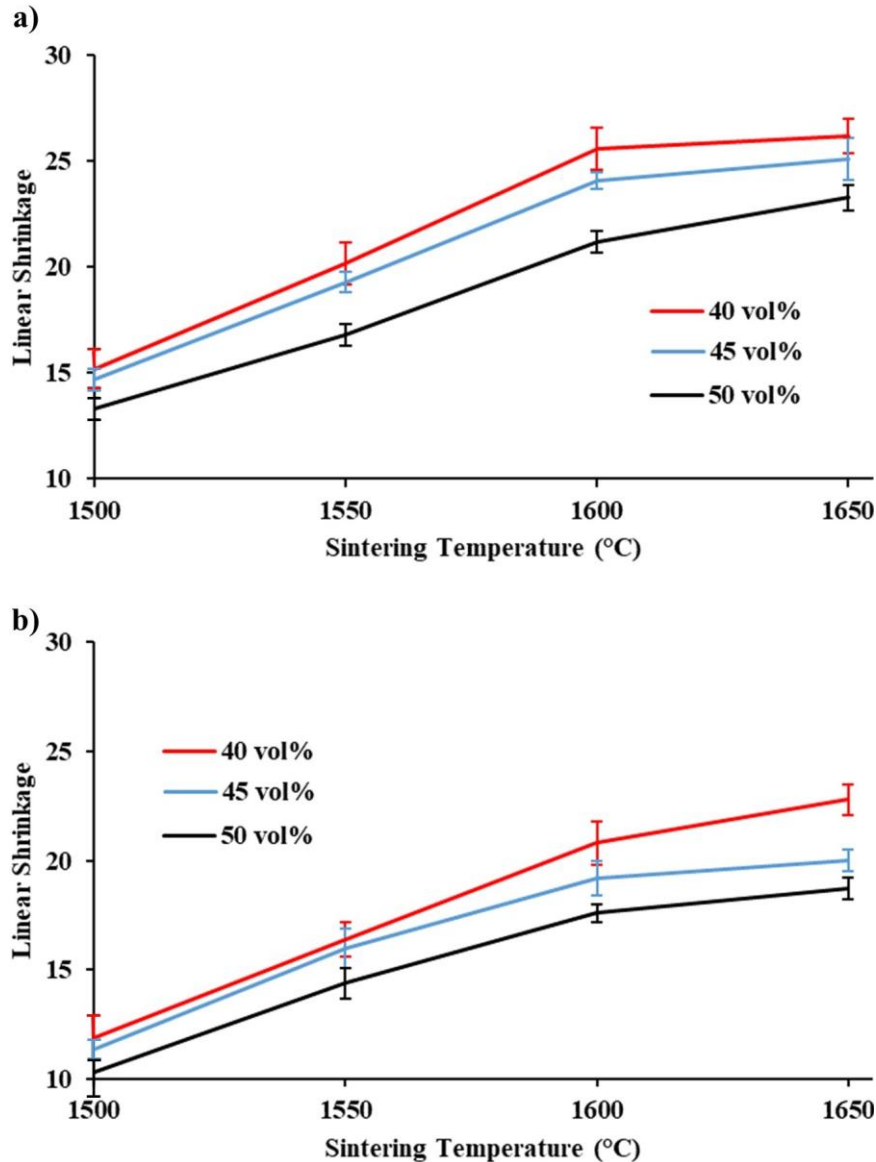
Source: Elaborated by the author.

4.3.9 Influence of solid loading and sintering temperature on final parts

In this subsection, the influence of solid loading and sintering temperature on linear shrinkage, density, flexural strength, phase composition, and microstructure is discussed. Considering the large number of samples needed for this study, the commercial 3D printer was chosen to manufacture the specimens from suspensions of 40, 45, and 50 vol% of solid loading, since it has a larger building area and printing speed. In addition, the fact that the printer used is commercially available at a low cost makes it easier for research to be continued elsewhere. Finally, the samples were debound and sintered at different temperatures (1500, 1550, 1600, and 1650 °C) and characterized, as described next:

As expected, the linear shrinkage increased with increasing sintering temperature and decreased with an increase in the solid loading, as shown in Figure 67. It can also be observed that the shrinkage in the building direction was significantly higher than in the XY plane. For example, for parts with 50 vol% sintered at 1650 °C, the Z-direction linear shrinkage was $23.3 \pm 0.6 \%$ while it was $18.7 \pm 0.5 \%$ in the XY plane. Such anisotropy has been presented in related works [7,8,43,131] and is associated with layered manufacturing of the process.

Figure 67 – Influence of sintering temperature and solid loading on linear shrinkage of mullite 3D printed parts.
 a) Linear shrinkage in the building direction. b) Linear shrinkage in the XY plane.

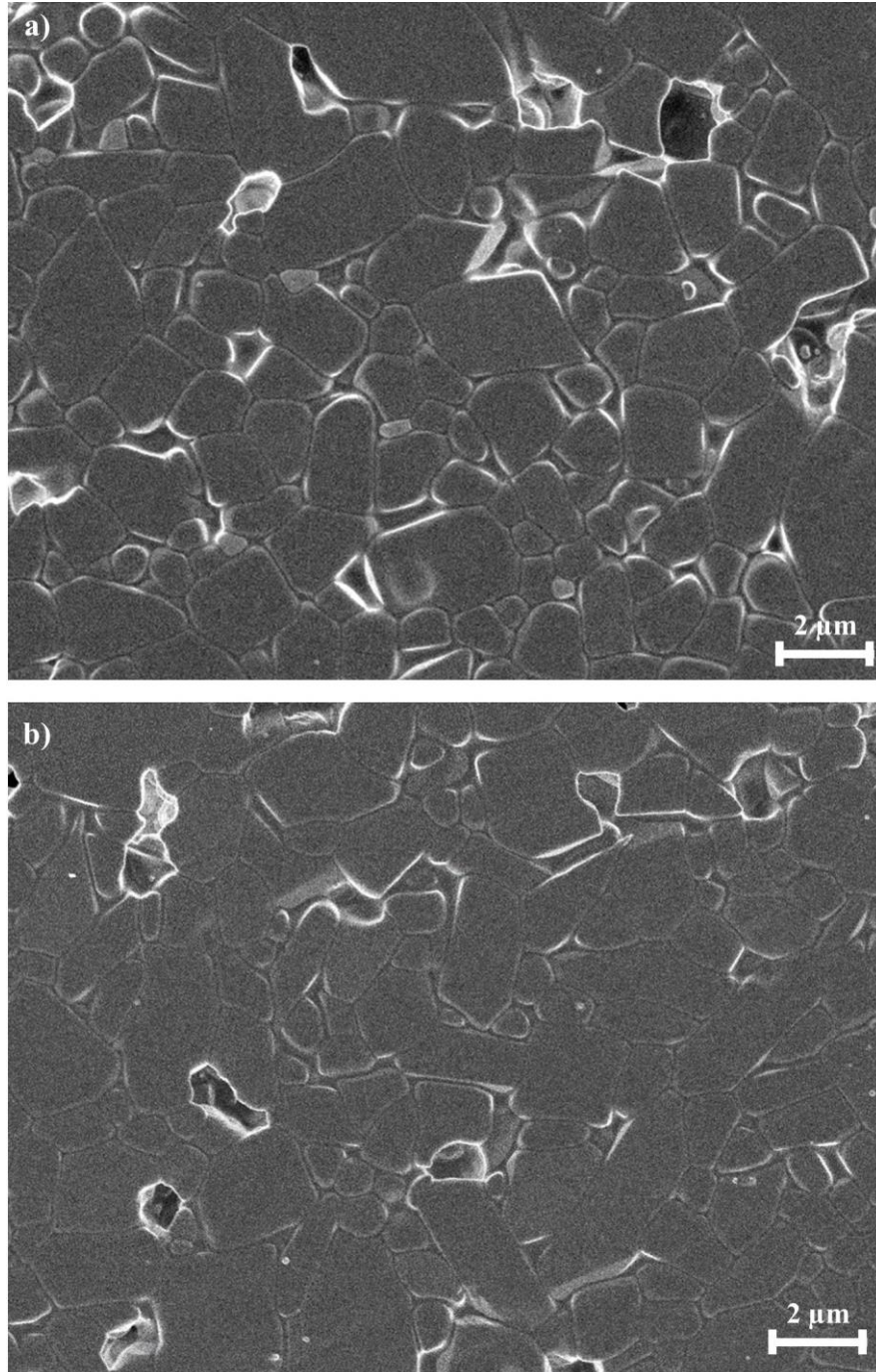


Source: Adapted from an article resulting from this thesis [44].

Figure 68 presents SEM images illustrating the decrease in porosity of parts sintered at the same temperature with increasing solid loading. Figure 69a and b show an increase in the average value of both, relative density and flexural strength with increasing sintering temperature and solid loading. The subsequent sintering step at 1650 °C made a big difference in relative density and even greater in the flexural strength. For example, parts with 40 vol% increased density from 85.5 ± 0.5 to 92.8 ± 0.6 % and flexural strength from 47.9 ± 4.3 to 65.0 ± 4.7 MPa when the sintering temperature increased from 1600 °C to 1650 °C. Moreover, solid loading also had a huge influence on these properties, and parts with 50 vol% sintered at 1650 °C reached 97.7 ± 0.3 % and 95.2 ± 5.0 MPa of relative density and flexural strength, respectively. The flexural strength obtained is greater than that obtained in other works related

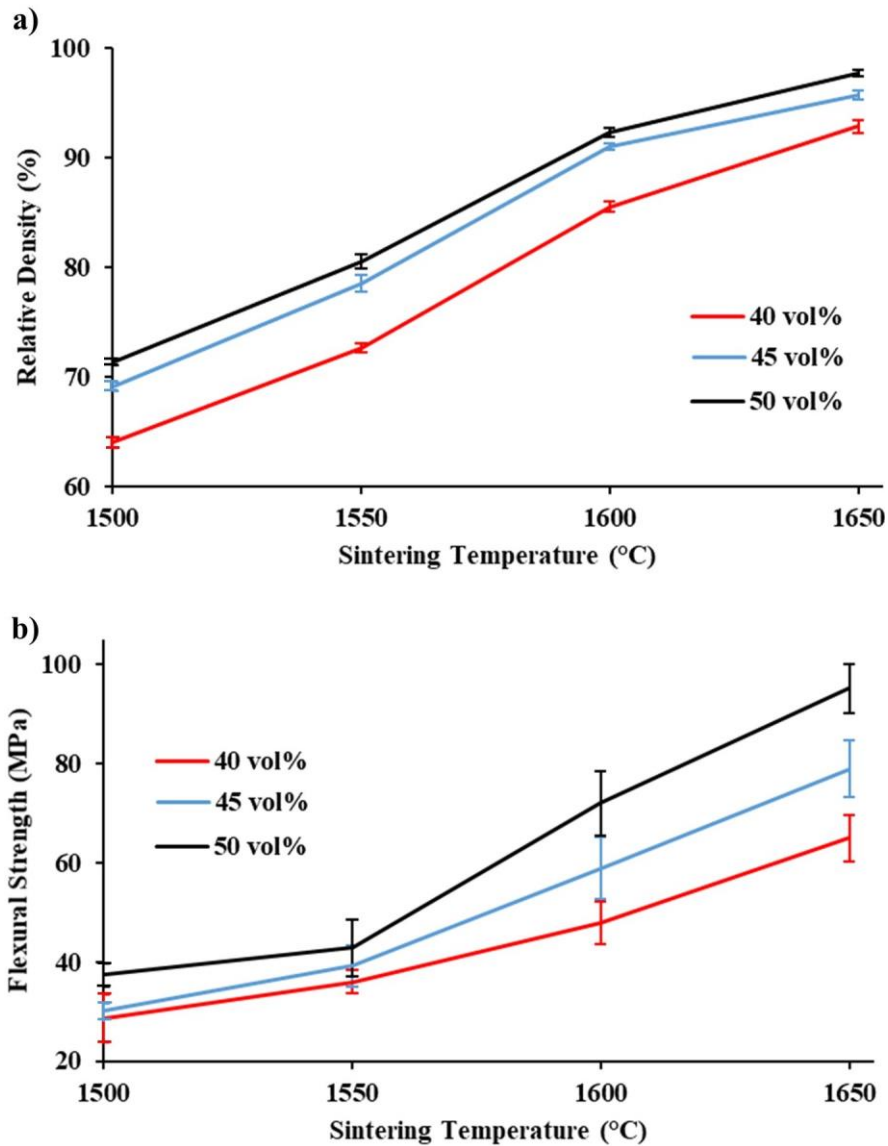
to the additive manufacturing of $\text{SiO}_2\text{-Al}_2\text{O}_3$ refractories [269,270] and comparable to mullite obtained by conventional processes [271–273].

Figure 68 – SEM images of mullite parts sintered at 1600 °C from suspensions with different solid loading. a) 45 vol%. b) 50 vol%.



Source: Elaborated by the author.

Figure 69 – Influence of sintering temperature and solid loading on properties of mullite 3D printed parts. a) Relative density. b) Flexural strength.

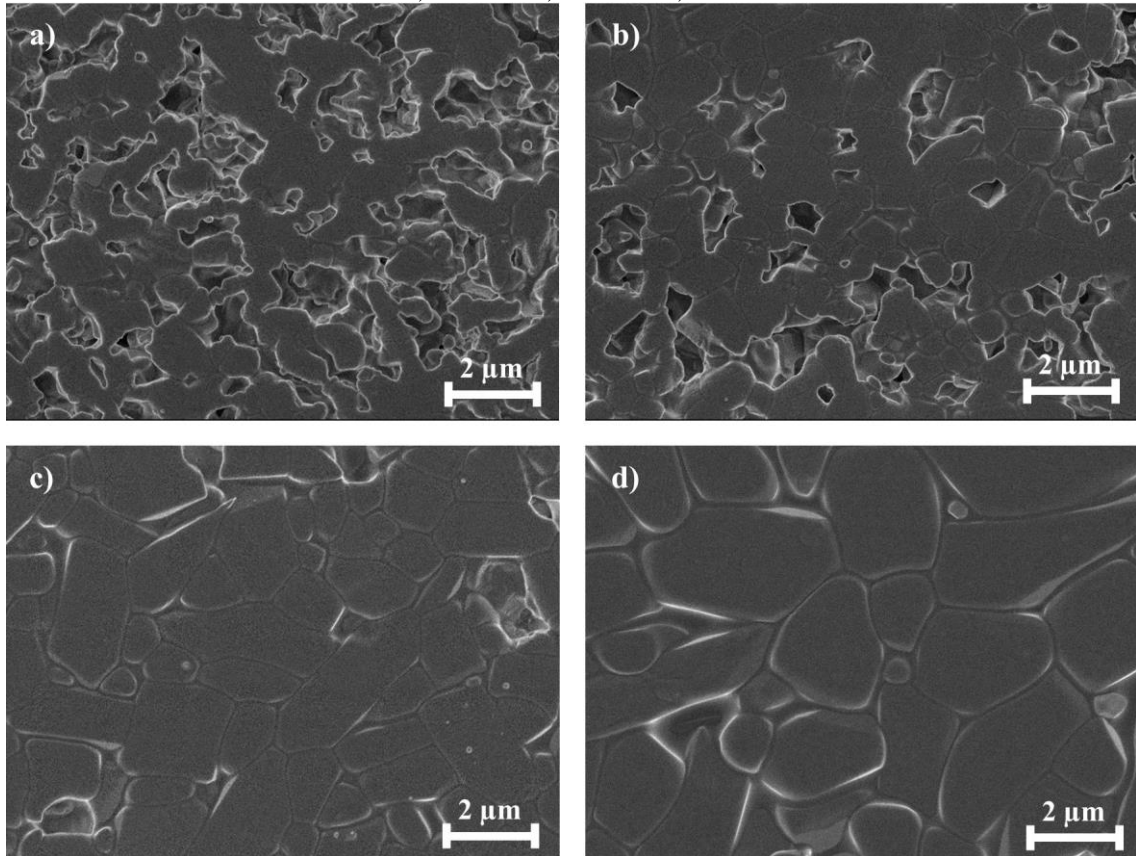


Source: Adapted from an article resulting from this thesis [44].

In general, commercial fused mullite may contain a low amount of glass phase owing to incomplete crystallization or by the presence of impurities such as calcium oxide, sodium oxide, etc. However, the liquid phase is significant just for $\text{Al}_2\text{O}_3/\text{SiO}_2$ ratios below 2.85 or a high amount of impurities. The electrofused mullite used in this work has an $\text{Al}_2\text{O}_3/\text{SiO}_2$ ratio of around 3.0 and a negligible amount of impurities. Thus, the densification of this work is predominantly related to “solid-state sintering” [238]. The SEM images (Figure 70) indicate that the primary mechanism of densification is grain boundary diffusion, similar to what was presented by Sacks [274]. After the initial sintering stage with neck growth, porosity from continuous open channels (Figure 70a and 70b) evolves into closed pores (Figure 70c). Lastly,

Figure 70d illustrates the coarsening with grain growth coupled with pore growth, consistent with what has been presented in related works [238,274,275].

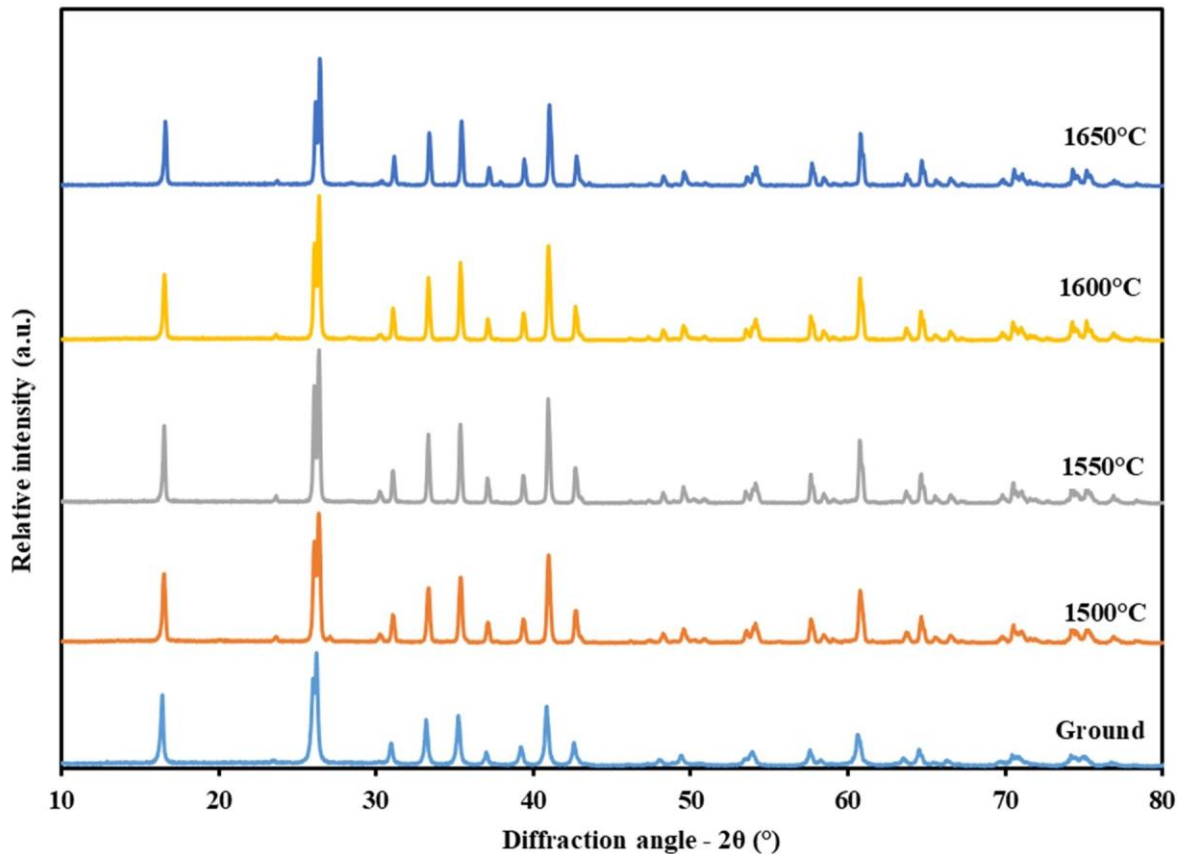
Figure 70 – SEM images of mullite parts sintered from 50 vol% suspensions at different temperatures. a) 1500 °C. b) 1550 °C. c) 1600 °C. d) 1650 °C.



Source: Adapted from an article resulting from this thesis [44].

Figure 71 shows X-ray diffraction patterns for the raw material and parts sintered at different temperatures, indicating no significant crystallinity change during sintering, with mullite being the only phase detected in all samples. The use of a crystalline mullite powder is the reason why high temperatures are required in the sintering process [238,276], given the low diffusion rate of aluminum and silicon ions, which justifies the demand for a fine powder with a high specific surface area [238,277] and the grinding protocol adopted in this work. Nevertheless, high temperatures (above 1600 °C) were required to obtain the best results, which restricts its application. Sintering additives such as Y_2O_3 [278] and MgO [279,280] decrease the sintering temperature of mullite due to the liquid phase formation, and their use in photosensitive ceramic suspensions may be the subject of future works.

Figure 71 – X-ray diffraction patterns for the mullite raw material and parts sintered at different temperatures.



Source: Adapted from an article resulting from this thesis [44].

4.4 Additive manufacturing of in situ mullite-zirconia composites

Parts of this subsection have been published as a journal paper [47].

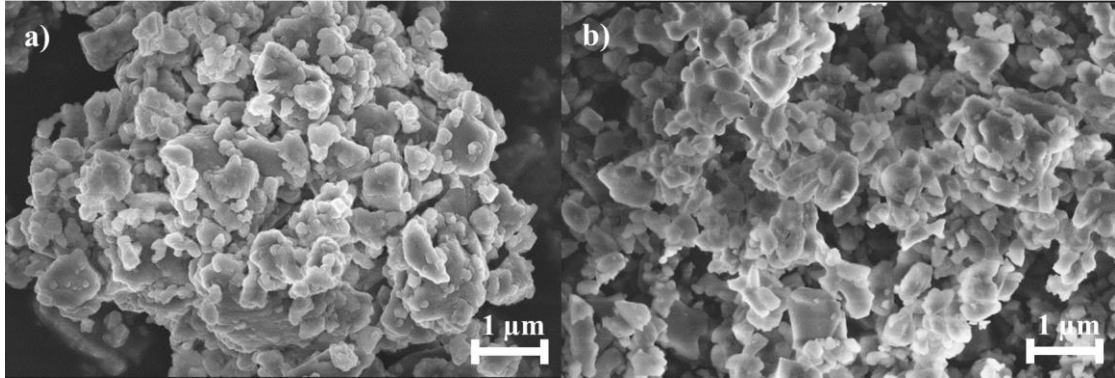
Aiming to manufacture in situ mullite zirconia composites parts, a coarse zircon ceramic powder was processed for use with calcined alumina in the preparation of photosensitive ceramic suspensions. The commercial 3D printer was chosen to 3D print the green parts. The parts sintered under different temperatures were characterized and the reaction sintering was analyzed, as described next.

4.4.1 Powder characterization

Figure 72 presents the SEM images of the powders used in the ceramic suspensions. According to the analysis of the Laser Particle Sizer, the commercial alumina powder presented a mean particle size of 0.8 μm . The zircon powder reached the same mean particle size after being processed in a ball mill for 7 days and subsequently in a vibrating ball mill also for 7 days. Such value is similar to what has been used in related works [24]. Finer particles would

be desirable to improve sintering reactivity [23,24,132], but they would increase the suspension viscosity, limiting the solid loading that could be added to prepare a ceramic slurry suitable for DLP additive manufacturing [24,44].

Figure 72 – SEM images of the ceramic powders used in the preparation of the photosensitive suspensions. a) Calcined Alumina. b) Ground Zircon.



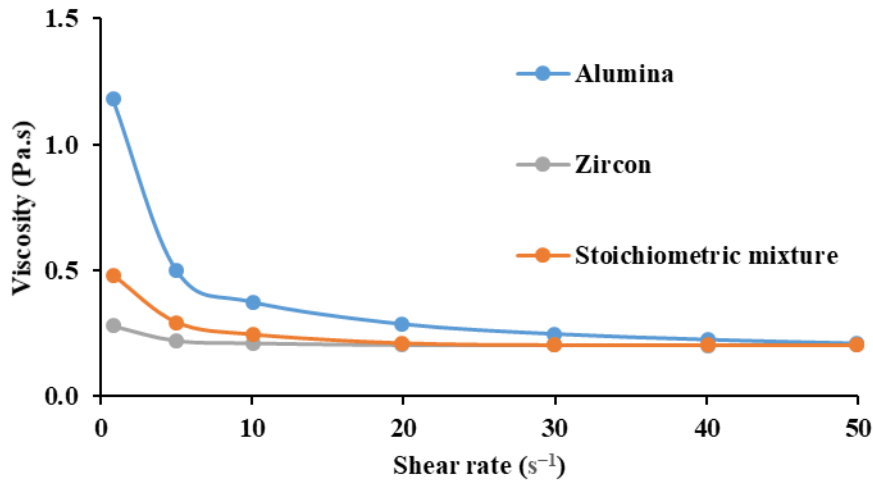
Source: Adapted from an article resulting from this thesis [47].

4.4.2 Slurry rheological Behavior and Stability

Figure 73 shows the viscosity curves of the prepared slurries. All the suspensions show similar viscosity in the operation range of the process (shear rate above 30 s^{-1} [24,142]), which is associated with the similar particle size of the powders. The low viscosity of the ceramic suspensions ($<0.25 \text{ Pa}\cdot\text{s}$) is favorable to the formation of uniform micrometric layers [28]. Also, their moderate shear-thinning behavior (decreased viscosity with increased shear rate) is desirable to avoid the sedimentation of the suspension at rest and allows adequate flow when a shear rate is applied [24,78]. Differences in the rheological behavior of suspensions may be associated with the geometry of the ceramic powders used.

Moreover, the prepared ceramic suspensions presented negligible sedimentation during the 30 days test with the retained volume fraction greater than 95%, indicating slurries suitable for the considered AM process.

Figure 73 – Viscosity curves of the prepared ceramic suspensions made of alumina, zircon, and the stoichiometric mixture.

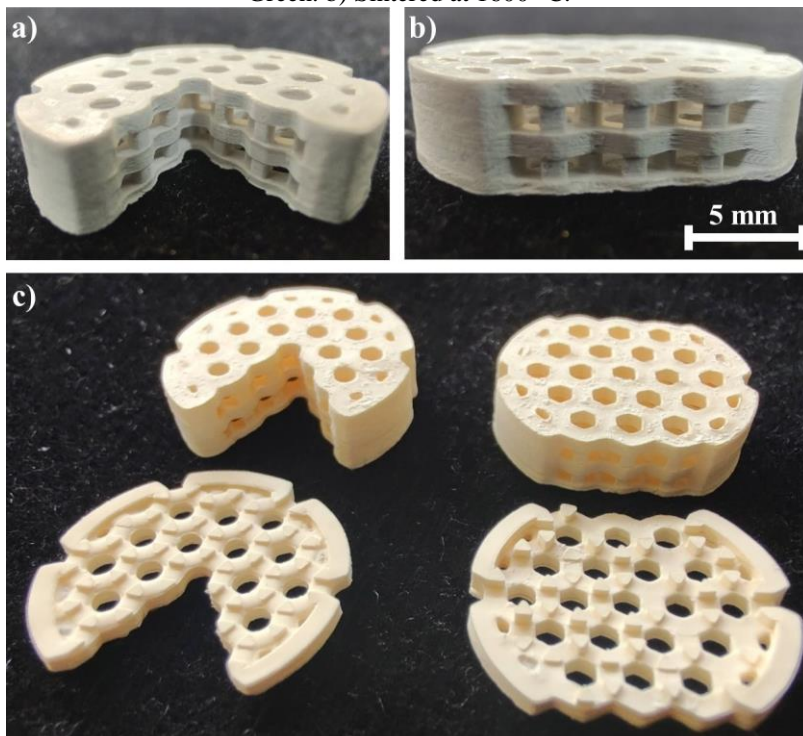


Source: Adapted from an article resulting from this thesis [47].

4.4.3 3D printing

Figure 74 shows printed parts, indicating the ability to manufacture parts with detailed and tiny structures, which would be unfeasible or even impossible to be produced by other manufacturing processes.

Figure 74 – 3D printed parts made of a stoichiometric mixture of zircon and alumina with tiny structures. a) Green. b) Sintered at 1600 °C.

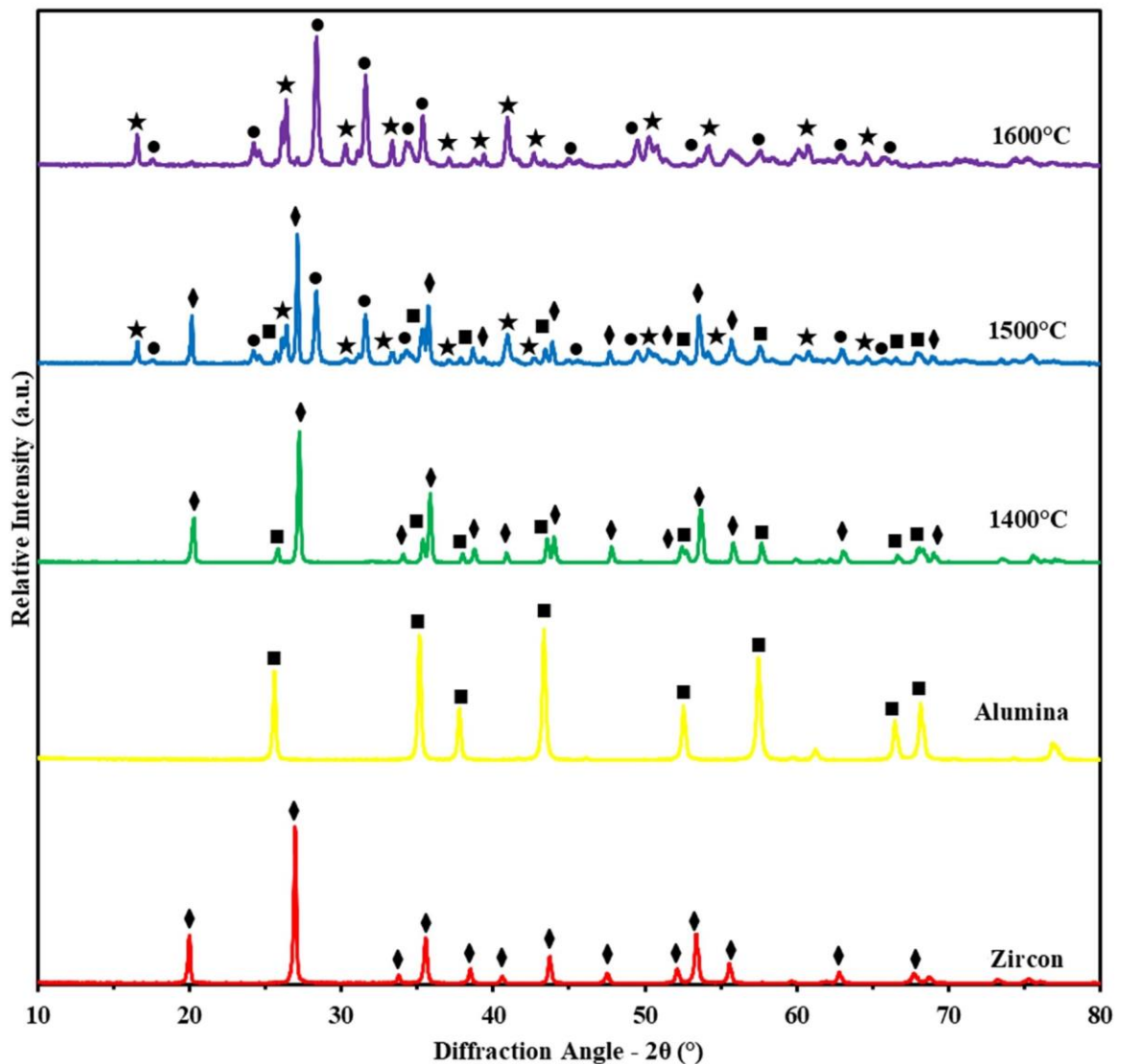


Source: Adapted from an article resulting from this thesis [47].

4.4.4 Reaction Sintering

Figure 75 shows X-ray diffraction patterns for the initial powders and parts sintered at different temperatures. No significant crystallinity change occurred at parts sintered at 1400 °C. On the other hand, the parts sintered at 1500 °C present not only the initial phases, but also mullite formed in situ and dissociated monoclinic zirconia. Finally, the reaction is completed at 1600 °C, creating mullite-zirconia composites.

Figure 75 – X-ray diffraction patterns for the alumina and zircon raw materials and parts sintered at different temperatures made of a stoichiometric mixture of zircon and alumina. Peaks of zircon are marked with \blacklozenge , alumina with \blacksquare , monoclinic Zirconia with \bullet , and mullite with \star .

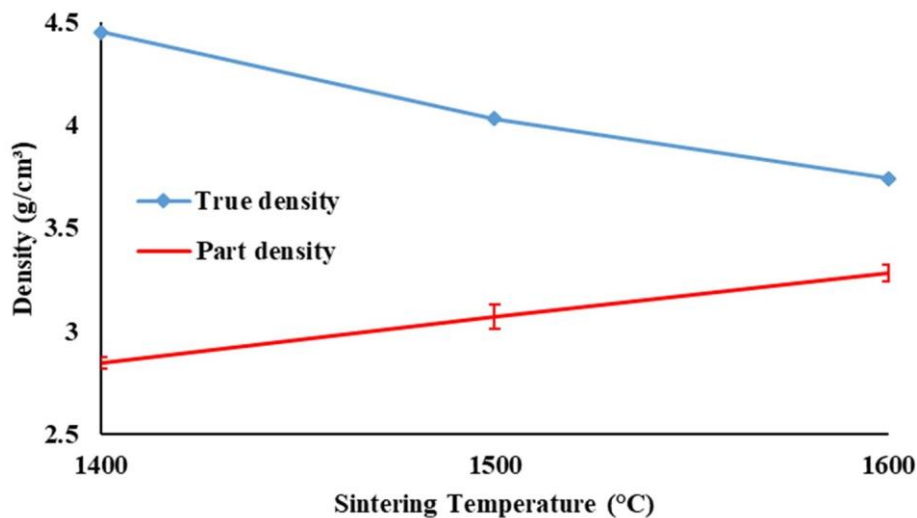


Source: Adapted from an article resulting from this thesis [47].

The reaction sintering is also evidenced in the density of the powders from parts sintered at different temperatures (Figure 76). The true density of parts sintered at 1400 °C is similar to

that of the initially mixed powders. The mullite and zirconia formation decreases the true density, and the powder density reached $3.740 \pm 0.004 \text{ g/cm}^3$ at $1600 \text{ }^\circ\text{C}$. On the other hand, the bulk density increases with increasing sintering temperature. Thus, the relative density increased from 64 ± 1 to $88 \pm 1 \%$ when the sintering temperature increased from $1400 \text{ }^\circ\text{C}$ to $1600 \text{ }^\circ\text{C}$. In addition, a summary of open and closed porosity is presented in Table 12, indicating that open porosity is predominant in the 3D printed parts sintered at all temperatures studied.

Figure 76 – Influence of sintering temperature on true density and bulk density of 3D printed parts made of a stoichiometric mixture of zircon and alumina.



Source: Adapted from an article resulting from this thesis [47].

Table 12 – Influence of sintering temperature on open and closed porosity of samples made of stoichiometric mixture of zircon and alumina.

Sintering Temperature (°C)	Open Porosity (%)	Closed Porosity (%)
1400	31 ± 1	4.9 ± 0.9
1500	19 ± 1	4.6 ± 0.8
1600	11 ± 1	1.4 ± 0.5

Source: Adapted from an article resulting from this thesis [47].

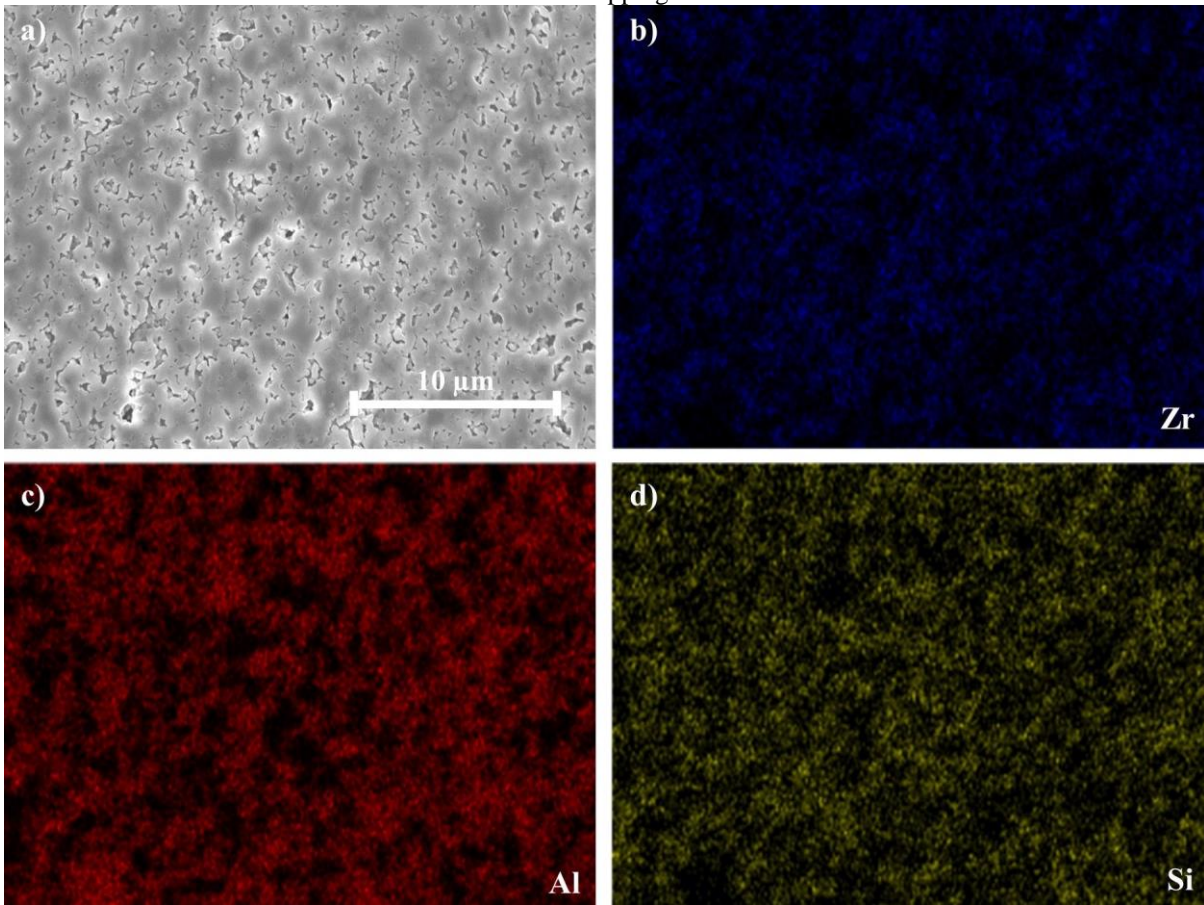
The flexural strength of the mullite-zirconia composites after the completed reaction sintering ($1600 \text{ }^\circ\text{C}$) reached $84 \pm 13 \text{ MPa}$. This value is significantly higher than the flexural strength presented by mullite parts (48 MPa) with alike relative density (86%) and manufactured under similar conditions [44]. On the other hand, research about mullite-zirconia composites produced by conventional ceramic processing has reported quite varied flexural

strength. For example, Aydin and Tokatas [281] reported a remarkable improvement in the flexural strength by using a sintering additive (colemantite), and the flexural strength improved from 52-94 MPa to 106-187 MPa (depending on the solid concentration and sintering temperature). Also, Lian et al. [282] obtained up to 285 MPa of flexural strength with mullite-zirconia composites. However, such a value was obtained for parts with open porosity smaller than 1%, being much denser than those reported in the present work.

Both relative density and flexural strength could be improved by increasing the solid loading of the suspension [66,76,78,283,284], which was limited, in this work, by the ordinary bottom-up 3D printer used. A higher ceramic loading would result in higher viscosity and demand a 3D printer specialized in ceramics [24]. Also, sintering additives have been used to improve densification in the fabrication of mullite-zirconia composites by conventional processes [281,285–288] and may be used in future developments of photosensitive suspensions to 3D print these materials.

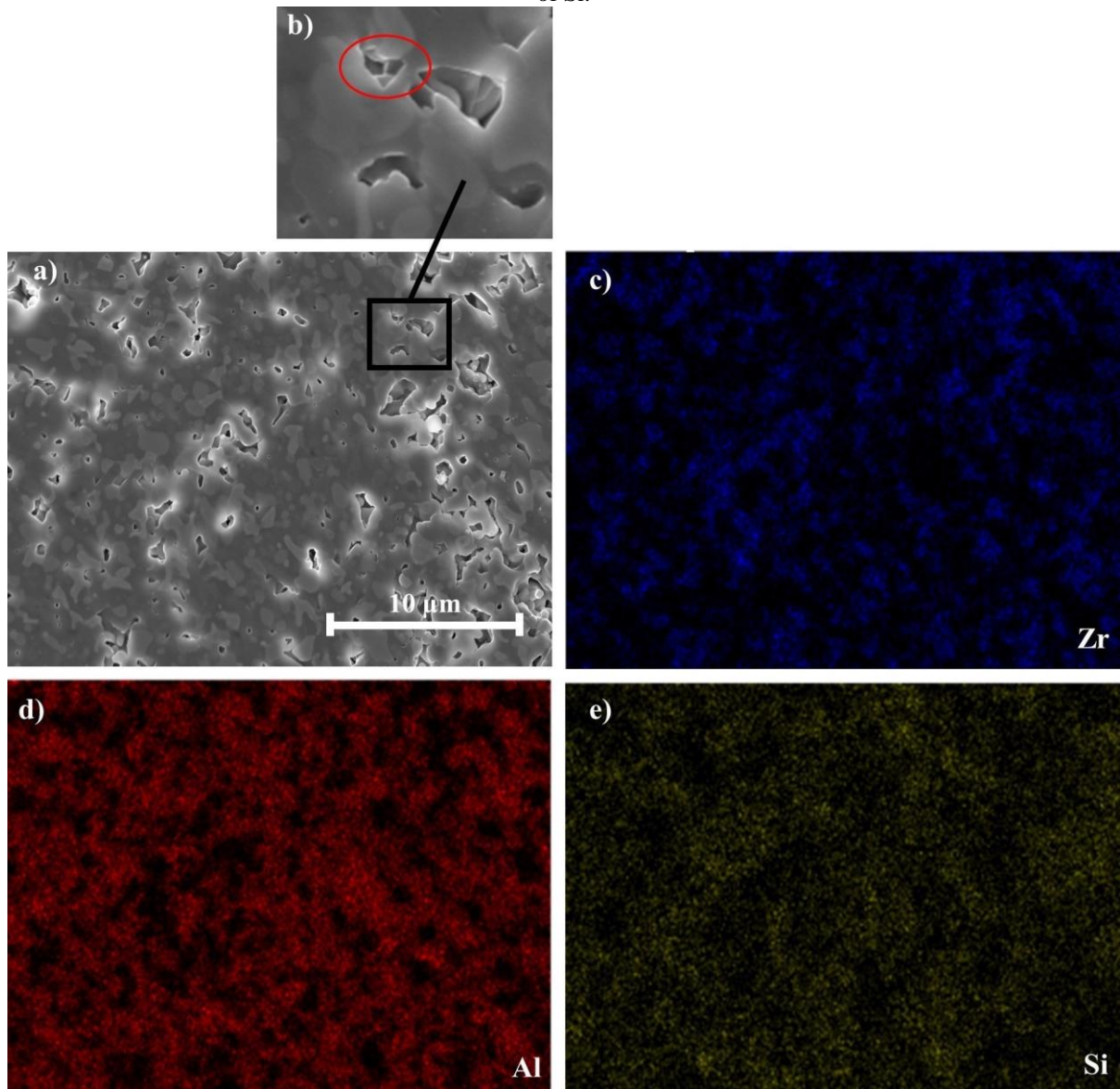
The SEM images with element mapping of parts sintered at different temperatures are shown from Figure 77 to Figure 79. The glassy phase plays an important role in the reaction sintering. The dissociation of zircon is already happening at 1500 °C (Figure 78), but the glass composition is not evident in the general EDS element mapping. However, a greater amount of impurities (Na and K) could be found in the boundaries of Zr-rich regions, as indicated in Figure 78b, suggesting the existence of a glassy phase in the area [289]. Finally, Figure 79 shows the microstructure for parts sintered at 1600 °C, in which the formation of in situ mullite and monoclinic zirconia was completed. The rounded morphology of the monoclinic zirconia corroborates the formation of the glassy phase around Zr-rich regions during the reaction sintering, as indicated in related work [281]. The formation of monoclinic rather than tetragonal zirconia was already expected since dopants were not added in this work.

Figure 77 – SEM-EDS elemental mapping of a sample made of a stoichiometric mixture of zircon and alumina sintered at 1400 °C. a) Scanning Electron Microscopy. b) Element mapping of Zr. c) Element mapping of Al. d) Element mapping of Si.



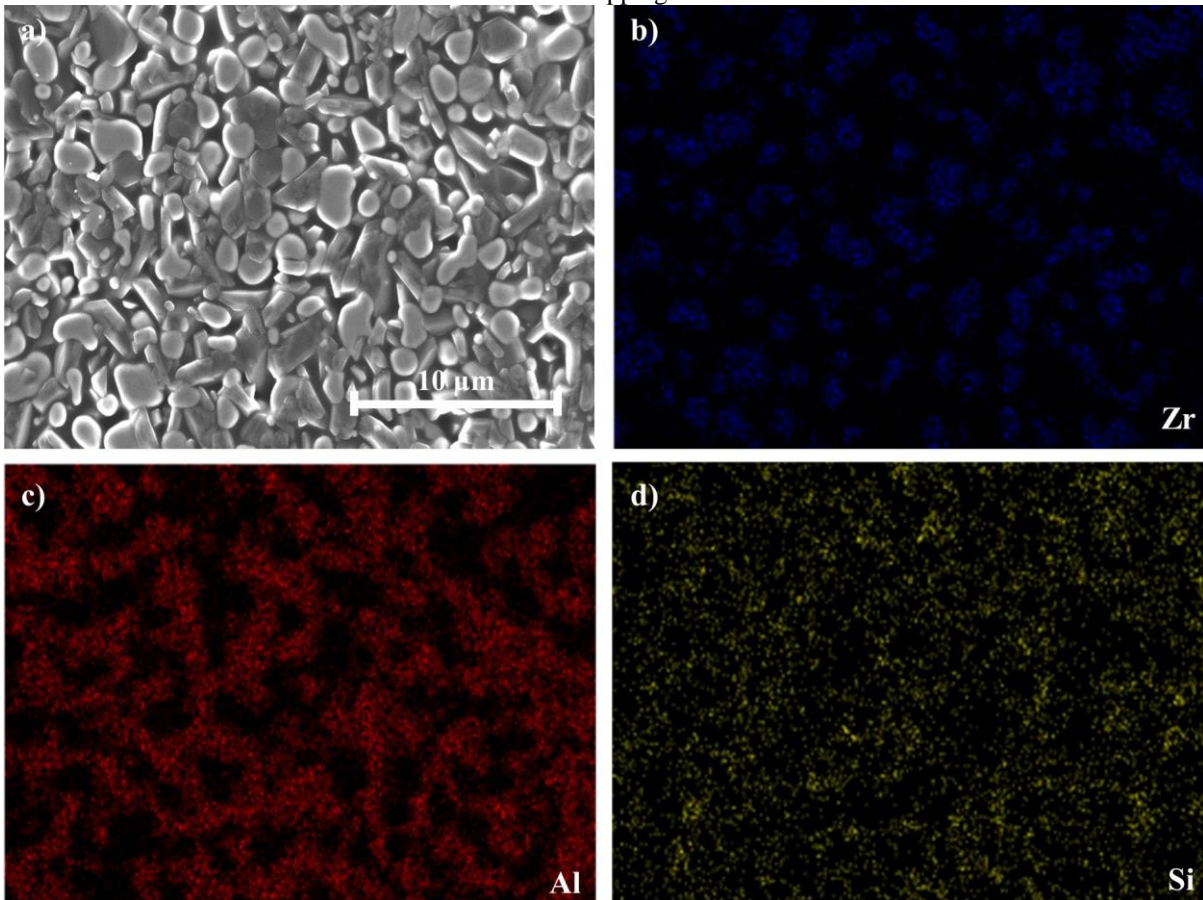
Source: Adapted from an article resulting from this thesis [47].

Figure 78 – SEM-EDS elemental mapping of a sample made of a stoichiometric mixture of zircon and alumina sintered at 1500 °C. a) Scanning Electron Microscopy (SEM). b) Magnified view of the SEM image with an indication of an impurity-rich region. c) Element mapping of Zr. d) Element mapping of Al. e) Element mapping of Si.



Source: Adapted from an article resulting from this thesis [47].

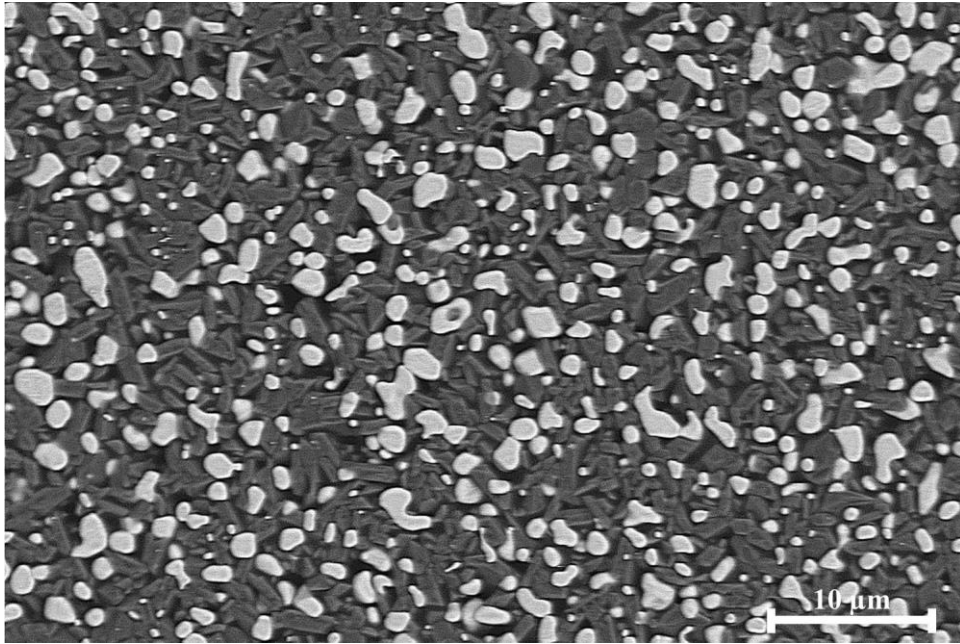
Figure 79 – SEM-EDS elemental mapping of a sample made of a stoichiometric mixture of zircon and alumina sintered at 1600 °C. a) Scanning Electron Microscopy. b) Element mapping of Zr. c) Element mapping of Al. d) Element mapping of Si.



Source: Adapted from an article resulting from this thesis [47].

In situ formation of mullite and zirconia can also be evidenced by SEM analysis with a backscattered electron detector (BSD). SEM-BSD images show high sensitivity to differences in atomic number. Higher atomic numbers generate a brighter appearance in the image [290]. Thus, Figure 80 presents the microstructure of a sample sintered at 1600 °C with the mullite grains being darker and the rounded shape zirconia grains being brighter due to the Zirconium chemical element having a higher atomic number ($Z=40$) than aluminum ($Z=13$) and Silicon ($Z=14$).

Figure 80 – SEM-BSD image of a sample made of a stoichiometric mixture of zircon and alumina sintered at 1600 °C.



Source: Elaborated by the author.

4.5 Final considerations

This work is a proof of concept that advanced ceramics can be produced by vat photopolymerization using economical 3D printers. Ceramic parts were produced not only in the developed prototype but also in an ordinary commercial 3D printer that costs less than US\$500, enabling the dissemination of the technique. Thus, the additive manufacturing technology that allows the manufacture of tiny structures with excellent dimensional precision and good surface quality can be applied in the manufacture of ceramic materials without the need for high investments. In addition to the most direct applications (industry and health), this allows the artistic production of ceramic pieces to be integrated with digital fabrication originating from 3D models. For example, Figure 81 shows the 3D caricature of the author of this thesis made of mullite. The 3D modeling was done by the artist Raul Tabajara, and manufacturing was made with the 40 vol% mullite suspension in the commercial 3D printer and sintered at 1600 °C.

Figure 81 – 3D caricature of the author of this thesis made of mullite (3D model created by the artist Raul Tabajara, manufactured from the 40 vol% mullite suspension in the selected commercial 3D printer and sintered at 1600 °C)



Source: Elaborated by the author.

4.5.1 Summary of the best results obtained in this work

Table 13 summarizes the best results obtained with the photosensitive ceramic suspensions developed in this work. The nanometric powder provided suspensions with higher viscosity (>2 Pa.s) and, therefore, could only be processed using the top-down built prototype with a dedicated recoating system. On the other hand, the submicrometric powders allowed the development of lower viscosity suspensions, which could be used also in the ordinary commercial bottom-up printer. In addition, this type of powder allowed the development of suspensions with up to 50 vol%, which is close to the best presented in the state-of-the-art and produced mullite parts with flexural strength comparable to those obtained by conventional processes.

Table 13 – Summary of the best results obtained with the photosensitive ceramic suspensions developed in this work.

Ceramic raw material	Mean Particle Size (μm)	Solid Loading (vol%)	Viscosity at 30 s^{-1} (Pa.s)	Suitable for prototype	Suitable for commercial 3D printer	Mean relative density (%)	Flexural strength (MPa)
3Y-TZP	0.04	40	2.30	Yes	No	95.4	169 ± 74
		40	0.14	Yes	Yes	92.8	65 ± 5
Mullite	0.6	45	0.25	Yes	Yes	95.7	79 ± 6
		50	0.79	Yes	Yes	97.7	95 ± 5
Zircon + Alumina	0.8	40	0.20	Yes	Yes	88.0	84 ± 13

Source: Elaborated by the author.

4.5.2 General guideline for future developments in ceramic vat photopolymerization.

Successful ceramic manufacturing by vat photopolymerization depends on several factors and the feedstock requirements will depend on the 3D printer to be used. A general guideline based on the experiences of this work for future developments related to vat photopolymerization of ceramic materials is presented next:

- Select a monomer (or a mixture of them) based on the literature. Viscosity and functionality must be considered, and the review article [24] resulting from this thesis may be useful.
- Select a photoinitiator whose absorbance spectrum is compatible with the light source of the 3D printer to be used. For detailed information on the most used photoinitiators for ceramic vat photopolymerization, see subsection 2.6.3.1.
- Select a suitable dispersant. First, search the literature [24] for dispersants already used with materials similar to the suspension to be developed. Pick a few and compare them concerning rheological behavior (especially viscosity at a shear rate of 30 s^{-1}) and sedimentation. For that, prepare suspensions with a predefined solid loading (e.g., 40 vol%) and a fixed amount of the tested dispersants (e.g., 3 wt% of the ceramic powder mass).
- Determine the dispersant concentration. Once the monomer(s) and dispersant have been selected, prepare suspensions with a predefined solid loading (e.g., 40 vol%) and different amounts of dispersant (e.g., from 0 to 5 wt% of the ceramic powder mass). Then, compare their sedimentation and rheological behavior (especially viscosity at a shear rate of 30 s^{-1}).

- Determine the solid loading. Prepare suspensions increasing the solid loading using the optimized amount of dispersant and characterize their rheological behavior. In general, the highest possible ceramic loading is desired. However, the limits of the 3D printer to be used must be considered. If the equipment is not dedicated to ceramics, such limits may be discovered empirically.

- Set the process specifications. The main printing parameters for vat photopolymerization are thickness and the light exposure time per layer. Unless there is a specific reason, the thickness may be the equipment default. For defining the light exposure parameter, expose the suspension to different light times and measure the thickness of the created layers (see section 3.7). The light exposure selected must provide a cure slightly thicker than the selected layer thickness (1.10 and 1.35 times [3]).

- Prepare the 3D printer. In addition to the usual vat photopolymerization precautions such as leveling the building platform, using ceramic suspensions as feedstock may require additional steps to prevent printing failures. For example, sanding the building platform (with 180 grit sandpaper) may prevent failures related to part detachment from the platform [258].

- Define your debinding protocol. A piece of a 3D printed part should be subjected to thermogravimetric analysis to study its thermal decomposition. Temperature ranges with higher thermal decomposition should have reduced heating rates in the debinding protocol. See subsection 4.2.7 for a practical example of how to use a TGA curve to define post-processing.

- Analyze the geometry of the parts to be manufactured. First, ceramic vat photopolymerization has limitations regarding maximum wall thickness (see section 2.7). Also, bottom-up 3D printers tend to fail when manufacturing parts with large cross-sections (see subsection 4.3.7). Finally, the anisotropic shrinkage during the post-processing must be considered.

5 CONCLUSIONS

In this work, advanced ceramic parts were produced by DLP additive manufacturing using a designed top-down prototype and an ordinary bottom-up 3D printer. The process proved to be able to produce ceramic detailed and tiny structures, which would be unfeasible or even impossible to be produced by other manufacturing processes. Furthermore, some manufactured parts presented flexural strength similar to the ones obtained by conventional processes. It was found that there is a strong dependence between raw materials, slurry, and the 3D printer to be used. Thus, the main findings and limitations are presented in this conclusion.

For that, a top-down DLP 3D printer with an innovative recoating system was designed and built, and photosensitive ceramic suspensions were developed, aiming to test their compatibility with the 3D printers considered. After the additive manufacturing, the green ceramic parts were subjected to debinding under appropriate heating rates and sintering to successfully obtain parts made of zirconia, mullite, and in situ mullite-zirconia composites.

The prototype built proved to be more versatile, due to its ability to work with different suspensions. Its top-down approach with an innovative recoating system composed of two blades with distinct and sequential actions allows the formation of uniform micrometric layers with constant thickness even with viscous suspensions. On the other hand, this device was designed only for the manufacture of smaller parts, since its use requires that the vat is always full and thus a large volume of printing would imply a large amount of raw material needed to carry out experiments. Still, the prototype has lower productivity, which is mainly explained by the need for a long time of light emission for the formation of layers due to the use of a commercial light projector with a small portion of useful irradiance. These prototype disadvantages can be overcome by replacing the vat and the build platform depending on the part to be printed and using a dedicated UV light projector for the purpose.

Although the ordinary bottom-up 3D printer has a large printing volume, such equipment also has restrictions on the size of the printed parts. Large cross-sections increase the separation force between the newly cured layer and the bottom of the vat, which may cause printing failures. On the other hand, it is important to note that the ceramic vat photopolymerization is not suitable for the manufacturing of parts with large wall thickness, not even with the use of the costly 3D printers specialized in ceramic manufacturing. Such a problem is associated with the high amount of organic materials used in the feedstock that has to be eliminated during the debinding.

Furthermore, several photosensitive ceramic suspensions were developed in this work, pointing out suitable components (PEGDA 250 as monomer, BAPO as photoinitiator, and BYK 111 as dispersant) and creating slurries based on distinct groups of ceramics powders: nanometric powders (3Y-TZP), submicrometric powders (electrofused mullite), and a combination of a natural raw material (zircon) with alumina. The 3D printing tests of these slurries showed the following:

The nanometric 3Y-TZP powders generated suspensions with higher viscosity, which limited the solid loading to 40 vol%. Only the top-down DLP 3D printer prototype was able to process this slurry. Zirconia (3Y-TZP) parts sintered at 1600 °C presented a density of 95.4% and some of these parts exceeded 200 MPa in flexural strength.

The submicrometric mullite powder was able to generate suspensions with up to 50 vol% solid loading. All the suspensions could be successfully used in both pieces of equipment considered. The study of the additive manufacturing of mullite from electrofused powder showed that density and flexural strength increased with increased sintering temperature and solid loading. Mullite parts from slurry with 50 vol% of solid loading sintered at 1650 °C reached a relative density of 97.7% and flexural strength of 95.2 ± 5.0 MPa.

Also, in situ mullite-zirconia composites parts were produced from alumina-zircon photosensitive slurries. The reaction sintering was studied at different temperatures, and it was completed at 1600 °C, which is evidenced by the X-ray diffraction patterns, true density, and SEM images. The printed parts from 40 vol% solid loading suspensions and sintered at 1600 °C reached a relative density of 87.7 ± 0.9 % and a flexural strength of 84 ± 13 MPa.

Finally, it is believed that the present study contributes to a new niche within the ceramic manufacturing industry, making the technique accessible to laboratories and small ceramic manufacturers and presenting an alternative to the traditional commercial link between equipment and raw material that raises the price of both.

5.1 Suggestions for future works

The studies of the following topics concerning ceramic vat photopolymerization are recommended:

- Influence of components such as plasticizers and sintering additives on the properties of sintered parts.
- Precision of the ceramic parts produced in the built prototype and in a low-cost DLP printer.

- Influence of the solid loading on the maximum wall thickness.
- Optimization of debinding under different atmospheres.
- Optimization of slurry processing using other equipment (SpeedMixer, planetary ball mill, etc.).
- Optimization of the recoating system (material and geometry of the blades, working speed, etc.).
- Development to reduce the operator's exposure to resin when using the built prototype.
- Influence of building direction on the properties.
- Development of dedicated dispersants instead of the off-the-shelf ones currently used.

6 SCIENTIFIC PRODUCTION

6.1 Articles published in Journals

Camargo IL de, Erbereli R, Lovo JFP, Fortulan R, Fortulan CA. Digital light processing additive manufacturing of in situ mullite-zirconia composites. *J Eur Ceram Soc* 2022. <https://doi.org/10.1016/j.jeurceramsoc.2022.06.042>

Camargo IL de, Lovo JFP, Erbereli R, Bock E, Fortulan CA. Fabrication of ceramics using photosensitive slurries: A comparison between UV-casting replication and vat photopolymerization 3D printing. *Process Appl Ceram* 2022. <https://doi.org/10.2298/PAC2202153C>

Camargo IL de, Fortulan CA, Colorado HA. A review on the ceramic additive manufacturing technologies and availability of equipment and materials. *Ceramica* 2022. <https://doi.org/10.1590/0366-69132022683873331>

Camargo IL de, Morais MM, Fortulan CA, Branciforti MC. A review on the rheological behavior and formulations of ceramic suspensions for vat photopolymerization. *Ceram Int* 2021;47:11906–21. <https://doi.org/10.1016/j.ceramint.2021.01.031>.

Camargo IL de, Erbereli R, Taylor H, Fortulan CA. 3Y-TZP DLP additive manufacturing: solvent-free slurry development and characterization. *Mater Res* 2021;24:e20200457. <https://doi.org/10.1590/1980-5373-mr-2020-0457>.

Camargo IL de, Erbereli R, Fortulan CA. Additive manufacturing of electrofused mullite slurry by digital light processing. *J Eur Ceram Soc* 2021;41:7182–8. <https://doi.org/10.1016/j.jeurceramsoc.2021.07.005>.

Camargo IL De, Lovo JFP, Erbereli R, Coelho RT, Silva IB Da, Fortulan CA. An overview of laser engineered net shaping of ceramics. *Rev Mater* 2020;25. <https://doi.org/10.1590/s1517-707620200001.0916>.

Erbereli R, Camargo IL de, Morais MM, Fortulan CA. 3D printing of trabecular bone - mimetic structures by vat photopolymerization of bovine hydroxyapatite as a potential candidate for scaffolds. *J Brazilian Soc Mech Sci Eng* 2022;0. <https://doi.org/10.1007/s40430-022-03468-0>.

Lovo JFP, Camargo IL de, Erbereli R, Morais MM, Fortulan CA. Vat Photopolymerization Additive Manufacturing Resins: Analysis and Case Study. *Mater Res* 2020;23:e20200010. <https://doi.org/https://doi.org/10.1590/1980-5373-MR-2020-0010>.

6.2 Filed patent

Camargo IL de, Erbereli R, Lovo JFP, Fortulan CA. Sistema de recobrimento com lâminas de ação sequencial para manufatura aditiva por fotopolimerização em cuba. 2021. BR1020210215445.

6.3 Article published as book chapter

Camargo IL de, Erbereli R, Lovo JFP, Fortulan CA. DLP 3D Printer with innovative recoating system. Proc. 6th Brazilian Technol. Symp., Springer, Cham; 2021, p. 609–16. https://doi.org/10.1007/978-3-030-75680-2_67.

6.4 Conferences and fairs with presentation of work or lecture

65th Brazilian Ceramic Conference (2022).

45th International Conference on Advanced Ceramics and Composites (2021).

26th International Congress of Mechanical Engineering (2021).

11th Brazilian Congress on Manufacturing Engineering (2021).

Expotech Itaquá (2021).

10th Brazilian Congress on Manufacturing Engineering (2019).

6.5 Articles published in magazines

10 Most Important Additive Manufacturing Journals of 2022. All3DP. <https://all3dp.com/2/best-additive-manufacturing-journal/>

3D Printing Advanced Ceramics. All3DP. <https://all3dp.com/2/vat-photopolymerization-dlp-advanced-ceramics/>

REFERENCES

- [1] Jr. Callister WD, Rethwisch DG. *Materials Science and Engineering: An Introduction*. 9th ed. John Wiley & Sons; 2013.
- [2] Carter CB, Norton MG. *Ceramic Materials - Science and Engineering*. 2nd ed. Springer-Verlag New York; 2013. <https://doi.org/10.1007/978-1-4614-3523-5>.
- [3] Wei L, Zhang J, Yu F, Zhang W, Meng X, Yang N, et al. A novel fabrication of yttria-stabilized-zirconia dense electrolyte for solid oxide fuel cells by 3D printing technique. *Int J Hydrogen Energy* 2019;44:6182–91. <https://doi.org/10.1016/j.ijhydene.2019.01.071>.
- [4] Xing B, Cao C, Zhao W, Shen M, Wang C, Zhao Z. Dense 8 mol% yttria-stabilized zirconia electrolyte by DLP stereolithography. *J Eur Ceram Soc* 2020;40:1418–23. <https://doi.org/10.1016/j.jeurceramsoc.2019.09.045>.
- [5] Manicone PF, Rossi Iommetti P, Raffaelli L. An overview of zirconia ceramics: Basic properties and clinical applications. *J Dent* 2007;35:819–26. <https://doi.org/10.1016/j.jdent.2007.07.008>.
- [6] Dehurtevent M, Robberecht L, Thuault A, Deveaux E, Leriche A, Petit F, et al. Effect of build orientation on the manufacturing process and the properties of stereolithographic dental ceramics for crown frameworks. *J Prosthet Dent* 2021;125:453–61. <https://doi.org/10.1016/j.prosdent.2020.01.024>.
- [7] Dehurtevent M, Robberecht L, Hornez JC, Thuault A, Deveaux E, Béhin P. Stereolithography: A new method for processing dental ceramics by additive computer-aided manufacturing. *Dent Mater* 2017;33:477–85. <https://doi.org/10.1016/j.dental.2017.01.018>.
- [8] Zhang K, He R, Ding G, Feng C, Song W, Fang D. Digital light processing of 3Y-TZP strengthened ZrO₂ ceramics. *Mater Sci Eng A* 2020;774:138768. <https://doi.org/10.1016/j.msea.2019.138768>.
- [9] Schwentenwein M, Homa J. Additive manufacturing of dense alumina ceramics. *Int J Appl Ceram Technol* 2015;12:1–7. <https://doi.org/10.1111/ijac.12319>.
- [10] Galante R, Figueiredo-Pina CG, Serro AP. Additive manufacturing of ceramics for dental applications: A review. *Dent Mater* 2019;35:825–46. <https://doi.org/10.1016/j.dental.2019.02.026>.
- [11] Lakhdar Y, Tuck C, Binner J, Terry A, Goodridge R. Additive manufacturing of

- advanced ceramic materials. *Prog Mater Sci* 2021;116:100736. <https://doi.org/10.1016/j.pmatsci.2020.100736>.
- [12] Chen Z, Li Z, Li J, Liu C, Lao C, Fu Y, et al. 3D printing of ceramics: A review. *J Eur Ceram Soc* 2019;39:661–87. <https://doi.org/10.1016/j.jeurceramsoc.2018.11.013>.
- [13] Shahzad A, Lazoglu I. Direct ink writing (DIW) of structural and functional ceramics: Recent achievements and future challenges. *Compos Part B Eng* 2021;225:109249. <https://doi.org/10.1016/j.compositesb.2021.109249>.
- [14] Lian Q, Yang F, Xin H, Li D. Oxygen-controlled bottom-up mask-projection stereolithography for ceramic 3D printing. *Ceram Int* 2017;43:14956–61. <https://doi.org/10.1016/j.ceramint.2017.08.014>.
- [15] Santoliquido O, Colombo P, Ortona A. Additive Manufacturing of ceramic components by Digital Light Processing: A comparison between the “bottom-up” and the “top-down” approaches. *J Eur Ceram Soc* 2019;39:2140–8. <https://doi.org/10.1016/j.jeurceramsoc.2019.01.044>.
- [16] ISO IO for S. ISO/ASTM 52900:2015(en), Additive manufacturing — General principles — Terminology 2015.
- [17] Gibson I, Rosen D, Stucker B. Additive manufacturing technologies: 3D printing, rapid prototyping, and direct digital manufacturing. 2nd ed. New York: Springer Science; 2015. <https://doi.org/10.1007/978-1-4939-2113-3>.
- [18] Ahrens CH. Processos de AM por fotopolimerização em cuba. In: Volpato N, editor. *Manufatura Aditiva Tecnol. e Apl. da Impressão 3D*. 1st ed., Blucher; 2017, p. 129–44.
- [19] Deckers J, Vleugels J, Kruth JP. Additive manufacturing of ceramics: A review. *J Ceram Sci Technol* 2014;5:245–60. <https://doi.org/10.4416/JCST2014-00032>.
- [20] Camargo IL De, Lovo JFP, Erbereli R, Coelho RT, Silva IB Da, Fortulan CA. An overview of laser engineered net shaping of ceramics. *Rev Mater* 2020;25. <https://doi.org/10.1590/s1517-707620200001.0916>.
- [21] Pelz JS, Ku N, Meyers MA, Vargas-Gonzalez LR. Additive manufacturing of structural ceramics: a historical perspective. *J Mater Res Technol* 2021;15:670–95. <https://doi.org/10.1016/j.jmrt.2021.07.155>.
- [22] Travitzky N, Bonet A, Dermeik B, Fey T, Filbert-Demut I, Schlier L, et al. Additive manufacturing of ceramic-based materials. *Adv Eng Mater* 2014;16:729–54. <https://doi.org/10.1002/adem.201400097>.
- [23] Diptanshu, Miao G, Ma C. Vat photopolymerization 3D printing of ceramics: Effects of fine powder. *Manuf Lett* 2019;21:20–3. <https://doi.org/10.1016/j.mfglet.2019.07.001>.

- [24] Camargo IL de, Morais MM, Fortulan CA, Branciforti MC. A review on the rheological behavior and formulations of ceramic suspensions for vat photopolymerization. *Ceram Int* 2021;47:11906–21. <https://doi.org/10.1016/j.ceramint.2021.01.031>.
- [25] Komissarenko DA, Sokolov PS, Evstigneeva AD, Shmeleva IA, Dosovitsky AE. Rheological and curing behavior of acrylate-based suspensions for the DLP 3D printing of complex zirconia parts. *Materials (Basel)* 2018;11:2350. <https://doi.org/10.3390/ma11122350>.
- [26] Griffith ML, Halloran JW. Freeform fabrication of ceramics via stereolithography. *J Am Ceram Soc* 1996;79:2601.
- [27] Jang KJ, Kang JH, Fisher JG, Park SW. Effect of the volume fraction of zirconia suspensions on the microstructure and physical properties of products produced by additive manufacturing. *Dent Mater* 2019;35:e97–106. <https://doi.org/10.1016/j.dental.2019.02.001>.
- [28] Zhang K, He R, Xie C, Wang G, Ding G, Wang M, et al. Photosensitive ZrO₂ suspensions for stereolithography. *Ceram Int* 2019;45:12189–95. <https://doi.org/10.1016/j.ceramint.2019.03.123>.
- [29] Schwarzer E, Götz M, Markova D, Stafford D, Scheithauer U, Moritz T. Lithography-based ceramic manufacturing (LCM) – Viscosity and cleaning as two quality influencing steps in the process chain of printing green parts. *J Eur Ceram Soc* 2017;37:5329–38. <https://doi.org/10.1016/j.jeurceramsoc.2017.05.046>.
- [30] Ding G, He R, Zhang K, Xia M, Feng C, Fang D. Dispersion and stability of SiC ceramic slurry for stereolithography. *Ceram Int* 2020;46:4720–9. <https://doi.org/10.1016/j.ceramint.2019.10.203>.
- [31] Park HK, Shin M, Kim B, Park JW, Lee H. A visible light-curable yet visible wavelength-transparent resin for stereolithography 3D printing. *NPG Asia Mater* 2018;10:82–9. <https://doi.org/10.1038/s41427-018-0021-x>.
- [32] Gonzalez P, Schwarzer E, Scheithauer U, Kooijmans N, Moritz T. Additive Manufacturing of Functionally Graded Ceramic Materials by Stereolithography. *J Vis Exp* 2019:1–8. <https://doi.org/10.3791/57943>.
- [33] Johansson E, Lidström O, Johansson J, Lyckfeldt O, Adolfsson E. Influence of resin composition on the defect formation in alumina manufactured by stereolithography. *Materials (Basel)* 2017;10. <https://doi.org/10.3390/ma10020138>.
- [34] Azarmi F, Amiri A. Microstructural evolution during fabrication of alumina via laser stereolithography technique. *Ceram Int* 2019;45:271–8.

<https://doi.org/10.1016/j.ceramint.2018.09.163>.

- [35] Varghese G, Moral M, Castro-García M, López-lópez JJ, Marín-Rueda JR, Yagüe-Alcaraz V, et al. Fabrication and characterisation of ceramics via low-cost DLP 3D printing. *Bol La Soc Esp Ceram y Vidr* 2018;57:9–18. <https://doi.org/10.1016/j.bsecv.2017.09.004>.
- [36] Liu X, Zou B, Xing H, Huang C. The preparation of ZrO₂-Al₂O₃ composite ceramic by SLA-3D printing and sintering processing. *Ceram Int* 2020;46:937–44. <https://doi.org/10.1016/j.ceramint.2019.09.054>.
- [37] Wu Z, Liu W, Wu H, Huang R, He R, Jiang Q, et al. Research into the mechanical properties, sintering mechanism and microstructure evolution of Al₂O₃-ZrO₂ composites fabricated by a stereolithography-based 3D printing method. *Mater Chem Phys* 2018;207:1–10. <https://doi.org/10.1016/j.matchemphys.2017.12.021>.
- [38] AMARAL LB DO. MANUFATURA ADITIVA DE CERÂMICAS POR PROJEÇÃO: PROJETO DE MÁQUINA, FORMULAÇÃO DE SUSPENSÕES E PROCESSO. 2019.
- [39] do Amaral LB, Paschoa JLF, Magalhães DV, Foschini CR, Suchicital CTA, Fortulan CA. Preliminary studies on additive manufacturing of over 95% dense 3Y zirconia parts via digital imaging projection. *J Brazilian Soc Mech Sci Eng* 2020;42:1–8. <https://doi.org/10.1007/s40430-019-2157-1>.
- [40] Camargo IL de, Erbereli R, Lovo JFP, Fortulan CA. DLP 3D Printer with innovative recoating system. *Proc. 6th Brazilian Technol. Symp., Springer, Cham; 2021, p. 609–16*. https://doi.org/10.1007/978-3-030-75680-2_67.
- [41] Camargo IL de, Erbereli R, Lovo JFP, Fortulan CA. DLP Additive Manufacturing of Ceramics : Photosensitive Parameters , Thermal Analysis , Post-Processing , and Parts Characterization. 11th Brazilian Congr. Manuf. Eng., 2021. <https://doi.org/10.26678/ABCM.COBEP2021.COB21-0106>.
- [42] Camargo IL de, Silveira Z de C, Erbereli R, Lovo JFP, Fortulan C. Design Development of a Ceramic DLP 3D Printer Integrating QFD and TRIZ. 26th Int. Congr. Mech. Eng., 2021. <https://doi.org/10.26678/abcm.cobem2021.cob2021-1086>.
- [43] Camargo IL de, Erbereli R, Taylor H, Fortulan CA. 3Y-TZP DLP additive manufacturing: solvent-free slurry development and characterization. *Mater Res* 2021;24:e20200457. <https://doi.org/10.1590/1980-5373-mr-2020-0457>.
- [44] Camargo IL de, Erbereli R, Fortulan CA. Additive manufacturing of electrofused mullite slurry by digital light processing. *J Eur Ceram Soc* 2021;41:7182–8. <https://doi.org/10.1016/j.jeurceramsoc.2021.07.005>.

- [45] Camargo IL de, Fortulan CA, Colorado HA. A review on the ceramic additive manufacturing technologies and availability of equipment and materials. *Cerâmica* 2022;68:329–47. <https://doi.org/10.1590/0366-69132022683873331>.
- [46] de Camargo I, Lovo JFP, Erbereli R, Bock E, Fortulan C. Fabrication of ceramics using photosensitive slurries: A comparison between UV-casting replication and vat photopolymerization 3D printing. *Process Appl Ceram* 2022;16:153–9. <https://doi.org/10.2298/PAC2202153C>.
- [47] de Camargo IL, Erbereli R, Lovo JFP, Fortulan R, Fortulan CA. Digital light processing additive manufacturing of in situ mullite-zirconia composites. *J Eur Ceram Soc* 2022;42:6025–32. <https://doi.org/10.1016/j.jeurceramsoc.2022.06.042>.
- [48] Ngo TD, Kashani A, Imbalzano G, Nguyen KTQ, Hui D. Additive manufacturing (3D printing): A review of materials, methods, applications and challenges. *Compos Part B Eng* 2018;143:172–96. <https://doi.org/10.1016/j.compositesb.2018.02.012>.
- [49] Revelo C, Colorado H. 3D printing of kaolinite clay with small additions of lime, fly ash and talc ceramic powders. *Process Appl Ceram* 2019;13:287–99. <https://doi.org/10.2298/PAC1903287R>.
- [50] Sachs E, Cima M, Williams P, Brancazio D, Cornie J. Three Dimensional Printing: Rapid Tooling and Prototypes Directly from a CAD Model. *J Eng Ind* 1992;114:481–8. <https://doi.org/10.1115/1.2900701>.
- [51] Agarwala MK, Weeren R Van, Bandyopadhyay A, Safari A, Danforth SC, Priedeman WR. Filament Feed Materials for Fused Deposition Processing of Ceramics and Metals. *Proc. Solid Free. Fabr. Symp.*, 1996, p. 451–8.
- [52] Danforth S. Fused Deposition of Ceramics: A New Technique for the Rapid Fabrication of Ceramic Components. *Mater Technol* 1995;10:144–6. <https://doi.org/10.1080/10667857.1995.11752614>.
- [53] Blazdell PF, Evans JRG, Edirisinghe MJ, Shaw P, Binstead MJ. The computer aided manufacture of ceramics using multilayer jet printing. *J Mater Sci Lett* 1995;14:1562–5. <https://doi.org/10.1007/BF00455415>.
- [54] Lakshminarayan U, Ogrydziak S, Marcus HL. Selective Laser Sintering of Ceramic Materials. *Int. Solid Free. Fabr. Symp.*, 1990, p. 16–26.
- [55] Griffith ML, Halloran JW. Ultraviolet Curing of Highly Loaded Ceramic Suspensions for Stereolithography of Ceramics. *Solid Free. Fabr. Symp.*, 1994, p. 396–403.
- [56] Zhang X, Wu X, Shi J. Additive manufacturing of zirconia ceramics: a state-of-the-art review. *J Mater Res Technol* 2020;9:9029–48.

<https://doi.org/10.1016/j.jmrt.2020.05.131>.

- [57] Kodama H. Automatic method for fabricating a three-dimensional plastic model with photo-hardening polymer. *Rev Sci Instrum* 1981;52:1770–3. <https://doi.org/10.1063/1.1136492>.
- [58] Hull CW. Apparatus for production of three-dimensional objects by stereolithography (US4575330), 1986.
- [59] Bartolo PJ, Gibson I. History of stereolithographic processes. In: Bartolo PJ, editor. *Stereolithography - Mater. Process. Appl.* 1st ed., Springer US; 2011, p. 37–56.
- [60] Wohlers T, Gornet T. *Wohlers Report 2016 - 3D printing and Additive Manufacturing of the Industry*. Wohlers Associates; 2016.
- [61] Bertsch A, Renaud P. Microstereolithography. In: Baldacchini T, editor. *Three Dimens. Fabr. using Two-phot. polymerization*, Elsevier; 2015, p. 20–44.
- [62] Hinczewski C, Corbel S, Chartier T. Ceramic suspensions suitable for stereolithography. *J Eur Ceram Soc* 1998;18:583–90. [https://doi.org/10.1016/s0955-2219\(97\)00186-6](https://doi.org/10.1016/s0955-2219(97)00186-6).
- [63] Hinczewski C, Corbel S, Chartier T. Stereolithography for the fabrication of ceramic 3D parts. *Rapid Prototyp J* 1998;4:104–11.
- [64] Xing H, Zou B, Lai Q, Huang C, Chen Q, Fu X, et al. Preparation and characterization of UV curable Al₂O₃ suspensions applying for stereolithography 3D printing ceramic microcomponent. *Powder Technol* 2018;338:153–61. <https://doi.org/10.1016/j.powtec.2018.07.023>.
- [65] Xing H, Zou B, Liu X, Wang X, Chen Q, Fu X, et al. Effect of particle size distribution on the preparation of ZTA ceramic paste applying for stereolithography 3D printing. *Powder Technol* 2020;359:314–22. <https://doi.org/10.1016/j.powtec.2019.09.066>.
- [66] Borlaf M, Szubra N, Serra-Capdevila A, Kubiak WW, Graule T. Fabrication of ZrO₂ and ATZ materials via UV-LCM-DLP additive manufacturing technology. *J Eur Ceram Soc* 2020;40:1574–81. <https://doi.org/10.1016/j.jeurceramsoc.2019.11.037>.
- [67] Lee JM, Sing SL, Zhou M, Yeong WY. 3D bioprinting processes: A perspective on classification and terminology. *Int J Bioprinting* 2018;4. <https://doi.org/10.18063/ijb.v4i2.151>.
- [68] Venuvinod PK, Ma W. *Rapid prototyping. Laser-based and Other Technologies*. vol. 23. Springer US; 2004. <https://doi.org/10.1007/978-1-4757-6361-4>.
- [69] Emami MM, Barazandeh F, Yaghmaie F. Scanning-projection based stereolithography: Method and structure. *Sensors Actuators, A Phys* 2014;218:116–24. <https://doi.org/10.1016/j.sna.2014.08.002>.

- [70] Lovo JFP, Camargo IL de, Erbereli R, Morais MM, Fortulan CA. Vat Photopolymerization Additive Manufacturing Resins : Analysis and Case Study. *Mater Res* 2020;23:e20200010. <https://doi.org/https://doi.org/10.1590/1980-5373-MR-2020-0010>.
- [71] Dumene R, Earle G, Williams C. Characterization of additively manufactured cellular alumina dielectric structures. *IEEE Trans Dielectr Electr Insul* 2018;25:2236–40. <https://doi.org/10.1109/TDEI.2018.007444>.
- [72] Zanchetta E, Cattaldo M, Franchin G, Schwentenwein M, Homa J, Brusatin G, et al. Stereolithography of SiOC Ceramic Microcomponents. *Adv Mater* 2016;28:370–6. <https://doi.org/10.1002/adma.201503470>.
- [73] Xiao J, Jia Y, Liu D, Cheng H. Three-dimensional printing of SiCN ceramic matrix composites from preceramic polysilazane by digital light processing. *Ceram Int* 2020;46:25802–7. <https://doi.org/10.1016/j.ceramint.2020.07.061>.
- [74] Wang JC, Dommati H, Hsieh SJ. Review of additive manufacturing methods for high-performance ceramic materials. *Int J Adv Manuf Technol* 2019;103:2627–47. <https://doi.org/10.1007/s00170-019-03669-3>.
- [75] Scheithauer U, Schwarzer E, Moritz T, Michaelis A. Additive Manufacturing of Ceramic Heat Exchanger: Opportunities and Limits of the Lithography-Based Ceramic Manufacturing (LCM). *J Mater Eng Perform* 2018;27:14–20. <https://doi.org/10.1007/s11665-017-2843-z>.
- [76] Xing H, Zou B, Li S, Fu X. Study on surface quality, precision and mechanical properties of 3D printed ZrO₂ ceramic components by laser scanning stereolithography. *Ceram Int* 2017;43:16340–7. <https://doi.org/10.1016/j.ceramint.2017.09.007>.
- [77] Sobhani S, Allan S, Muhunthan P, Boigne E, Ihme M. Additive Manufacturing of Tailored Macroporous Ceramic Structures for High-Temperature Applications. *Adv Eng Mater* 2020;22:2000158. <https://doi.org/10.1002/adem.202000158>.
- [78] Borlaf M, Serra-Capdevila A, Colominas C, Graule T. Development of UV-curable ZrO₂ slurries for additive manufacturing (LCM-DLP) technology. *J Eur Ceram Soc* 2019;39:3797–803. <https://doi.org/10.1016/j.jeurceramsoc.2019.05.023>.
- [79] Truxova V, Safka J, Seidl M, Kovalenko I, Volesky L, Ackermann M. Ceramic 3d printing: Comparison of SLA and DLP technologies. *MM Sci J* 2020;2020:3905–11. https://doi.org/10.17973/MMSJ.2020_06_2020006.
- [80] Wang D, Chen T, Zeng Y, Chen X, Xing W, Fan Y, et al. Optimization of UV-curable alumina suspension for digital light processing of ceramic membranes. *J Memb Sci*

- 2022;643:120066. <https://doi.org/10.1016/j.memsci.2021.120066>.
- [81] Chen T, Wang D, Chen X, Qiu M, Fan Y. Three-dimensional printing of high-flux ceramic membranes with an asymmetric structure via digital light processing. *Ceram Int* 2022;48:304–12. <https://doi.org/10.1016/j.ceramint.2021.09.105>.
- [82] Ye Y, Du Y, Hu T, You J, Bao B, Wang Y, et al. 3D Printing of Integrated Ceramic Membranes by the DLP Method. *Ind Eng Chem Res* 2021;60:9368–77. <https://doi.org/10.1021/acs.iecr.1c02224>.
- [83] Ray SS, Dommati H, Wang J-C, Chen S-S. Solvent based Slurry Stereolithography 3D printed hydrophilic ceramic membrane for ultrafiltration application. *Ceram Int* 2020;46:12480–8. <https://doi.org/10.1016/j.ceramint.2020.02.010>.
- [84] Pfaffinger M, Hartmann M, Schwentenwein M, Stampfl J. Stabilization of tricalcium phosphate slurries against sedimentation for stereolithographic additive manufacturing and influence on the final mechanical properties. *Int J Appl Ceram Technol* 2017;14:499–506. <https://doi.org/10.1111/ijac.12664>.
- [85] Erbereli R, de Camargo IL, Morais MM, Fortulan CA. 3D printing of trabecular bone-mimetic structures by vat photopolymerization of bovine hydroxyapatite as a potential candidate for scaffolds. *J Brazilian Soc Mech Sci Eng* 2022;44:170. <https://doi.org/10.1007/s40430-022-03468-0>.
- [86] Van hede D, Liang B, Anania S, Barzegari M, Verlée B, Nolens G, et al. 3D-Printed Synthetic Hydroxyapatite Scaffold With In Silico Optimized Macrostructure Enhances Bone Formation In Vivo. *Adv Funct Mater* 2022;32:2105002. <https://doi.org/10.1002/adfm.202105002>.
- [87] Liang H, Wang Y, Chen S, Liu Y, Liu Z, Bai J. Nano-Hydroxyapatite Bone Scaffolds with Different Porous Structures Processed by Digital Light Processing 3D Printing. *Int J Bioprinting* 2022;8:502. <https://doi.org/10.18063/ijb.v8i1.502>.
- [88] Zakeri S, Vastamäki T, Honkanen M, Järveläinen M, Vippola M, Levänen E. Fabrication of self-supporting structures made of washcoat materials (Al₂O₃-CeO₂) by ceramic stereolithography: Towards digital manufacturing of enhanced catalytic converters. *Mater Des* 2021;210:110115. <https://doi.org/10.1016/j.matdes.2021.110115>.
- [89] Santoliquido O, Camerota F, Pelanconi M, Ferri D, Elsener M, Dimopoulos Eggenschwiler P, et al. Structured Alumina Substrates for Environmental Catalysis Produced by Stereolithography. *Appl Sci* 2021;11:8239. <https://doi.org/10.3390/app11178239>.
- [90] Wang H, Wang P, Wang Q, Zhang R, Zhang L. Preparation of a High-Precision Gama-

- Al₂O₃ Structured Catalyst by DLP 3D Direct Printing for Hydrogen Production from Methanol. *Ind Eng Chem Res* 2021;60:13107–14. <https://doi.org/10.1021/acs.iecr.1c01951>.
- [91] Valotta A, Maier MC, Soritz S, Pauritsch M, Koenig M, Brouczek D, et al. 3D printed ceramics as solid supports for enzyme immobilization: an automated DoE approach for applications in continuous flow. *J Flow Chem* 2021;11:675–89. <https://doi.org/10.1007/s41981-021-00163-4>.
- [92] Nikulshin PA, Dorokhov VS, Ovsienko OL, Rogozina M V., Anikeev NA, Sidel'nikov I V., et al. Computer-Aided Modeling and Additive Manufacturing of Promising Protective Layer Materials for Catalytic Reactors. *Pet Chem* 2021;61:1207–16. <https://doi.org/10.1134/S0965544121110098>.
- [93] Li H, Liu Y, Colombo P, Li W, Liu Y, Hu K, et al. Enhanced 3D printed alumina ceramic cores via impregnation. *J Am Ceram Soc* 2022;105:181–92. <https://doi.org/10.1111/jace.18107>.
- [94] Li H, Liu Y, Liu Y, Zeng Q, Wang J, Hu K, et al. Evolution of the microstructure and mechanical properties of stereolithography formed alumina cores sintered in vacuum. *J Eur Ceram Soc* 2020;40:4825–36. <https://doi.org/10.1016/j.jeurceramsoc.2019.11.047>.
- [95] Li H, Liu Y, Liu Y, Zeng Q, Hu K, Lu Z, et al. Effect of sintering temperature in argon atmosphere on microstructure and properties of 3D printed alumina ceramic cores. *J Adv Ceram* 2020;9:220–31. <https://doi.org/10.1007/s40145-020-0362-0>.
- [96] Li H, Liu Y, Liu Y, Hu K, Lu Z, Liang J. Effects of Solvent Debinding on the Microstructure and Properties of 3D-Printed Alumina Ceramics. *ACS Omega* 2020;5:27455–62. <https://doi.org/10.1021/acsomega.0c03944>.
- [97] Li H, Liu Y, Liu Y, Zeng Q, Hu K, Lu Z, et al. Effect of burying sintering on the properties of ceramic cores via 3D printing. *J Manuf Process* 2020;57:380–8. <https://doi.org/10.1016/j.jmapro.2020.07.007>.
- [98] Jiang CP, Hsu HJ, Lee SY. Development of mask-less projection slurry stereolithography for the fabrication of zirconia dental coping. *Int J Precis Eng Manuf* 2014;15:2413–9. <https://doi.org/10.1007/s12541-014-0608-2>.
- [99] Wang W, Sun J. Dimensional accuracy and clinical adaptation of ceramic crowns fabricated with the stereolithography technique. *J Prosthet Dent* 2021;125:657–63. <https://doi.org/10.1016/j.prosdent.2020.02.032>.
- [100] Masciandaro S, Torrell M, Leone P, Tarancón A. Three-dimensional printed yttria-stabilized zirconia self-supported electrolytes for solid oxide fuel cell applications. *J Eur*

- Ceram Soc 2019;39:9–16. <https://doi.org/10.1016/j.jeurceramsoc.2017.11.033>.
- [101] Komissarenko DA, Sokolov PS, Evstigneeva AD, Slyusar I V., Nartov AS, Volkov PA, et al. DLP 3D printing of scandia-stabilized zirconia ceramics. *J Eur Ceram Soc* 2021;41:684–90. <https://doi.org/10.1016/j.jeurceramsoc.2020.09.010>.
- [102] Lin L, Wu H, Ni P, Chen Y, Huang Z, Li Y, et al. Additive manufacturing of complex-shaped and high-performance aluminum nitride-based components for thermal management. *Addit Manuf* 2022;52:102671. <https://doi.org/10.1016/j.addma.2022.102671>.
- [103] Duan W, Li S, Wang G, Dou R, Wang L, Zhang Y, et al. Thermal conductivities and mechanical properties of AlN ceramics fabricated by three dimensional printing. *J Eur Ceram Soc* 2020;40:3535–40. <https://doi.org/10.1016/j.jeurceramsoc.2020.04.004>.
- [104] Lin L, Wu H, Xu Y, Lin K, Zou W, Wu S. Fabrication of dense aluminum nitride ceramics via digital light processing-based stereolithography. *Mater Chem Phys* 2020;249:122969. <https://doi.org/10.1016/j.matchemphys.2020.122969>.
- [105] Zakeri S, Vippola M, Levänen E. A comprehensive review of the photopolymerization of ceramic resins used in stereolithography. *Addit Manuf* 2020;35:101177. <https://doi.org/10.1016/j.addma.2020.101177>.
- [106] Zhang J, Wei L, Meng X, Yu F, Yang N, Liu S. Digital light processing-stereolithography three-dimensional printing of yttria-stabilized zirconia. *Ceram Int* 2020;46:8745–53. <https://doi.org/10.1016/j.ceramint.2019.12.113>.
- [107] Li XB, Zhong H, Zhang JX, Duan Y Sen, Jiang DL. Powder Characteristics on the Rheological Performance of Resin-based Zirconia Suspension for Stereolithography. *J Inorg Mater* 2020;35:231–5. <https://doi.org/10.15541/jim20190091>.
- [108] Dudley K. 3D printing using spiral buildup and high viscosity build materials (US10150247B2) 2018. <https://doi.org/10.1038/incomms1464>.
- [109] Almquist TA, Hull CW, Modrek B, Serkuczewski AR, Jacobs PF, Lewis CW, et al. Recoating of stereolithographic layers (EP0361847B1), 1989.
- [110] Hafkamp T, Van Baars G, De Jager B, Etman P. A Trade-Off Analysis of Recoating Methods for Vat Photopolymerization of Ceramics. *Proc. 28th Annu. Int. Solid Free. Fabr. Symp.*, 2017, p. 687–711.
- [111] Chua, C.K, Leong KF, LIM CS. *Rapid Prototyping: Principles and Applications*. 3rd ed. World Scientific; 2010.
- [112] Allanic A-L, Schaeffer P. Fast three-dimensional modeling method and device (US6764636B1), 2000.

- [113] Saito N, Hayano S. High precision photosolidification modelling device (EP0484182A1), 1991.
- [114] Segawa T. Apparatus for shaping solid profile resin bodies (US5238497A), 1991. [https://doi.org/10.1016/0375-6505\(85\)90011-2](https://doi.org/10.1016/0375-6505(85)90011-2).
- [115] Hull CW, Cohen AL, Spence SL, Lewis CW. Apparatus and related method for forming a substantially flat stereolithographic working surface (US5447822A), 1994.
- [116] ALLANIC A-L, Medard C, Schaeffer J-P. Method and apparatus for making articles by photoprocessing a material (WO1995015842A1), 1994.
- [117] Almquist TA, Hull CW, Thayer JS, Leyden RN, Jacobs PF, Smalley DR. Reenduction rapide d'objets tridimensionnels formes sur une base de coupe transversale (WO1996023647A2), 1996.
- [118] Renap K, Vancraen W. Method and device for making a three-dimensional object from a hardenable liquid medium (EP0928242B1), 1997.
- [119] M. Gilio, J.P. Kruth, P. Vanherck. HIGH-SPEED CURTAIN RECOATING FOR STEREO LITHOGRAPHY. Proc. 12th Annu. Solid Free. Fabr. Symp., Austin, EUA: 2001, p. 46–54.
- [120] Almquist TA, Hull CW, Jacobs PF, Leyden RN, Smalley DR, Thayer JS. RAPID RECOATING OF THREE-DIMENSIONAL OBJECTS FORMED ON A CROSS-SECTIONAL BASIS (EP0807014B1), 1996.
- [121] KUIJPERS PAJM. Additive manufacturing system for manufacturing a three dimensional object (WO2015107066A1), 2015.
- [122] Nelson A, Getley S, Spalding D. Assessment of Technology for Additive Manufacturing of Ceramic Nuclear Fuels 2019.
- [123] Merot C, Graves A, Caltabiano V. Recoater blade reservoir and adjustment mechanism for stereolithography rapid-prototyping systems that allows removal and replacement of the blade-reservoir without adjustment to the blade height or rake settings (US20060219163A1), 2006.
- [124] Hunter DF, Reynolds GL, Wallstrom B. Improved rapid prototyping and manufacturing system and method (CN1974185B), 2006.
- [125] Yi Z. A kind of scraper adjusting method for photocurable rapid shaping (CN104457601B), 2014.
- [126] Bastiancich C, Danhier P, Pr at V, Danhier F. Anticancer drug-loaded hydrogels as drug delivery systems for the local treatment of glioblastoma. *J Control Release* 2016;243:29–42. <https://doi.org/10.1016/j.jconrel.2016.09.034>.

- [127] Goodner MD, Lee HR, Bowman CN. Method for Determining the Kinetic Parameters in Diffusion-Controlled Free-Radical Homopolymerizations. *Ind Eng Chem Res* 1997;36:1247–52. <https://doi.org/10.1021/ie9605387>.
- [128] Li K, Zhao Z. The effect of the surfactants on the formulation of UV-curable SLA alumina suspension. *Ceram Int* 2017;43:4761–7. <https://doi.org/10.1016/j.ceramint.2016.11.143>.
- [129] Adake C V., Bhargava P, Gandhi P. Effect of surfactant on dispersion of alumina in photopolymerizable monomers and their UV curing behavior for microstereolithography. *Ceram Int* 2015;41:5301–8. <https://doi.org/10.1016/j.ceramint.2014.12.066>.
- [130] Zhang S, Sha N, Zhao Z. Surface modification of α -Al₂O₃ with dicarboxylic acids for the preparation of UV-curable ceramic suspensions. *J Eur Ceram Soc* 2017;37:1607–16. <https://doi.org/10.1016/j.jeurceramsoc.2016.12.013>.
- [131] Sun J, Binner J, Bai J. Effect of surface treatment on the dispersion of nano zirconia particles in non-aqueous suspensions for stereolithography. *J Eur Ceram Soc* 2019;39:1660–7. <https://doi.org/10.1016/j.jeurceramsoc.2018.10.024>.
- [132] Wang Z, Huang C, Wang J, Zou B. Development of a novel aqueous hydroxyapatite suspension for stereolithography applied to bone tissue engineering. *Ceram Int* 2019;45:3902–9. <https://doi.org/10.1016/j.ceramint.2018.11.063>.
- [133] Xing Z, Liu W, Chen Y, Li W. Effect of plasticizer on the fabrication and properties of alumina ceramic by stereolithography-based additive manufacturing. *Ceram Int* 2018;44:19939–44. <https://doi.org/10.1016/j.ceramint.2018.07.259>.
- [134] Lee YH, Lee J Bin, Maeng WY, Koh YH, Kim HE. Photocurable ceramic slurry using solid camphor as novel diluent for conventional digital light processing (DLP) process. *J Eur Ceram Soc* 2019;39:4358–65. <https://doi.org/10.1016/j.jeurceramsoc.2019.05.069>.
- [135] Zeng Q, Yang C, Tang D, Li J, Feng Z, Liu J, et al. Additive manufacturing alumina components with lattice structures by digital light processing technique. *J Mater Sci Technol* 2019;35:2751–5. <https://doi.org/10.1016/j.jmst.2019.08.001>.
- [136] Chen W, Wang F, Yan K, Zhang Y, Wu D. Micro-stereolithography of KNN-based lead-free piezoceramics. *Ceram Int* 2019;45:4880–5. <https://doi.org/10.1016/j.ceramint.2018.11.185>.
- [137] Halloran JW. Ceramic Stereolithography: Additive Manufacturing for Ceramics by Photopolymerization. *Annu Rev Mater Res* 2016;46:19–40. <https://doi.org/10.1146/annurev-matsci-070115-031841>.

- [138] Schmidt J, Altun AA, Schwentenwein M, Colombo P. Complex mullite structures fabricated via digital light processing of a preceramic polysiloxane with active alumina fillers. *J Eur Ceram Soc* 2019;39:1336–43. <https://doi.org/10.1016/j.jeurceramsoc.2018.11.038>.
- [139] Hu K, Wei Y, Lu Z, Wan L, Li P. Design of a Shaping System for Stereolithography with High Solid Loading Ceramic Suspensions. *3D Print Addit Manuf* 2018;5:311–8. <https://doi.org/10.1089/3dp.2017.0065>.
- [140] Song SY, Park MS, Lee D, Lee JW, Yun JS. Optimization and characterization of high-viscosity ZrO₂ ceramic nanocomposite resins for supportless stereolithography. *Mater Des* 2019;180:107960. <https://doi.org/10.1016/j.matdes.2019.107960>.
- [141] Dufaud O, Marchal P, Corbel S. Rheological properties of PZT suspensions for stereolithography. *J Eur Ceram Soc* 2002;22:2081–92. [https://doi.org/10.1016/S0955-2219\(02\)00036-5](https://doi.org/10.1016/S0955-2219(02)00036-5).
- [142] Li X, Zhong H, Zhang J, Duan Y, Bai H, Li J, et al. Dispersion and properties of zirconia suspensions for stereolithography. *Int J Appl Ceram Technol* 2020;17:239–47. <https://doi.org/10.1111/ijac.13321>.
- [143] Chen Z, Li J, Liu C, Liu Y, Zhu J, Lao C. Preparation of high solid loading and low viscosity ceramic slurries for photopolymerization-based 3D printing. *Ceram Int* 2019;45:11549–57. <https://doi.org/10.1016/j.ceramint.2019.03.024>.
- [144] Tropea C, Yarin AL, Foss JF. *Springer Handbook of Experimental Fluid Mechanics*. Springer; 2007.
- [145] Wozniak M, de Hazan Y, Graule T, Kata D. Rheology of UV curable colloidal silica dispersions for rapid prototyping applications. *J Eur Ceram Soc* 2011;31:2221–9. <https://doi.org/10.1016/j.jeurceramsoc.2011.05.004>.
- [146] Wu X, Lian Q, Li D, He X, Meng J, Liu X, et al. Influence of boundary masks on dimensions and surface roughness using segmented exposure in ceramic 3D printing. *Ceram Int* 2019;45:3687–97. <https://doi.org/10.1016/j.ceramint.2018.11.031>.
- [147] Sokolov PS, Komissarenko DA, Dosovitskii GA, Shmeleva IA, Slyusar' I V., Dosovitskii AE. Rheological Properties of Zirconium Oxide Suspensions in Acrylate Monomers For Use In 3D Printing. *Glas Ceram (English Transl Steklo i Keramika)* 2018;75:55–9. <https://doi.org/10.1007/s10717-018-0028-3>.
- [148] Wang L, Liu X, Wang G, Tang W, Li S, Duan W, et al. Partially stabilized zirconia moulds fabricated by stereolithographic additive manufacturing via digital light processing. *Mater Sci Eng A* 2020;770:138537.

- <https://doi.org/10.1016/j.msea.2019.138537>.
- [149] Wang Y, Wang Z, Liu S, Qu Z, Han Z, Liu F, et al. Additive manufacturing of silica ceramics from aqueous acrylamide based suspension. *Ceram Int* 2019;45:21328–32. <https://doi.org/10.1016/j.ceramint.2019.07.118>.
- [150] Li Y, Wang M, Wu H, He F, Chen Y, Wu S. Cure behavior of colorful ZrO₂ suspensions during Digital light processing (DLP) based stereolithography process. *J Eur Ceram Soc* 2019;39:4921–7. <https://doi.org/10.1016/j.jeurceramsoc.2019.07.035>.
- [151] Wang W, Sun J, Guo B, Chen X, Ananth KP, Bai J. Fabrication of piezoelectric nanoceramics via stereolithography of low viscous and non-aqueous suspensions. *J Eur Ceram Soc* 2020;40:682–8. <https://doi.org/10.1016/j.jeurceramsoc.2019.10.033>.
- [152] Newstein MC, Wang H, Balsara NP, Lefebvre AA, Shnidman Y, Watanabe H, et al. Microstructural changes in a colloidal liquid in the shear thinning and shear thickening regimes. *J Chem Phys* 1999;111:4827–38. <https://doi.org/10.1063/1.479245>.
- [153] Wagner NJ, Brady JF. Shear thickening in colloidal dispersions. *Phys Today* 2009;62:27–32. <https://doi.org/10.1063/1.3248476>.
- [154] Lewis JA. Colloidal Processing of Ceramics. *J Am Ceram Soc* 2004;83:2341–59. <https://doi.org/10.1111/j.1151-2916.2000.tb01560.x>.
- [155] Hoffman RL. Discontinuous and Dilatant Viscosity Behavior in Concentrated Suspensions . I . Observation of a Flow Instability Discontinuous and Dilatant Viscosity Behavior in Concentrated Suspensions . I . Observation of a Flow Instability 1972;16:155–73. <https://doi.org/10.1122/1.549250>.
- [156] Li X, Zhong H, Zhang J, Duan Y, Li J, Jiang D. Fabrication of zirconia all-ceramic crown via DLP-based stereolithography. *Int J Appl Ceram Technol* 2020;17:844–53. <https://doi.org/10.1111/ijac.13441>.
- [157] Barnes HA, Hutton JFH, Waltersn K. An introduction to rheology. Amsterdam: Elsevier; 1989.
- [158] Goswami A, Ankit K, Balashanmugam N, Umarji AM, Madras G. Optimization of rheological properties of photopolymerizable alumina suspensions for ceramic microstereolithography. *Ceram Int* 2014;40:3655–65. <https://doi.org/10.1016/j.ceramint.2013.09.059>.
- [159] Bae CJ, Halloran JW. Concentrated suspension-based additive manufacturing – viscosity, packing density, and segregation. *J Eur Ceram Soc* 2019;39:4299–306. <https://doi.org/10.1016/j.jeurceramsoc.2019.05.034>.
- [160] Barnes HA. Shear-Thickening (“Dilatancy”) in Suspensions of Nonaggregating Solid

- Particles Dispersed in Newtonian Liquids. *J Rheol (N Y N Y)* 1989;33:329–66. <https://doi.org/10.1122/1.550017>.
- [161] He L, Song X. Supportability of a High-Yield-Stress Slurry in a New Stereolithography-Based Ceramic Fabrication Process. *Jom* 2018;70:407–12. <https://doi.org/10.1007/s11837-017-2657-3>.
- [162] Macosko CW. *Rheology: Principles, Measurements and Applications*. New York: Wiley-VCH; 1994.
- [163] Lasgorceix M, Champion E, Chartier T. Shaping by microstereolithography and sintering of macro-micro-porous silicon substituted hydroxyapatite. *J Eur Ceram Soc* 2016;36:1091–101. <https://doi.org/10.1016/j.jeurceramsoc.2015.11.020>.
- [164] Herschel WH, Bulkley R. Konsistenzmessungen von gummi-benzollosungen. *Kolloid Z* 1926;39:291. <https://doi.org/https://doi.org/10.1007/BF01432034>.
- [165] Yaghtin M, Yaghtin A, Tang Z, Troczynski T. Improving the rheological and stability characteristics of highly concentrated aqueous yttria stabilized zirconia slurries. *Ceram Int* 2020;46:26991–9. <https://doi.org/10.1016/j.ceramint.2020.07.176>.
- [166] Gao F, Yang S, Hao P, Evans JRG. Suspension stability and fractal patterns: A comparison using hydroxyapatite. *J Am Ceram Soc* 2011;94:704–12. <https://doi.org/10.1111/j.1551-2916.2010.04149.x>.
- [167] Wang L, Zheng K, Ding Z, Yan X, Zhang H, Cao Y, et al. Drag coefficient and settling velocity of fine particles with varying surface wettability. *Powder Technol* 2020;372:8–14. <https://doi.org/10.1016/j.powtec.2020.05.102>.
- [168] Richardson JF, Zaki WN. Sedimentation and fluidisation: Part I. *Trans Inst Chem Eng* 1954;32:35–53. [https://doi.org/10.1016/S0263-8762\(97\)80006-8](https://doi.org/10.1016/S0263-8762(97)80006-8).
- [169] Abel JS, Stangle GC, Schilling CH, Aksay IA. Sedimentation in flocculating colloidal suspensions. *J Mater Res* 1994;9:451–61. <https://doi.org/10.1557/JMR.1994.0451>.
- [170] Zhang K, Xie C, Wang G, He R, Ding G, Wang M, et al. High solid loading, low viscosity photosensitive Al₂O₃ slurry for stereolithography based additive manufacturing. *Ceram Int* 2019;45:203–8. <https://doi.org/10.1016/j.ceramint.2018.09.152>.
- [171] Burgos-Montes O, Moreno R. Stability of concentrated suspensions of Al₂O₃-SiO₂ measured by multiple light scattering. *J Eur Ceram Soc* 2009;29:603–10. <https://doi.org/10.1016/j.jeurceramsoc.2008.07.044>.
- [172] Rajaiiah J, Ruckenstein E, Andrews GF, Forster EO, Gupta RK. Rheology of Sterically Stabilized Ceramic Suspensions. *Ind Eng Chem Res* 1994;33:2336–40.

<https://doi.org/10.1021/ie00034a012>.

- [173] Krieger IM, Dougherty TJ. A Mechanism for Non-Newtonian Flow in Suspensions of Rigid Spheres. *Trans Soc Rheol* 1959;3:137–52. <https://doi.org/10.1122/1.548848>.
- [174] Zhang K, He R, Ding G, Bai X, Fang D. Effects of fine grains and sintering additives on stereolithography additive manufactured Al₂O₃ ceramic. *Ceram Int* 2020;47:2303–10. <https://doi.org/10.1016/j.ceramint.2020.09.071>.
- [175] Wang J. A Novel Fabrication Method of High Strength Alumina Ceramic Parts Based on Solvent-based Slurry Stereolithography and Sintering. *Int J Precis Eng Manuf* 2013;14:485–91. <https://doi.org/10.1007/s12541-013-0065-3>.
- [176] Liu W, Wu H, Tian Z, Li Y, Zhao Z, Huang M, et al. 3D printing of dense structural ceramic microcomponents with low cost: Tailoring the sintering kinetics and the microstructure evolution. *J Am Ceram Soc* 2019;102:2257–62. <https://doi.org/10.1111/jace.16241>.
- [177] He R, Liu W, Wu Z, An D, Huang M, Wu H, et al. Fabrication of complex-shaped zirconia ceramic parts via a DLP- stereolithography-based 3D printing method. *Ceram Int* 2018;44:3412–6. <https://doi.org/10.1016/j.ceramint.2017.11.135>.
- [178] Zhou M, Liu W, Wu H, Song X, Chen Y, Cheng L, et al. Preparation of a defect-free alumina cutting tool via additive manufacturing based on stereolithography – Optimization of the drying and debinding processes. *Ceram Int* 2016;42:11598–602. <https://doi.org/10.1016/j.ceramint.2016.04.050>.
- [179] Wu H, Liu W, He R, Wu Z, Jiang Q, Song X, et al. Fabrication of dense zirconia-toughened alumina ceramics through a stereolithography-based additive manufacturing. *Ceram Int* 2017;43:968–72. <https://doi.org/10.1016/j.ceramint.2016.10.027>.
- [180] Li W, Nie J, Li M, Liu W, Chen Y, Xing Z. Additive manufactured 3Y-TZP ceramics: Study of micromechanical behavior by nanoindentation and microscratch method. *Int J Appl Ceram Technol* 2019:1–10. <https://doi.org/10.1111/ijac.13459>.
- [181] Wu H, Cheng Y, Liu W, He R, Zhou M, Wu S, et al. Effect of the particle size and the debinding process on the density of alumina ceramics fabricated by 3D printing based on stereolithography. *Ceram Int* 2016;42:17290–4. <https://doi.org/10.1016/j.ceramint.2016.08.024>.
- [182] Greenwood R, Luckham PF, Gregory T. The effect of diameter ratio and volume ratio on the viscosity of bimodal suspensions of polymer latices. *J Colloid Interface Sci* 1997;191:11–21. <https://doi.org/10.1006/jcis.1997.4915>.
- [183] Olhero SM, Ferreira JMF. Influence of particle size distribution on rheology and particle

- packing of silica-based suspensions. *Powder Technol* 2004;139:69–75. <https://doi.org/10.1016/j.powtec.2003.10.004>.
- [184] Farris RJ. Prediction of the Viscosity of Multimodal Suspensions from Unimodal Viscosity Data. *Trans Soc Rheol* 1968;12:281–301. <https://doi.org/10.1122/1.549109>.
- [185] Tomeckova V, Halloran JW. Flow behavior of polymerizable ceramic suspensions as function of ceramic volume fraction and temperature. *J Eur Ceram Soc* 2011;31:2535–42. <https://doi.org/10.1016/j.jeurceramsoc.2011.01.019>.
- [186] Lian Q, Sui W, Wu X, Yang F, Yang S. Additive manufacturing of ZrO₂ ceramic dental bridges by stereolithography. *Rapid Prototyp J* 2018;24:114–9. <https://doi.org/10.1108/RPJ-09-2016-0144>.
- [187] Kotz F, Arnold K, Bauer W, Schild D, Keller N, Sachsenheimer K, et al. Three-dimensional printing of transparent fused silica glass. *Nature* 2017;544:337–9. <https://doi.org/10.1038/nature22061>.
- [188] Chen Z, Liu C, Li J, Zhu J, Liu Y, Lao C, et al. Mechanical properties and microstructures of 3D printed bulk cordierite parts. *Ceram Int* 2019;45:19257–67. <https://doi.org/10.1016/j.ceramint.2019.06.174>.
- [189] He R, Ding G, Zhang K, Li Y, Fang D. Fabrication of SiC ceramic architectures using stereolithography combined with precursor infiltration and pyrolysis. *Ceram Int* 2019;45:14006–14. <https://doi.org/10.1016/j.ceramint.2019.04.100>.
- [190] Bae CJ, Halloran JW. Influence of residual monomer on cracking in ceramics fabricated by stereolithography. *Int J Appl Ceram Technol* 2011;8:1289–95. <https://doi.org/10.1111/j.1744-7402.2010.02578.x>.
- [191] Tian Z, Yang Y, Wang Y, Wu H, Liu W, Wu S. Fabrication and properties of a high porosity h-BN–SiO₂ ceramics fabricated by stereolithography-based 3D printing. *Mater Lett* 2019;236:144–7. <https://doi.org/10.1016/j.matlet.2018.10.058>.
- [192] Chen Y, Bao X, Wong CM, Cheng J, Wu H, Song H, et al. PZT ceramics fabricated based on stereolithography for an ultrasound transducer array application. *Ceram Int* 2018;44:22725–30. <https://doi.org/10.1016/j.ceramint.2018.09.055>.
- [193] Zheng T, Wang W, Sun J, Liu J, Bai J. Development and evaluation of Al₂O₃–ZrO₂ composite processed by digital light 3D printing. *Ceram Int* 2020;46:8682–8. <https://doi.org/10.1016/j.ceramint.2019.12.102>.
- [194] Huang RJ, Jiang QG, Wu HD, Li YH, Liu WY, Lu XX, et al. Fabrication of complex shaped ceramic parts with surface-oxidized Si₃N₄ powder via digital light processing based stereolithography method. *Ceram Int* 2019;45:5158–62.

- <https://doi.org/10.1016/j.ceramint.2018.11.116>.
- [195] Wei Y, Zhao D, Cao Q, Wang J, Wu Y, Yuan B, et al. Stereolithography-Based Additive Manufacturing of High-Performance Osteoinductive Calcium Phosphate Ceramics by a Digital Light-Processing System. *ACS Biomater Sci Eng* 2020;6:1787–97. <https://doi.org/10.1021/acsbiomaterials.9b01663>.
- [196] Cha J, Lee JW, Bae B, Lee SE, Yoon CB. Fabrication and characterization of PZT suspensions for stereolithography based on 3D printing. *J Korean Ceram Soc* 2019;56:360–4. <https://doi.org/10.4191/kcers.2019.56.4.08>.
- [197] Chen F, Zhu H, Wu JM, Chen S, Cheng LJ, Shi YS, et al. Preparation and biological evaluation of ZrO₂ all-ceramic teeth by DLP technology. *Ceram Int* 2020;46:11268–74. <https://doi.org/10.1016/j.ceramint.2020.01.152>.
- [198] Schmidt J, Elsayed H, Bernardo E, Colombo P. Digital light processing of wollastonite-diopside glass-ceramic complex structures. *J Eur Ceram Soc* 2018;38:4580–4. <https://doi.org/10.1016/j.jeurceramsoc.2018.06.004>.
- [199] Wang JC, Dommati H. Fabrication of zirconia ceramic parts by using solvent-based slurry stereolithography and sintering. *Int J Adv Manuf Technol* 2018;98:1537–46. <https://doi.org/10.1007/s00170-018-2349-3>.
- [200] Liu JC, Jean JH, Li CC. Dispersion of nano-sized γ -alumina powder in non-polar solvents. *J Am Ceram Soc* 2006;89:882–7. <https://doi.org/10.1111/j.1551-2916.2005.00858.x>.
- [201] Conley RF. *Practical Dispersion. A Guide to Understanding and Formulation Slurries*. 1st ed. WILEY-VCH; 1996.
- [202] Liu D-M. Effect of Dispersants on the Rheological Behavior of Zirconia-Wax Suspensions. *J Am Ceram Soc* 2004;82:1162–8. <https://doi.org/10.1111/j.1151-2916.1999.tb01890.x>.
- [203] Tanurdjaja S, Tallon C, Scales PJ, Franks G V. Influence of dispersant size on rheology of non-aqueous ceramic particle suspensions. *Adv Powder Technol* 2011;22:476–81. <https://doi.org/10.1016/j.appt.2011.04.011>.
- [204] Tadros TF. *Rheology of Dispersions*. Weinheim, Germany: Wiley-VCH Verlag GmbH & Co. KGaA; 2010. <https://doi.org/10.1002/9783527631568>.
- [205] Sushumna I, Gupta RK, Ruckenstein E. Effective dispersants for concentrated, nonaqueous suspensions. *J Mater Res* 1992;7:2884–93. <https://doi.org/10.1557/JMR.1992.2884>.
- [206] Oliveira IR de, Studart AR, Pileggi RG, Pandolfelli VC. Dispersão e Empacotamento de

- Partículas - Princípios e Aplicações em Processamento Cerâmico. São Paulo: Fazenda Arte; 2000.
- [207] Davies J, Binner JGP. The role of ammonium polyacrylate in dispersing concentrated alumina suspensions. *J Eur Ceram Soc* 2000;20:1539–53. [https://doi.org/10.1016/S0955-2219\(00\)00012-1](https://doi.org/10.1016/S0955-2219(00)00012-1).
- [208] Castellan G. *Fundamentos de Físico-Química*. 1st ed. LTC; 1995.
- [209] Van Den Brand J, Blajiev O, Beentjes PCJ, Terryn H, De Wit JHW. Interaction of ester functional groups with aluminum oxide surfaces studied using infrared reflection absorption spectroscopy. *Langmuir* 2004;20:6318–26. <https://doi.org/10.1021/la049456a>.
- [210] Narkiewicz-Michałek J, Rudzinski W, Keh E, Partyka S. A combined calorimetric-thermodynamic study of non-ionic surfactant adsorption from aqueous solutions onto silica surface. *Colloids and Surfaces* 1992;62:273–88. [https://doi.org/10.1016/0166-6622\(92\)80053-5](https://doi.org/10.1016/0166-6622(92)80053-5).
- [211] Somasundaran P, Snell ED, Fu E, Xu Q. Effect of adsorption of non-ionic surfactant and non-ionic-anionic surfactant mixtures on silica-liquid interfacial properties. *Colloids and Surfaces* 1992;63:49–54. [https://doi.org/10.1016/0166-6622\(92\)80068-D](https://doi.org/10.1016/0166-6622(92)80068-D).
- [212] Li H, Liu YS, Liu YS, Zeng QF, Hu KH, Liang JJ, et al. Microstructure and properties of 3D-printed alumina ceramics with different heating rates in vacuum debinding. *Rare Met* 2020. <https://doi.org/10.1007/s12598-020-01372-x>.
- [213] Schofield JD. Extending the boundaries of dispersant technology. *Prog Org Coatings* 2002;45:249–57. [https://doi.org/10.1016/S0300-9440\(02\)00041-3](https://doi.org/10.1016/S0300-9440(02)00041-3).
- [214] Zeng Y, Yan Y, Yan H, Liu C, Li P, Dong P, et al. 3D printing of hydroxyapatite scaffolds with good mechanical and biocompatible properties by digital light processing. *J Mater Sci* 2018;53:6291–301. <https://doi.org/10.1007/s10853-018-1992-2>.
- [215] Bajpai P. *Chemicals Used in Deinking and Their Function*. *Recycl. Deinking Recover. Pap.*, Elsevier; 2014, p. 121–37. <https://doi.org/10.1016/C2013-0-00556-7>.
- [216] Wojcik AB, Klein LC. Transparent inorganic/organic copolymers by the sol-gel process: Thermal behavior of copolymers of tetraethyl orthosilicate (TEOS), vinyl triethoxysilane (VTES) and (meth)acrylate monomers. *J Sol-Gel Sci Technol* 1995;5:77–82. <https://doi.org/10.1007/BF00487723>.
- [217] Green WA. *Industrial Photoinitiators: A technical guide*. CRC Press - Taylor & Francis Group; 2010. <https://doi.org/10.1201/9781439827468>.
- [218] Dai Y, Qiu F, Wang L, Zhao J, Yang D, Kong L, et al. Effect of different photoinitiators

- on the properties of UV-cured electromagnetic shielding composites 2015;35:209–22. <https://doi.org/10.1515/polyeng-2014-0192>.
- [219] Kotz F, Risch P, Helmer D, Rapp BE. Highly fluorinated methacrylates for optical 3D printing of microfluidic devices. *Micromachines* 2018;9. <https://doi.org/10.3390/mi9030115>.
- [220] Manotham S, Channasanon S, Nanthananon P, Tanodekaew S, Tesavibul P. Photosensitive binder jetting technique for the fabrication of alumina ceramic. *J Manuf Process* 2021;62:313–22. <https://doi.org/10.1016/j.jmapro.2020.12.011>.
- [221] Qin X-H, Ovsianikov A, Stampfl J, Liska R. Additive manufacturing of photosensitive hydrogels for tissue engineering applications. *BioNanoMaterials* 2014;15. <https://doi.org/10.1515/bnm-2014-0008>.
- [222] ADMATEC. Admaflex 130 n.d. <https://admateceurope.com/admaflex130> (accessed January 25, 2022).
- [223] Brown ME. *Introduction to Thermal Analysis*. vol. 1. Dordrecht: Kluwer Academic Publishers; 2004. <https://doi.org/10.1007/0-306-48404-8>.
- [224] Chen X, Sun J, Guo B, Wang Y, Yu S, Wang W, et al. Effect of the particle size on the performance of BaTiO₃ piezoelectric ceramics produced by additive manufacturing. *Ceram Int* 2022;48:1285–92. <https://doi.org/10.1016/j.ceramint.2021.09.213>.
- [225] Cao J, Idrees M, Tian G, Liu J, Xiong S, Yuan J, et al. Complex SiC-based structures with high specific strength fabricated by vat photopolymerization and one-step pyrolysis. *Addit Manuf* 2021;48:102430. <https://doi.org/10.1016/j.addma.2021.102430>.
- [226] Pan Z, Wang D, Guo X, Li Y, Zhang Z, Xu C. High strength and microwave-absorbing polymer-derived SiCN honeycomb ceramic prepared by 3D printing. *J Eur Ceram Soc* 2022;42:1322–31. <https://doi.org/10.1016/j.jeurceramsoc.2021.12.003>.
- [227] Rieger T, Schubert T, Schurr J, Kopp A, Schwenkel M, Sellmer D, et al. Vat Photopolymerization of Cemented Carbide Specimen. *Materials (Basel)* 2021;14:7631. <https://doi.org/10.3390/ma14247631>.
- [228] He L, Wang X, Fei F, Chen L, Song X. Selectively doped piezoelectric ceramics with tunable piezoelectricity via suspension-enclosing projection stereolithography. *Addit Manuf* 2021;48:102407. <https://doi.org/10.1016/j.addma.2021.102407>.
- [229] He C, Liu X, Ma C, Cao Y, Hou F, Yan L, et al. Digital light processing of Si-based composite ceramics and bulk silica ceramics from a high solid loading polysiloxane/SiO₂ slurry. *J Eur Ceram Soc* 2021;41:7189–98. <https://doi.org/10.1016/j.jeurceramsoc.2021.07.016>.

- [230] Li H, Liu Y, Liu Y, Zeng Q, Hu K, Lu Z, et al. Effect of debinding temperature under an argon atmosphere on the microstructure and properties of 3D-printed alumina ceramics. *Mater Charact* 2020;168:110548. <https://doi.org/10.1016/j.matchar.2020.110548>.
- [231] Li H, Liu Y, Liu Y, Hu K, Lu Z, Liang J. Investigating the relation between debinding atmosphere and mechanical properties of stereolithography-based three-dimensional printed Al₂O₃ ceramic. *Proc Inst Mech Eng Part B J Eng Manuf* 2020;234:1686–94. <https://doi.org/10.1177/0954405420937855>.
- [232] Zou W, Yang P, Lin L, Li Y, Wu S. Improving cure performance of Si₃N₄ suspension with a high refractive index resin for stereolithography-based additive manufacturing. *Ceram Int* 2022. <https://doi.org/10.1016/j.ceramint.2022.01.124>.
- [233] Camargo IL, Erbereli R, Lovo JFP, Fortulan CA. Manufatura aditiva de mullita em impressora 3D comercial de baixo custo (Additive manufacturing of mullite in a low-cost commercial 3D printer). 65° Congr. Bras. Cerâmica (65 CBC), Águas de Lindóia: 2022.
- [234] Ulrich KT, Eppinger SD. *Product Design and Development*. Sixth. McGraw-Hill Education; 2015.
- [235] Pahl G, Beitz W, Feldhusen J, Grote K-H. *Engineering Design*. third. New York: Springer-Verlag; 2007.
- [236] Navas H. *TRIZ: Design Problem Solving with Systematic Innovation*. Adv. Ind. Des. Eng. 1st ed., 2013. <https://doi.org/10.5772/55979>.
- [237] Al'tshuller GS. *The Innovation Algorithm: TRIZ, Systematic Innovation and Technical Creativity*. Technical Innovation Center, Inc.; 1999.
- [238] Komarneni S, Schneider H, Okada K. *Mullite Synthesis and Processing*. Mullite, vol. 1, Wiley-VCH Verlag GmbH & Co. KGaA; 2005. <https://doi.org/https://doi.org/10.1002/3527607358.ch4>.
- [239] Aksay A, Dabbs DM, Sarikaya M. Mullite for structural, Electronic, and Optical Applications. *J Am Ceram Soc* 1991;74:2343.
- [240] Emadi R, Ashrafi H, Zamani Foroushani R. Effect of temperature on the reaction sintering of mechanically activated ZrSiO₄–Al₂O₃ mixture. *Ceram Int* 2015;41:14400–5. <https://doi.org/10.1016/j.ceramint.2015.07.074>.
- [241] Carvalho RG, Oliveira FJ, Silva RF, Costa FM. Mechanical behaviour of zirconia-mullite directionally solidified eutectics. *Mater Des* 2014;61:211–6. <https://doi.org/10.1016/j.matdes.2014.04.050>.
- [242] Khorsand A, Majidian H, Farvizi M. Development of AMZ composites via mutual

- attraction of particles in wet processing. *Int J Appl Ceram Technol* 2020;17:1822–32. <https://doi.org/10.1111/ijac.13522>.
- [243] Mazzei AC, RODrigues JA. Alumina-mullite-zirconia composites obtained by reaction sintering. Part I: microstructure and mechanical behavior. *J Mater Sci* 2000;35:2807–14.
- [244] Hazra S, Bandyopadhyay PP. Tribological properties of plasma sprayed zircon-alumina powder mixture with and without laser re-melting. *Trans Inst Met Finish* 2020;98:144–53. <https://doi.org/10.1080/00202967.2020.1757309>.
- [245] Ebadzadeh T, Ghasemi E. Influence of starting materials on the reaction sintering of mullite-ZrO₂ composites. *Mater Sci Eng A* 2000;283:289–97. [https://doi.org/10.1016/S0921-5093\(99\)00631-0](https://doi.org/10.1016/S0921-5093(99)00631-0).
- [246] Wei WJ, Kao HC, Lo MH. Phase Transformation and Grain Coarsening Zirconia / Mullite Composites 1996;2219:239–47.
- [247] Yuan L, Liu Z, Hou X, Liu Z, Zhu Q, Wang S, et al. Fibrous ZrO₂-mullite porous ceramics fabricated by a hydratable alumina based aqueous gel-casting process. *Ceram Int* 2019;45:8824–31. <https://doi.org/10.1016/j.ceramint.2019.01.209>.
- [248] Di Rupo E, Anseau MR. Solid state reactions in the ZrO₂ · SiO₂ - αAl₂O₃ system. *J Mater Sci* 1980;15:114–8. <https://doi.org/10.1007/BF00552434>.
- [249] Wahsh MMS, Khattab RM, Awaad M. Thermo-mechanical properties of mullite/zirconia reinforced alumina ceramic composites. *Mater Des* 2012;41:31–6. <https://doi.org/10.1016/j.matdes.2012.04.040>.
- [250] Medvedovski E. Alumina-mullite ceramics for structural applications. *Ceram Int* 2006;32:369–75. <https://doi.org/10.1016/j.ceramint.2005.04.001>.
- [251] Jang HM, Cho SM, Kim KT. Alumina-mullite-zirconia composites: Part 1. Colloidal processing and phase-formation characteristics. *J Mater Sci* 1996;31:5083–92. <https://doi.org/10.1007/BF00355909>.
- [252] Tosoh. Zirconia Powders 2019. <https://www.tosoh.com/our-products/advanced-materials/zirconia-powders> (accessed August 30, 2019).
- [253] Tosoh. Tosoh Zirconia Powder - Technical Bulletin n.d.
- [254] Fiocchi AA. Ciência e tecnologia da manufatura de ultraprecisão de cerâmicas avançadas: Lapidorrretificação Ud de superfícies planas de zircônia tetragonal policristalina estabilizada com ítria. Universidade de São Paulo, 2014. <https://doi.org/10.11606/T.18.2014.tde-30032015-094410>.
- [255] Tajiri HA, Al-Qureshi HA. Manufacturing and characterization of porous ceramic capillary membranes for enzyme functionalization through click chemistry. *J Brazilian*

- Soc Mech Sci Eng 2020;42:170. <https://doi.org/10.1007/s40430-020-2254-1>.
- [256] Camargo IL de, Lovo JFP, Erbereli R, Fortulan CA. SISTEMA DE RECOBRIMENTO COM LÂMINAS DE AÇÃO SEQUENCIAL PARA MANUFATURA ADITIVA POR FOTOPOLIMERIZAÇÃO EM CUBA(BR1020210215445), 2021.
- [257] Bertolo MVL, Moraes R de CM, Pfeifer C, Salgado VE, Correr ARC, Schneider LFJ. Influence of photoinitiator system on physical-chemical properties of experimental self-adhesive composites. *Braz Dent J* 2017;28:35–9. <https://doi.org/10.1590/0103-6440201700841>.
- [258] Roach M, Keicher D, Maines E, Wall B, Wall C, Lavin J, et al. Mechanical challenges of 3D printing ceramics using digital light processing. *Proc. 29th Annu. Int. Solid Free. Fabr. Symp. - An Addit. Manuf. Conf.*, 2018.
- [259] Rahaman MN. *Ceramic Processing and Sintering*. 2nd ed. CRC Press; 2017. <https://doi.org/10.1201/9781315274126>.
- [260] Barsoum M, Barsoum M. *Fundamentals of Ceramics*. 1st ed. CRC Press; 2002. <https://doi.org/10.1201/b21299>.
- [261] Hasanuzzaman M, Rafferty A, Olabi AG, Prescott T. Approach for sintering nano-sized yttria-stabilised zirconia. *Int J Nanomanuf* 2007;1:524. <https://doi.org/10.1504/IJNM.2007.014572>.
- [262] Knieke C, Sommer M, Peukert W. Identifying the apparent and true grinding limit. *Powder Technol* 2009;195:25–30. <https://doi.org/10.1016/j.powtec.2009.05.007>.
- [263] Huang Y-M, Jiang C-P. On-line force monitoring of platform ascending rapid prototyping system. *J Mater Process Technol* 2005;159:257–64. <https://doi.org/10.1016/j.jmatprotec.2004.05.015>.
- [264] Wu X, Lian Q, Li D, Jin Z. Biphasic osteochondral scaffold fabrication using multi-material mask projection stereolithography. *Rapid Prototyp J* 2019;25:277–88. <https://doi.org/10.1108/RPJ-07-2017-0144>.
- [265] Coppola B, Schmitt J, Lacondemine T, Tardivat C, Montanaro L, Palmero P. Digital light processing stereolithography of zirconia ceramics: Slurry elaboration and orientation-reliant mechanical properties. *J Eur Ceram Soc* 2022;42:2974–82. <https://doi.org/10.1016/j.jeurceramsoc.2022.01.024>.
- [266] Xiang D, Xu Y, Bai W, Lin H. Dental zirconia fabricated by stereolithography: Accuracy, translucency and mechanical properties in different build orientations. *Ceram Int* 2021;47:28837–47. <https://doi.org/10.1016/j.ceramint.2021.07.044>.
- [267] Li H, Hu K, Liu Y, Lu Z, Liang J. Improved mechanical properties of silica ceramic

- cores prepared by 3D printing and sintering processes. *Scr Mater* 2021;194:113665. <https://doi.org/10.1016/j.scriptamat.2020.113665>.
- [268] Shen M, Zhao W, Xing B, Sing Y, Gao S, Wang C, et al. Effects of exposure time and printing angle on the curing characteristics and flexural strength of ceramic samples fabricated via digital light processing. *Ceram Int* 2020;46:24379–84. <https://doi.org/10.1016/j.ceramint.2020.06.220>.
- [269] Zhu K, Yang D, Yu Z, Ma Y, Zhang S, Liu R, et al. Additive manufacturing of SiO₂ – Al₂O₃ refractory products via Direct Ink Writing. *Ceram Int* 2020;46:27254–61. <https://doi.org/10.1016/j.ceramint.2020.07.210>.
- [270] Li H, Liu Y, Liu Y, Zeng Q, Liang J. Silica strengthened alumina ceramic cores prepared by 3D printing. *J Eur Ceram Soc* 2021;41:2938–47. <https://doi.org/10.1016/j.jeurceramsoc.2020.11.050>.
- [271] Fernandes L, Salomão R. Preparation and Characterization of Mullite-Alumina Structures Formed " In Situ " from Calcined Alumina and Different Grades of Synthetic Amorphous Silica. *Mater Res* 2018;21:39–44.
- [272] Pereira D, Biasibetti GRS, Camerini R V., Pereira AS. Sintering of Mullite by Different Methods. *Mater Manuf Process* 2014;29:391–6. <https://doi.org/10.1080/10426914.2013.864400>.
- [273] Salomão R, Fernandes L, Spera NCM. Combined effects of SiO₂ ratio and purity on physical properties and microstructure of in situ alumina - mullite ceramics . *Int J Appl Ceram Technol* 2021;1–8. <https://doi.org/10.1111/ijac.13733>.
- [274] Sacks MD, Pask JA. Sintering of Mullite-Containing Materials: I , Effect of Composition 1982;66:65–70.
- [275] Rahaman MN. *Ceramic processing and sintering*. 2nd ed. CRC Press; 2003.
- [276] Rodrigo PDD, Boch P. High purity mullite ceramics by reaction sintering. *Int J High Technol Ceram* 1985;1:3–30. [https://doi.org/10.1016/0267-3762\(85\)90022-0](https://doi.org/10.1016/0267-3762(85)90022-0).
- [277] Sacks MD, Pask JA. Sintering of Mullite-Containing Materials: II, Effect of Agglomeration. *J Am Ceram Soc* 1982;65:70–7.
- [278] Souto PM, Menezes RR, Kiminami RHGA. Effect of Y₂O₃ additive on conventional and microwave sintering of mullite. *Ceram Int* 2011;37:241–8. <https://doi.org/10.1016/j.ceramint.2010.08.043>.
- [279] Souto PM, Menezes RR, Kiminami RHGA. Sintering of commercial mulite powder: Effect of MgO dopant. *J Mater Process Technol* 2009;209:548–53. <https://doi.org/10.1016/j.jmatprotec.2008.02.029>.

- [280] Montanaro L, Tulliani JM, Perrot C, Negro A. Sintering of industrial mullites. *J Eur Ceram Soc* 1997;17:1715–23. [https://doi.org/10.1016/s0955-2219\(97\)00043-5](https://doi.org/10.1016/s0955-2219(97)00043-5).
- [281] Aydin H, Tokatas G. Mechanical properties of zirconia toughened mullite composites fabricated by slip casting. *J Ceram Process Res* 2019;20:250–8. <https://doi.org/10.36410/jcpr.2019.20.3.250>.
- [282] Lian W, Liu Z, Zhu R, Wang W, Liu Y, Wang S, et al. Effects of zirconium source and content on zirconia crystal form, microstructure and mechanical properties of ZTM ceramics. *Ceram Int* 2021;47:19914–22. <https://doi.org/10.1016/j.ceramint.2021.03.327>.
- [283] Zhang K, Meng Q, Zhang X, Qu Z, Jing S, He R. Roles of solid loading in stereolithography additive manufacturing of ZrO₂ ceramic. *Int J Refract Met Hard Mater* 2021;99:105604. <https://doi.org/10.1016/j.ijrmhm.2021.105604>.
- [284] Liu W, Li M, Nie J, Wang C, Li W, Xing Z. Synergy of solid loading and printability of ceramic paste for optimized properties of alumina via stereolithography-based 3D printing. *J Mater Res Technol* 2020;9:11476–83. <https://doi.org/10.1016/j.jmrt.2020.08.038>.
- [285] Aydın H. Effect of La₂O₃ addition on the thermal, microstructure and mechanical properties of mullite–zirconia composites. *Iran J Mater Sci Eng* 2019;16:10–9. <https://doi.org/10.22068/ijmse.16.4.10>.
- [286] Chandra D, Das G, Maitra S. Comparison of the Role of MgO and CaO Additives on the Microstructures of Reaction-Sintered Zirconia-Mullite Composite. *Int J Appl Ceram Technol* 2015;12:771–82. <https://doi.org/10.1111/ijac.12263>.
- [287] Bodhak S, Bose S, Bandyopadhyay A. Densification Study and Mechanical Properties of Microwave-Sintered Mullite and Mullite-Zirconia Composites. *J Am Ceram Soc* 2011;94:32–41. <https://doi.org/10.1111/j.1551-2916.2010.04062.x>.
- [288] Besisa DHA, Ewais EMM. Investigation of mechanical strength of the functionally graded zirconia-mullite/alumina ceramics tailored for high temperature applications. *Mater Res Express* 2019;6. <https://doi.org/10.1088/2053-1591/ab177e>.
- [289] Zanelli C, Dondi M, Raimondo M, Guarini G. Phase composition of alumina-mullite-zirconia refractory materials. *J Eur Ceram Soc* 2010;30:29–35. <https://doi.org/10.1016/j.jeurceramsoc.2009.07.016>.
- [290] ThermoFisher Scientific. Electrons in SEM n.d. <https://www.thermofisher.com/br/en/home/materials-science/learning-center/applications/sem-electrons.html> (accessed May 11, 2022).